

# Ariel II Engineering Data Analysis

## Phase II Report

8 September 1965

Contract No. NAS5-9104

FACILITY FORM 602	N66 24504	
	(ACCESSION NUMBER)	(THRU)
	123	1
	(PAGES)	(CODE)
	CR-74539	31
	(NASA CR OR TMX OR AD NUMBER)	(CATEGORY)

Prepared by

Westinghouse Electric Corporation

Aerospace Division

Baltimore, Maryland

GPO PRICE \$ \_\_\_\_\_

CFSTI PRICE \$ \_\_\_\_\_

HQ \$ 4.00

MAIL \$ 1.75

for

Goddard Space Flight Center

Greenbelt, Maryland

Ariel II Engineering Data Analysis

Phase II Report

8 September 1965

Contract No. NAS5-9104

Prepared by

Westinghouse Electric Corporation

Aerospace Division

Baltimore, Maryland

for

Goddard Space Flight Center

Greenbelt, Maryland

## ABSTRACT

This report presents the methods and results of Phase II of a three-phase post-launch evaluation of Ariel II satellite engineering performance. Phase II is devoted to a review and summary of performance based upon data reduced in Phase I. Emphasis is placed upon anomalies and singular points in the performance record. In certain cases where direct data is lacking, inferences are drawn by correlating data of incidental applicability.

Three major areas of performance are discussed, namely, dynamical performance, power system performance and thermal behavior. Comparisons are drawn, where possible, between prelaunch predictions as derived from calculation and actual performance as represented by the data.

Areas of particular interest for consideration in Phase III are noted and an indication of the depth of these considerations is given.

## TABLE OF CONTENTS

<u>Title</u>	<u>Page No.</u>
Abstract	ii
1.0 INTRODUCTION	1
2.0 DYNAMICAL PERFORMANCE	2
2.1 Predicted Spacecraft Performance	2
2.2 Actual Spacecraft Performance	3
2.2.1 Spin Rate	3
2.2.2 Spin Acceleration	5
2.2.3 Solar Aspect Angle	7
2.2.3.1 Solar Aspect Angle Determination by Means of Ozone Spectrometer Data	10
2.2.3.2 Aspect Angle Information from the Broadband Ozone Detector	21
2.2.3.3 Aspect Angle Information from the Micrometeorite Detectors	22
2.2.3.4 Aspect Angle Information from the Spacecraft Temperatures	23
2.2.3.5 Aspect Angle Information from the Solar Current	24
2.2.4 Solar Position	24
2.2.5 Perigee Position	24
2.2.6 Perigee Velocity Vector	27
2.2.7 Right Ascension of Ascending Node	31
2.2.8 Angle Between Initial Spin Axis and Perigee Velocity Vector	31
2.2.9 Initial Spacecraft Orientation	34
2.3 Dynamical Conclusions and Recommendations	36
3.0 POWER SYSTEM PERFORMANCE	38
3.1 Regulated Voltage	39
3.1.1 Fault Determination	39
3.1.2 Anomalous Occurrence	39
3.1.3 Regulation Requirements	51
3.2 Battery Performance	51
3.2.1 Undervoltage Determination	52
3.2.2 Maximum Discharge Level	52

TABLE OF CONTENTS (Continued)

<u>Title</u>	<u>Page No.</u>
3.2.3 Charging Current Regulation	54
3.2.4 Degradation Determination	63
3.2.5 Battery Temperature	63
3.3 Solar Array Performance	63
3.3.1 Minimum Power Requirement	63
3.3.2 Maximum Power Output	64
4.0 THERMAL PERFORMANCE	72
4.1 Predicted Thermal Performance	72
4.2 Actual Thermal Performance	73
4.3 Conclusions and Recommendations	73
5.0 GENERAL CONCLUSIONS AND RECOMMENDATIONS	87

# LIST OF ILLUSTRATIONS

FIGURE NO.	ILLUSTRATION	PAGE NO.
------------	--------------	----------

1	Variation of Spin Rate with Time. . . . .	4
2	Variation of Spin Acceleration with Time. . . . .	6
3	Variation of Solar Aspect Angle with Time . . . . .	8
4	Expected Pulse Shapes from Ozone Spectrometer . . . . .	11
5	Fields of View for Ozone Spectrometer in Equatorial Plane. . . . .	12
6	Angular Relations of Spectrometer Pulses. . . . .	13
7	Difference in Spin Angle at 2795A between P2 and P3 . . . . .	14
8	Angular Description of Ozone Spectrometer Responses . .	16
9	Ozone Spectrometer Response . . . . .	19
10	Solar Position	25
11	Ariel II Perigee Position	28
12	Coordinates of Perigee Velocity Vector	30
13	Argument of Perigee and Right Ascension of Ascending Node. . . . .	32
14	Angle Between Initial Spin Axis and Perigee Velocity Vector . . . . .	33
15	PP #08, 200-day Graph . . . . .	40
16	PP #04, 200-day Graph . . . . .	41
17	PP #08, Orbit 415 . . . . .	42
18	PP #07, Orbit 415 . . . . .	43
19	PP #06, Orbit 415 . . . . .	44
20	PP #09, Orbit 415 . . . . .	45
21	PP #04, Orbit 415 . . . . .	46
22	PP #05, Orbit 415 . . . . .	47
23	PP #10, Orbit 415 . . . . .	48
24	PP #11, Orbit 415 . . . . .	49
25	PP #12, Orbit 415 . . . . .	50
26	PP #07, 200-day Graph . . . . .	53
27	PP #10, 200-day Graph . . . . .	55
28	PP #11, 200-day Graph . . . . .	56
29	PP #10, Orbit 2109. . . . .	57
30	PP #07, Orbit 2109. . . . .	58

LIST OF ILLUSTRATIONS (Continued)

FIGURE NO.	ILLUSTRATION	PAGE NO.
31	PP #11, Orbit 2109. . . . .	59
32	PP #10, Orbit 815 . . . . .	60
33	PP #07, Orbit 815 . . . . .	61
34	PP #11, Orbit 815 . . . . .	62
35	Available Power Profile, Orbit 704. . . . .	65
36	PP #09, Orbit 704 . . . . .	66
37	PP #07, Orbit 704 . . . . .	67
38	PP #06, Orbit 704 . . . . .	68
39	PP #10, Orbit 704 . . . . .	69
40	PP #12, Orbit 704 . . . . .	70
41	Actual and Predicted Performance for PP00 . . . . .	75
42	Actual and Predicted Performance for PP01 . . . . .	76
43	Actual and Predicted Performance for PP02 . . . . .	77
44	Actual and Predicted Performance for PP05 . . . . .	78
45	Actual and Predicted Performance for PP11 . . . . .	79
46	Actual and Predicted Performance for PP13 . . . . .	80
47	Actual and Predicted Performance for PP14 . . . . .	81
48	Actual and Revised Predicted Performance for PP02 . . . . .	82
49	Actual and Revised Predicted Performance for PP05 . . . . .	83
50	Actual and Revised Predicted Performance for PP11 . . . . .	84
51	Actual and Revised Predicted Performance for PP13 . . . . .	85
52	Actual and Revised Predicted Performance for PP14 . . . . .	86

## 1.0 INTRODUCTION

Phase II of contract NAS 5-9104 has been aimed at a definition of spacecraft performance based on data reduced in Phase I. Comparisons to pre-launch predictions have been drawn where possible. This report discusses the processes involved in pursuing these objectives and displays results in graphical form.

To present the most useful report, an outline derived from the contract objectives has been used. These objectives are actually four in number and consist of discussing and explaining the following points.

### 1. Primary Objectives

- (a) The unexpectedly rapid decrease in satellite spin rate
- (b) The satellite spin axis/sunline angle variation
- (c) The power system performance analysis

### 2. Secondary Objectives

- (a) Satellite thermal behavior.

Primary objectives (a) and (b) are treated as one because of their close interrelationship and the resulting area has been termed "dynamical performance". Another secondary objective allowed for the inclusion of the discussion of any other interesting phenomenon appearing in the data, but this has not developed.

Each objective has been discussed in entirety in one section of the report with predicted and actual performance and conclusions presented in that section. In this way the special interests of a reader whose vital concerns are with one area are served.

Generalized conclusions and recommendations are also presented in a section given that name. These conclusions state, in summary, that the Aerial II was successful as a spacecraft with some departures from



predicted or anticipated performance. This contract was not concerned with the success of the satellite as a collector of scientific information so no comment is given on that subject except to note that it is regarded as successful.

## 2.0 DYNAMICAL PERFORMANCE

In this area more than the others actual spacecraft performance must be inferred from data which was taken for another purpose, namely, the collection of scientific information. The methods and assumptions adopted in this inference are stated so that the reader may evaluate their validity and that of the conclusions. Conclusions relative to the spin velocity can be reached much more easily and with more confidence than those relating to spacecraft orientation. For this reason most of this section is devoted to facets of the latter problem.

### 2.1 Predicted Spacecraft Performance

It had been presumed prior to launch that the angular momentum vector,  $\vec{H}$ , of Ariel II would be established at orbital injection and would remain substantially invariant thereafter. Thus, it had been presumed that the spacecraft spin axis would be initially aligned with the velocity vector at injection. The British team assumed that this spin axis orientation would remain inertially fixed. GSFC made no pre-launch predictions regarding spin axis wander.

It had also been assumed by the British team that when all yo-yo weights, booms, paddles, and antennas had been deployed that the established vehicle spin rate would not vary significantly over a one-year period. The personnel at GSFC also concluded that there would be no significant despin of the spacecraft.

## 2.2 Actual Spacecraft Performance

### 2.2.1 Spin Rate

The satellite spin rate was determined primarily from the ozone spectrometer data. A distinguishing feature such as a sharp peak or valley on one of the spectrometer pulses was compared with the identical feature eight pulses later, corresponding to 360 deg of rotation about the spin axis. The measured time interval over one spin revolution when compared with the known telemetry data rate enables the spin rate to be calculated. Both DROD and IROD data were also employed to measure spin rate since each experiment developed pulses as a consequence of the scanning action of the satellite spin. The pulses were sharp enough to provide good angular resolution over one spin revolution. The satellite spin rate is plotted as a function of days from launch in figure 1. It may be seen that the satellite has an initial spin rate of 5.6 rpm which rapidly decreases to 2.2 rpm then increases to 3 rpm. After two more spin reversal cycles the satellite stops spinning entirely about 190 days after launch.

Prior to launch it was predicted that the satellite spin rate would be approximately 5 rpm after all yo-yo weights, booms, antennas, and solar paddles had been deployed. It was further presumed that the spin rate would not vary significantly over the nominal one-year lifetime of the satellite. The spinning action of the satellite is required for a number of reasons:

1. The experiments rely on vehicle spin to perform their necessary scanning functions
2. The vehicle is spin-stabilized
3. The galactic noise antenna relies on centrifugal forces to establish and retain its form

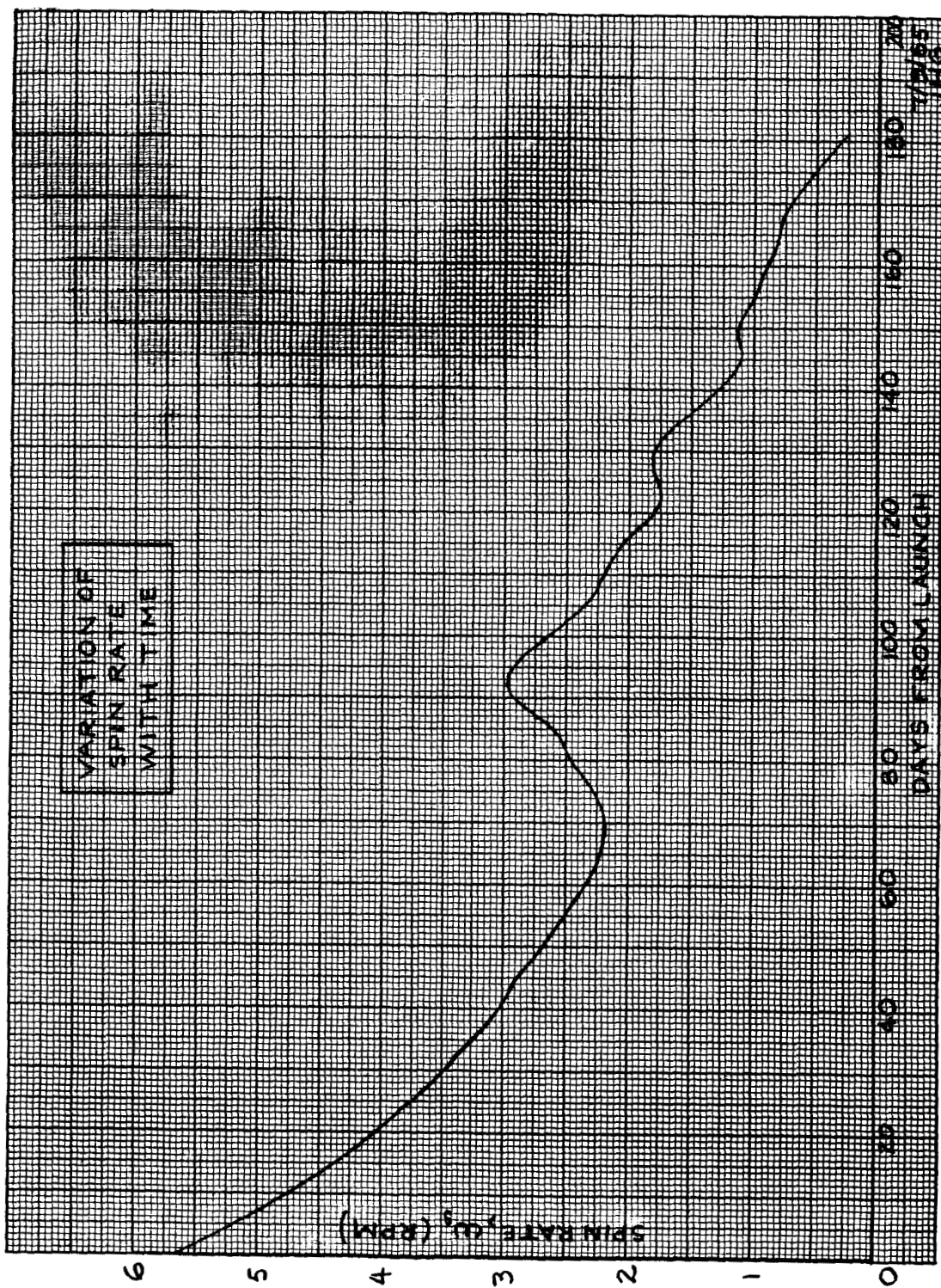


FIGURE 1 Variation of Spin Rate With Time

#### 4. Thermal balance of the center body

It is readily observed from figure 1 that the actual spin rate performance of Ariel II deviated markedly from the pre-launch presumption.

##### 2.2.2 Spin Acceleration

The spin acceleration time history of Ariel II was obtained by measuring the slope of the curve of figure 1, which is a time plot of spin rate. The acceleration about the spin or z-axis is plotted in figure 2 against days from launch. Several interesting observations may be noted by referring to figure 2:

1. The vehicle initially decelerates at a value of 0.10  
rpm/day
2. The vehicle actually has three periods of positive  
acceleration
3. The maximum value of spin acceleration is 0.05  
rpm/day

Prior to launch it was presumed that the spin acceleration would remain substantially zero. Referring to figure 2 it is seen that there is a definite departure between the presumed and the actual spin acceleration of the vehicle.

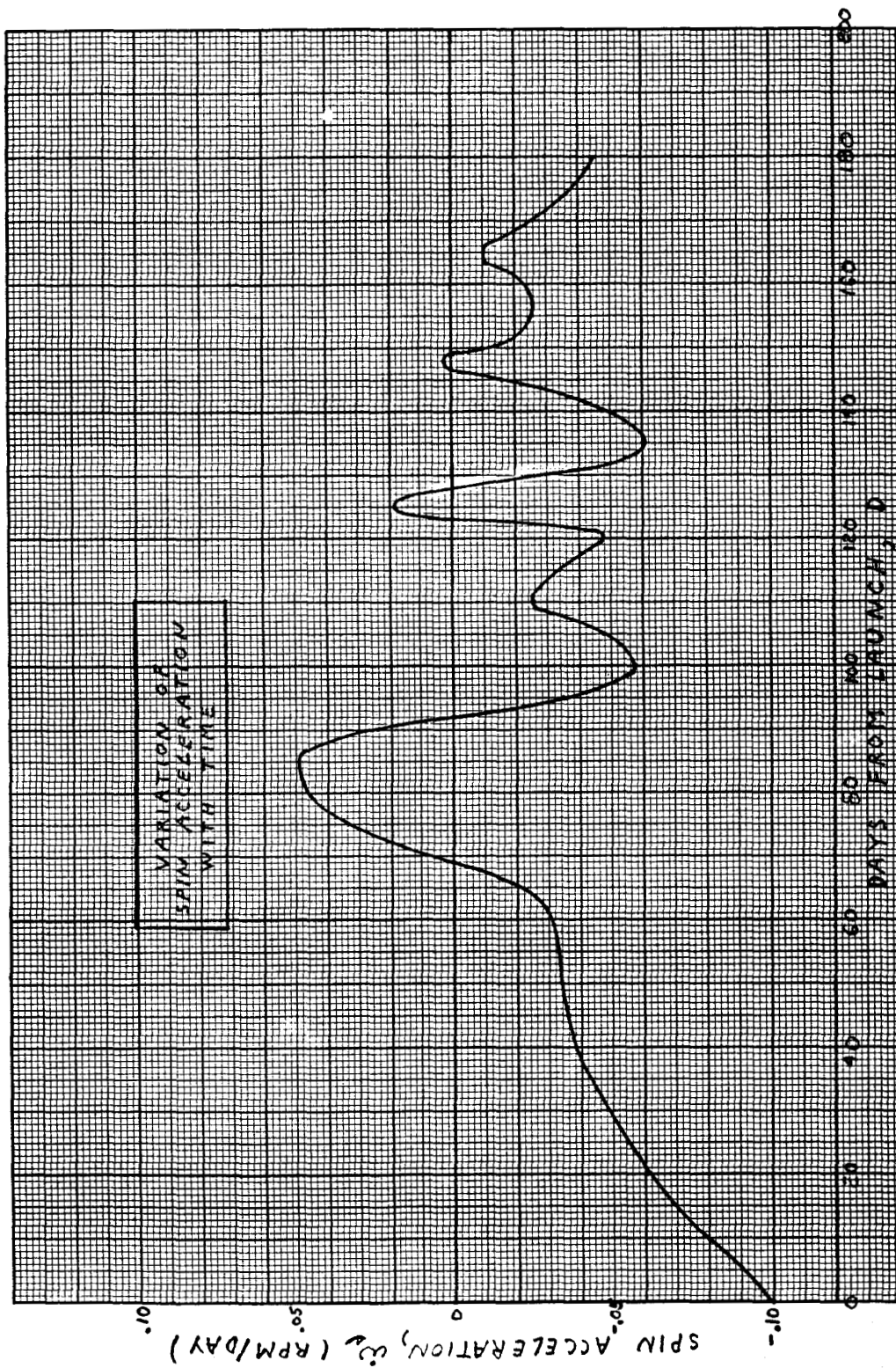


FIGURE 2 Variation of Spin Acceleration With Time

### 2.2.3 Solar Aspect Angle

The solar aspect angle,  $\delta_s$ , defined as that angle between the spin axis,  $\bar{z}$ , and the sunline,  $\bar{s}$ , is unfortunately not subject to direct measurement. This angle may only be derived by indirect means from such telemetered information as:

1. experiments
  - a. ozone spectrometer
  - b. broadband ozone detectors
  - c. DROD and IROD micrometeorite detectors
2. performance parameters
  - a. temperatures at several points
  - b. solar current

The ozone spectrometer furnished the principal evidence for the solar aspect angle since it is basically more sensitive to solar aspect than are the other sensors. This method is subsequently discussed as are others based on the various sources of information listed above.

The time plot of solar aspect angle is presented in figure 3. This angle is developed as a composite curve based on several weighted sources as previously indicated. It should be noted that this curve is not precise and may be in error by  $\pm 20$  deg. At times some of the data conflicts or disagrees by a considerable angle. The quality of the ozone spectrometer data deteriorates as time proceeds due to gradual mirror degradation. As a result the aspect angle becomes more uncertain as time progresses. The aspect angle past 165 days from launch is subject to question because of conflicting information.

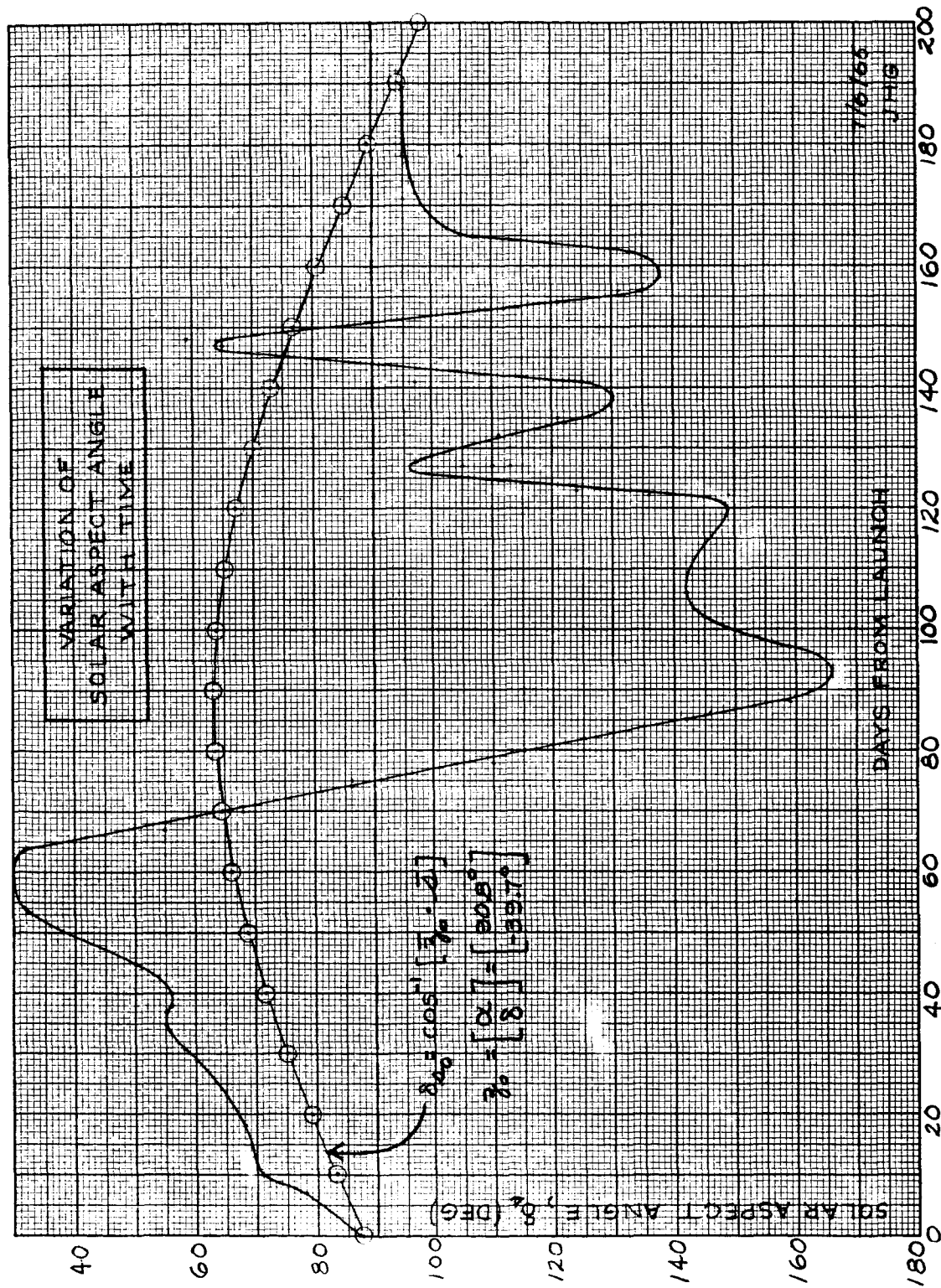


FIGURE 3 Variation of Solar Aspect Angle With Time



Also presented in figure 3 is the solar aspect angle that would have applied if the initial spin axis orientation had remained fixed in space. This curve is determined by calculating the angle between the initial spin vector,

$$\bar{j}_0 = \begin{bmatrix} \alpha_{j_0} \\ \delta_{j_0} \end{bmatrix} = \begin{bmatrix} 90.8^\circ \\ -39.7^\circ \end{bmatrix}$$

and the actual sunline vector,

$$\bar{s} = \begin{bmatrix} \alpha_s \\ \delta_s \end{bmatrix}$$

The angle between these two unit vectors is then:

$$\delta_{s_0} = \cos^{-1} [\bar{j}_0 \cdot \bar{s}]$$

or

$$\delta_{s_0} = \cos^{-1} [\sin \delta_{j_0} \sin \delta_s + \cos \delta_{j_0} \cos \delta_s \cos(\alpha_{j_0} - \alpha_s)]$$

It is apparent from a comparison of the two curves of figure 3 that the specific orientation is not fixed but rather is undergoing considerable and rapid changes.



#### 2.2.3.1 Solar Aspect Angle Determination by Means of Ozone Spectrometer Data

The two prism spectrometers, used to measure ozone distribution in the earth's atmosphere, look in opposite directions. Together they form eight separate spectra for each revolution about the spin axis of the satellite. A rather narrow pulse is produced each time the sun sweeps past one of the fields of view of either spectrometer. Each spectrum covers wavelengths in the near UV region down to 2500 Å. The recorded pulse shapes, representing the UV spectra, change as a consequence of ozone attenuation of the horizon-grazing sunlight as indicated by figure 4.

The geometrical distribution of the two spectrometers and corresponding eight fields of view is illustrated by figure 5 for the case where the sun is in the equatorial plane (90 deg. solar aspect angle). In this figure, the nominal angular limits, B and R, of each field of view are determined by wavelengths of 2650 and 4000 Å.

For purposes of illustration, let us assume that rectangular pulses are produced as a consequence of spin scanning. A plot of spectrometer response as a function of spin angle is presented in figure 6 which illustrates the relative angular relations of the eight pulses during one spin revolution.

As the solar aspect angle departs from the equatorial or 90 deg. position, the angular relation shifts among the various pulses, i.e., the B (blue) limit moves toward the R (red) limit which retreats in the same direction. These relative motions are indicated by the arrow directions of figure 6. The differential spin angle between pulses 2 and 3 at the specific wavelength of 2795 Å is presented as a function of sun latitude by the UK-developed curve of figure 7. It is this angle characteristic which is used to derive solar aspect angle information from the ozone spectrometer data. It should be noted that the curve does not distinguish between north and south latitudes since the spectrometers are symmetrical about the equator of the spacecraft.

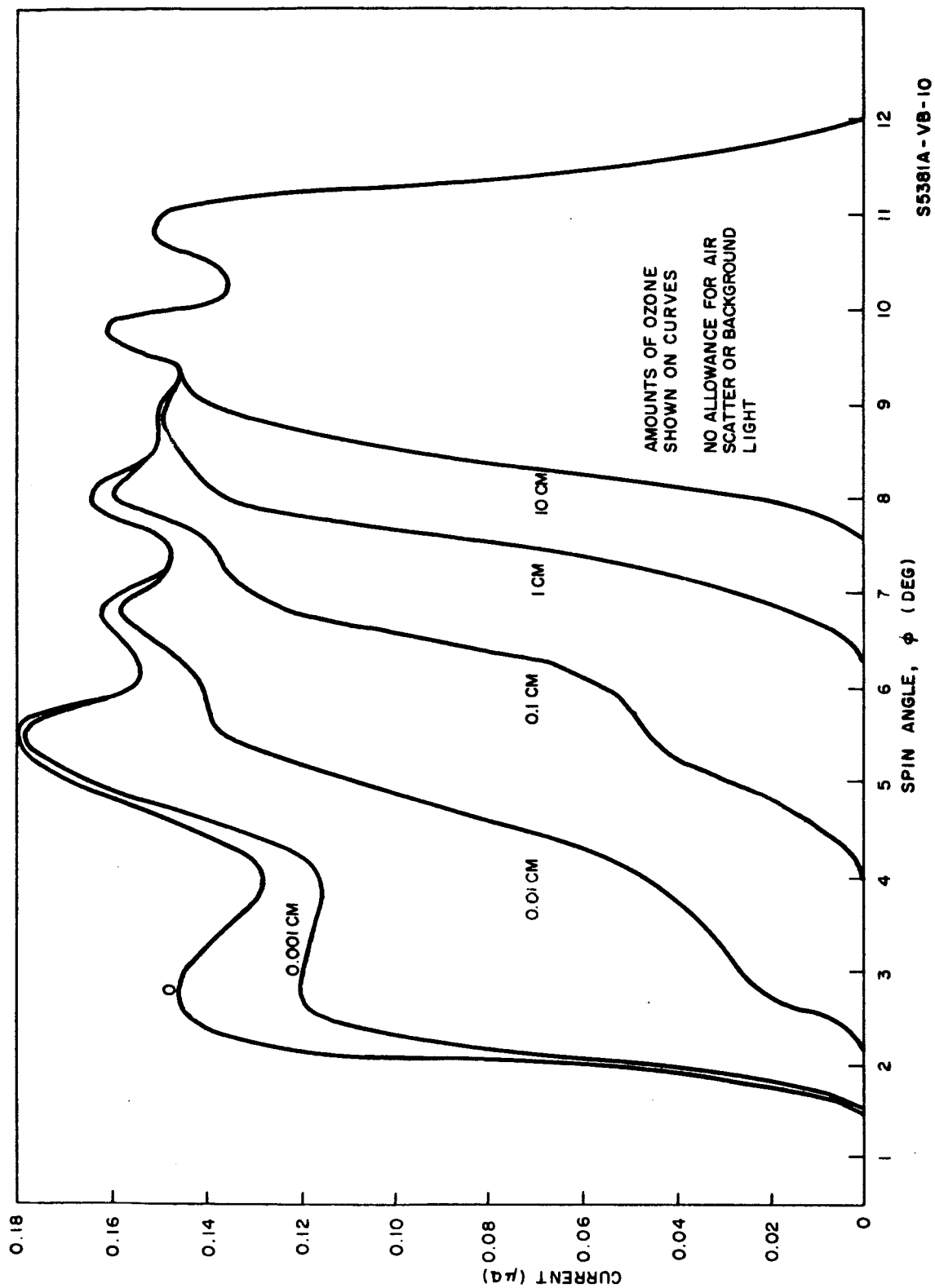
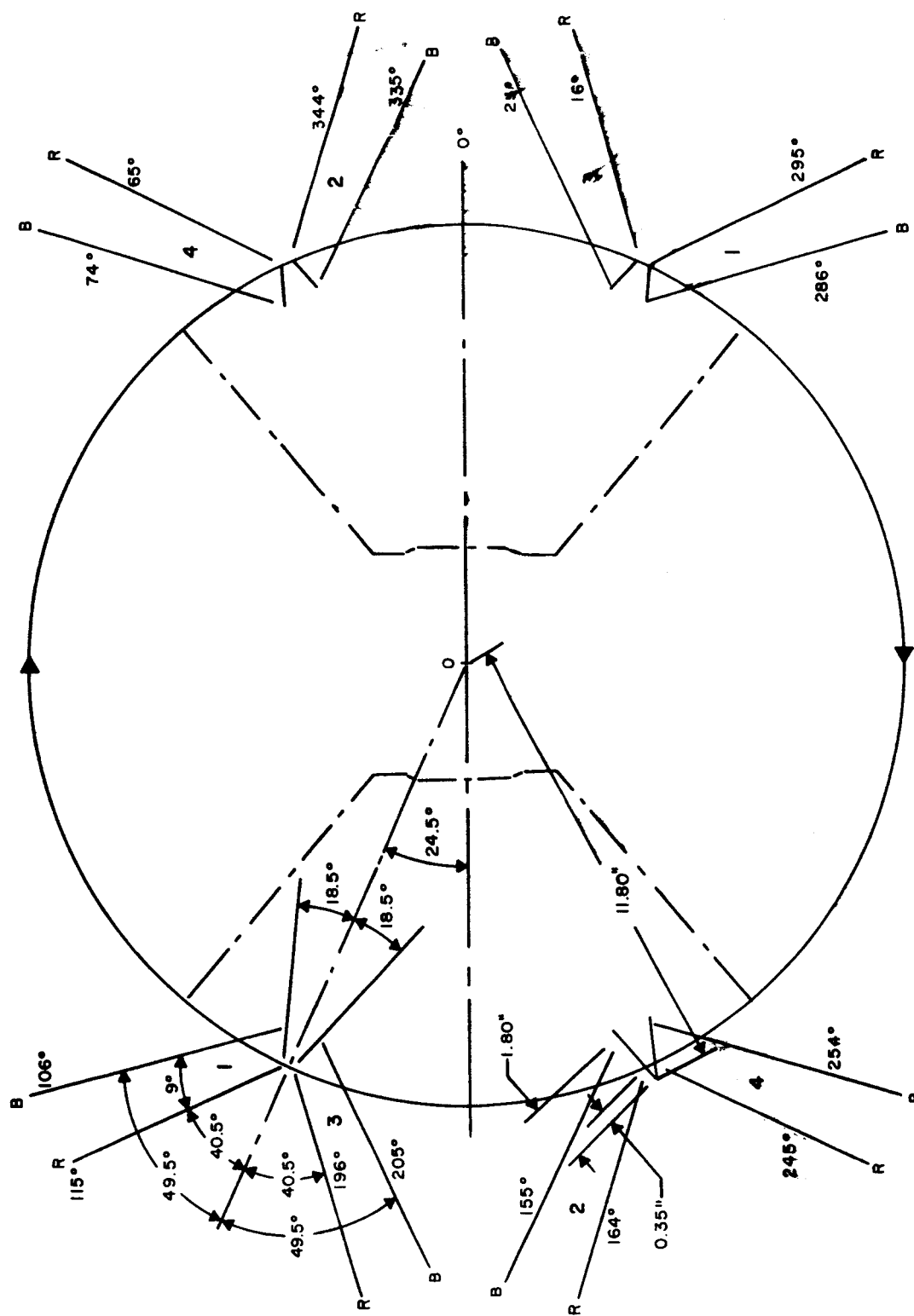


FIGURE 4 Expected Pulse Shape From Ozone Spectrometer



RAYS OF SHORTEST WAVELENGTH, 2650 Å MARKED B  
 RAYS OF LONGEST WAVELENGTH, 4000 Å MARKED R

S5381A-VC-3

FIGURE 5 Fields of View For Ozone Spectrometer In Equatorial Plane

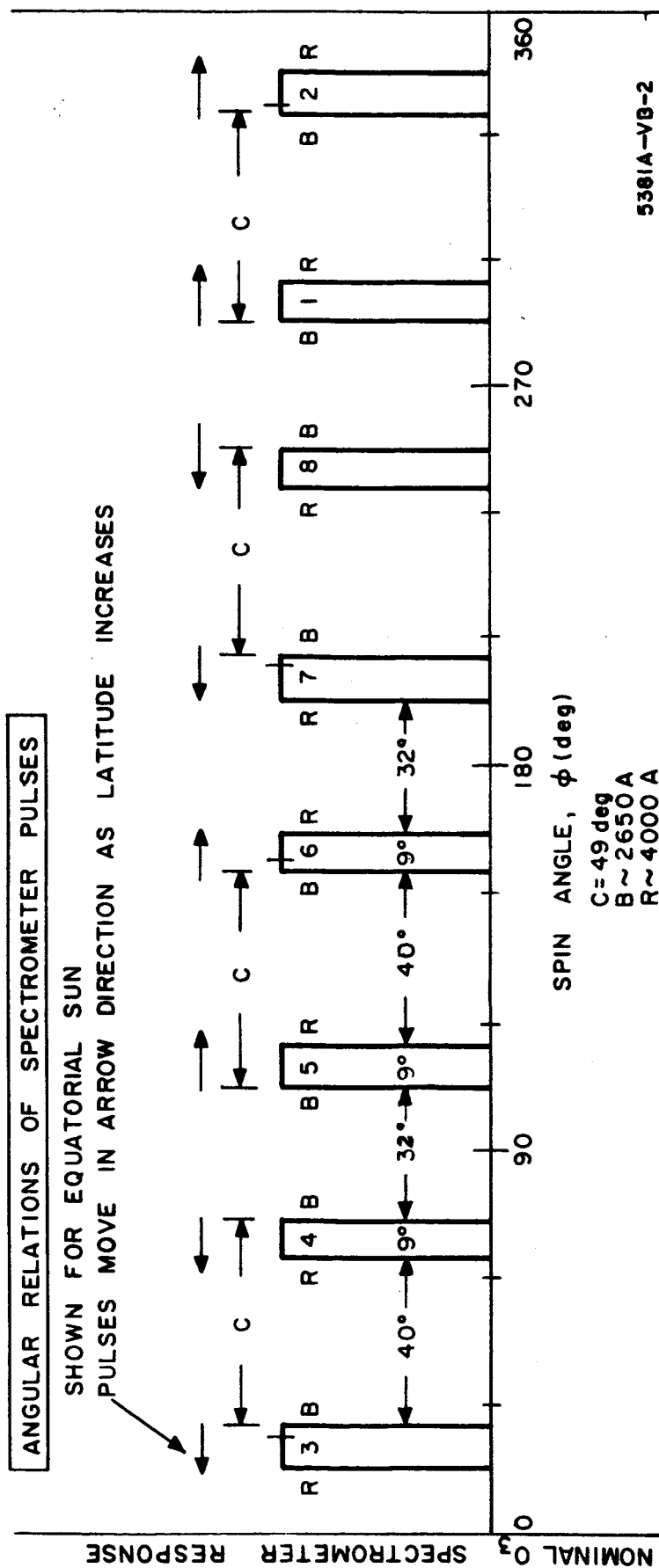


FIGURE 6 Angular Relations of Spectrometer Pulses

S-3 P2-P3

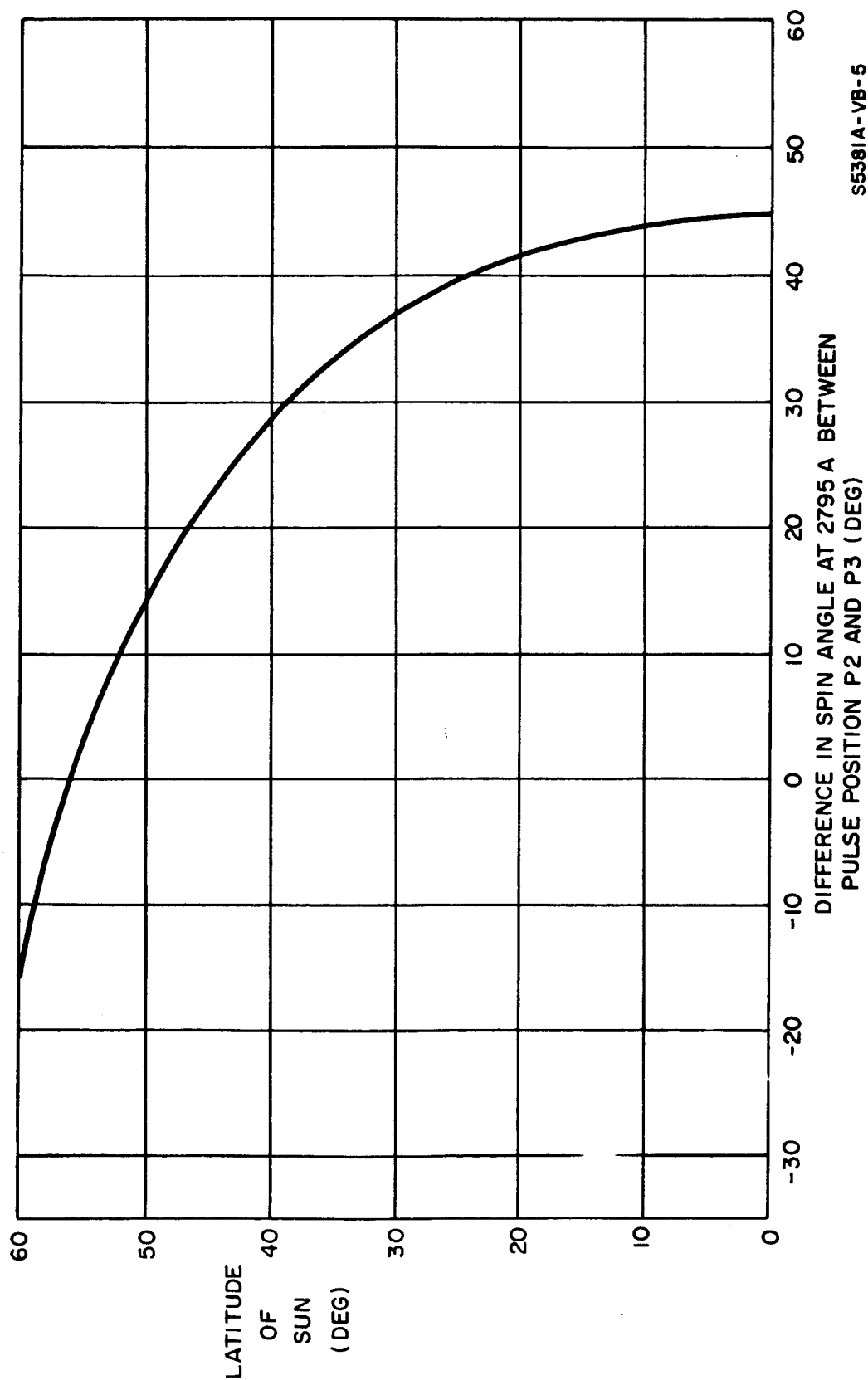


FIGURE 7 Difference In Spin Angle At 2795A Between Pulse Positions P2 And P3 (Degrees)

The method of deriving solar aspect angle from a time plot of ozone spectrometer response over one spin revolution is described below.

1. From the actual time plot the individual pulses are first identified by number by: (a) considering the relative angular relationships among the pulses, and (b) observing the waveforms of adjacent pulses to determine whether the blue, B, edge leads or trails.
2. As the solar latitude increases, pulse pairs 2 and 3 and 6 and 7 move closer together while pulse pairs 4 and 5 and 8 and (1 + 2  $\pi$ ) move apart. At the same time the angular separation between pulse pairs 1 and 2 and 5 and 6 remains constant.
3. The angular designations and relations of each pulse are shown in figure 8. What is desired is the angular difference,  $\Delta\phi$ , between pulses 2 and 3 (or 6 and 7) at the specific wavelength of 2795 Å. The difference angle,  $\Delta\phi$ , is obtained by the relation:

$$\Delta\phi = (\phi_3 - \phi_2) + K(\phi_2' - \phi_2) \quad (1)$$

The constant, K, is evaluated at the first day of the flight where it was calculated that the solar aspect angle was 86 deg. — corresponding to a latitude of 4 deg. From measurements of the corresponding plot of the  $O_3$  spectrometer it was determined that:

$$\phi_2' - \phi_2 = 10.12 \text{ div (12.35 deg)}$$

$$\phi_3 - \phi_2 = 33.12 \text{ div (40.42 deg)}$$

From the calibrating curve for a latitude of 4 deg:

$$\Delta\phi = 44.5 \text{ deg.}$$

SPIN ANGLE

$$\lambda = (\phi_{1+2}\pi - \phi_1)$$

a  $\Delta\phi = (\phi_3 - \phi_2) + K(\phi'_2 - \phi_2)$

WHERE  $K = 0.3304$

### FIGURE 8 Angular Description Of Ozone Spectrometer Responses

Solving for K from equation (1):

$$\begin{aligned} K &= \frac{\Delta\phi - (\phi_3 - \phi_2)}{(\phi'_2 - \phi_2)} \\ &= \frac{44.5 - 40.42}{12.35} \\ &= \underline{0.3304} \end{aligned}$$

Equation (1) may then be stated:

$$\Delta\phi = (\phi_3 - \phi_2) + 0.3304 (\phi'_2 - \phi_2) \quad (1a)$$

At higher latitudes pulses 2 and 3 overlap making it impossible to measure  $\phi_2$  and  $\phi_3$  directly. This difficulty is overcome by making use of  $\phi_4$  and  $\phi_5$  since their corresponding pulses separate as the latitude increases. Referring to figure 6:

$$(\phi_5 - \phi_1) = 180 \text{ deg.}$$

$$\text{or } (\phi_5 - \phi_4) + (\phi_4 - \phi_3) + (\phi_3 - \phi_2) + (\phi_2 - \phi_1) = 180 \text{ deg.}$$

$$\text{but } (\phi_4 - \phi_3) = (\phi_2 - \phi_1) = \text{const.} = 49 \text{ deg.}$$

$$\therefore (\phi_5 - \phi_4) + 49 + (\phi_3 - \phi_2) + 49 = 180$$

$$\text{or } (\phi_3 - \phi_2) = 82 \text{ deg.} - (\phi_5 - \phi_4) \quad (2)$$

The method of establishing incremental phase angle from proportional pulse width is subject to some error in determining just where the 2795 Å wavelength UV occurs in the spectrum or pulse waveform. Fortunately the pulse is relatively narrow, and also the measurements are deliberately removed from the horizon-grazing regions where the UV is attenuated by the ozone content of the atmosphere.



4. In determining the incremental phase angle,  $\Delta\phi$ , from each plot, several equivalent measurements were taken and the results averaged to minimize the effects of individual spectral deviations and reduce measurement errors. The averaged angular differences are:

$$a. (\phi_2' - \phi_2)_{eq} = \frac{1}{4} [(\phi_2' - \phi_2) + (\phi_3' - \phi_3) + (\phi_6' - \phi_6) + (\phi_7' - \phi_7)] \quad (3)$$

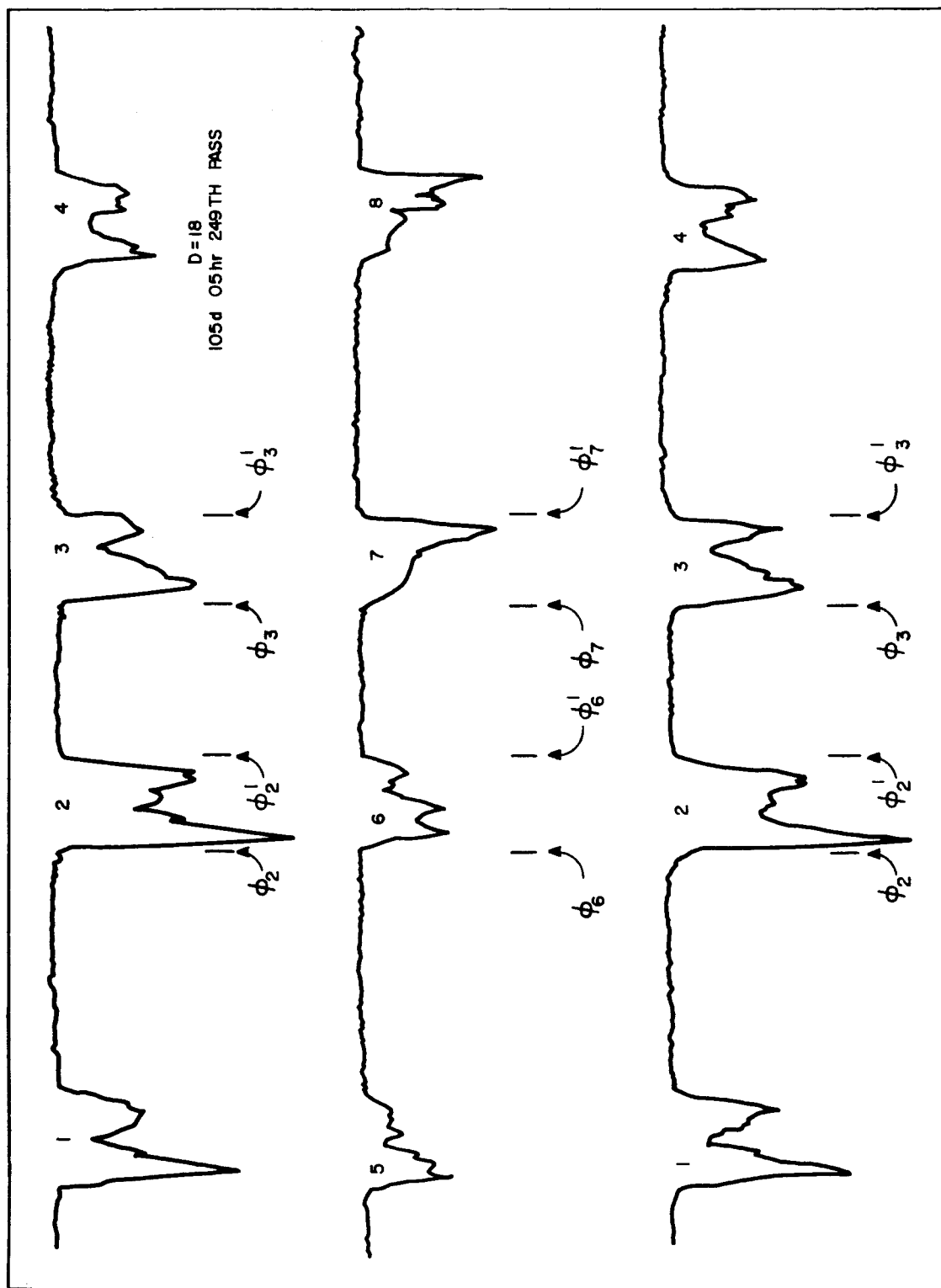
$$b. (\phi_3 - \phi_2)_{eq} = \frac{1}{4} [(\phi_3 - \phi_2) + (\phi_3' - \phi_2') + (\phi_7 - \phi_6) + (\phi_7' - \phi_6')] \quad (4)$$

$$c. (\phi_5 - \phi_4)_{eq} = \frac{1}{4} [(\phi_5 - \phi_4) + (\phi_5' - \phi_4') + (\phi_{1+2\pi} - \phi_3) + (\phi_{1+2\pi}' - \phi_3')] \quad (5)$$

As the flight progressed, the cylindrical diverging mirrors apparently became degraded, resulting in pulse irregularity with a marked attenuation of the received signal. A typical ozone spectrometer time response ( $D = 18$ ) is shown in figure 9, where the points of interest are also displayed. An illustrative calculation of  $\Delta\phi$  is given below for this particular response.

a. The wavelength,  $\lambda$ , is measured from a distinctive peak or valley in one spectrum and in the same spectrum exactly one spin revolution later.

$$\lambda = 398.5 \text{ div} \sim 360 \text{ deg.}$$



55381A-VB-4

FIGURE 9 Spectrometer Response

- b. The spin rate is determined by the constant data rate and the wavelength:

$$W_s = 4.584 \frac{\text{rpm}}{\text{deg/div}} \times \frac{360 \text{ deg.}}{398.5 \text{ div.}}$$

$$= \underline{4.151} \text{ rpm}$$

- c. Using equation (3)

$$(\phi'_2 - \phi_2) = 1/4 (15 + 14 + 15 + 15)$$

$$= 14.75 \text{ div.} = 13.33 \text{ deg.}$$

- d. From equation (4):

$$(\phi_3 - \phi_2) = 1/4 (40 + 39 + 39 + 39)$$

$$= 39.2 \text{ div} = 35.41 \text{ deg.}$$

- e. The incremental phase angle is then obtained from equation (1a):

$$\Delta\phi = 35.41 + 0.3304 \times 13.33$$

$$= 40.81 \text{ deg.}$$

- f. From the curve of figure 7 using the above value of  $\Delta\phi$ :
- latitude = 22 deg.

- g. The solar aspect angle is then:

$$\delta = c (22^\circ)$$

$$= \underline{68} \text{ deg.}$$

### 2.2.3.2 Aspect Angle Information from the Broadband Ozone Detector

The broadband ozone detectors include: an ozone photocell with filters to measure radiation in the band from 2500 to 3500 A; and a monitor photocell to measure the radiation between 3600 and 4000 A. These photocells rely on the sun for their light source, and scanning is provided by the spin of the spacecraft. The photocells have an omnidirectional field of view of  $\pm 45$  deg off the equator. Measurements are of value only at sunrise and sunset.

Theoretically each telemetry antenna, whose tip coordinates are sta. 4.62 in. and radius of 22.65 in., may cast a shadow on the photocells when the angle off the nose exceeds:

Cell	Sta. (in.)	Angle (deg)
ozone	9.06	78
monitor	12.50	71

Each inertia boom, with tip coordinates of sta. 39.4 in. and radius of 47.5 in. and each galatic boom, with tip coordinates of sta. 38.9 in. and a radius of 46.5 in., may cast a shadow on the photocells when the angle off the nose exceeds:

Cell	Angle (deg)
ozone	123
monitor	120

### 2.2.3.3 Aspect Angle Information from the Micrometeorite Detectors

There are two pairs of micrometeorite detectors mounted on the satellite. The Instantaneous Read-out Detectors (IROD), which look in opposite directions, utilize aluminum foil exposed along the circumferential surface. A strip solar cell with a cylindrical lens forms the detector while the sun acts as the light source. Two calibration holes provide calibration pulses each spin revolution. Based on calibration hole sizes and tempering with other aspect data the IROD pulses appear when the solar aspect angle exceeds 50 to 60 deg and disappear when the angle exceeds 117 to 136 deg.

The Delayed Read-Out Detectors (DROD), which look in opposite directions, utilize metalized Mylar exposed in the longitudinal direction. A strip solar cell mounted directly below the Mylar is the sensor while the sun is the light source. Rectangular tapered slots terminating in pin holes provide calibration pulses before or after the normal readout. Based on comparison with other data it appears that the DROD starts responding between 33 and 55 deg off the nose and shuts off out as far as 148 deg.

The DROD, which has coordinates of sta. 27.12 and radius of 11.5 in., may have its calibrating slot shadowed by the galactic boom. The boom is rotated 32.8 deg. from the DROD and has tip coordinates of sta. 38.9 at a radius of 39.0 in. Thus the boom may cause shadowing of the DROD calibrating pulse if the angle off the nose exceeds 113 deg. This corresponds to a DROD look angle of 47 deg relative to the equator.

#### 2.2.3.4 Aspect Angle Information from the Spacecraft Temperatures

The temperatures at several points on the spacecraft were used to help establish solar aspect angle. Maximum and minimum conditions can be determined, spectrometer ambiguities may be resolved and points of equal aspect angle can be established. Of the eight performance parameter temperatures, the ozone cell temperature is the most helpful since it is readily responsive to solar radiation and is reasonably well isolated from structure. The ozone cell thermistor is shadowed by a shoulder at an angle of 135 deg and is shadowed by the vehicle itself at 145 deg. It appears that this signal failed after 178 and before 185 days from launch.

The monitor cell temperature is another good indicator except that the signal bottoms out at  $-7^{\circ}\text{C}$ . This thermistor is shadowed by the vehicle at 135 deg.

The tape recorder temperature is of value since it responds when the sun is off the bottom or solar-paddle end of the spacecraft.

The temperature data must be used with care because of the effects of percent sunlight. In general, when the sunlight does not exceed 70 percent the temperature data may be used without appreciable error since the minimum sunlight is 63 percent. Because of periods of excessive sunlight, gaps occur in the useful temperature data over the following days from launch:

17 - 37  
86 - 108  
159 - 176  
195 - 200

for a total of 64 days. The first two periods unfortunately occur at critical periods of minimum and maximum solar aspect angle respectively.

#### 2.2.3.5 Aspect Angle Information from the Solar Current

Because of the angular orientation of the four solar paddles, a modulation is introduced into the solar current as a consequence of spacecraft spin. This spin modulation will disappear only when the sun is at an aspect angle of 0 or 180 deg. The former angle is never achieved, but the latter angle is approached between 88 and 97 days from launch, although it does not appear that a solar aspect angle of 180 deg is actually attained. This is not surprising since it would be purely a coincidence if a solar aspect angle of 180 deg were actually achieved.

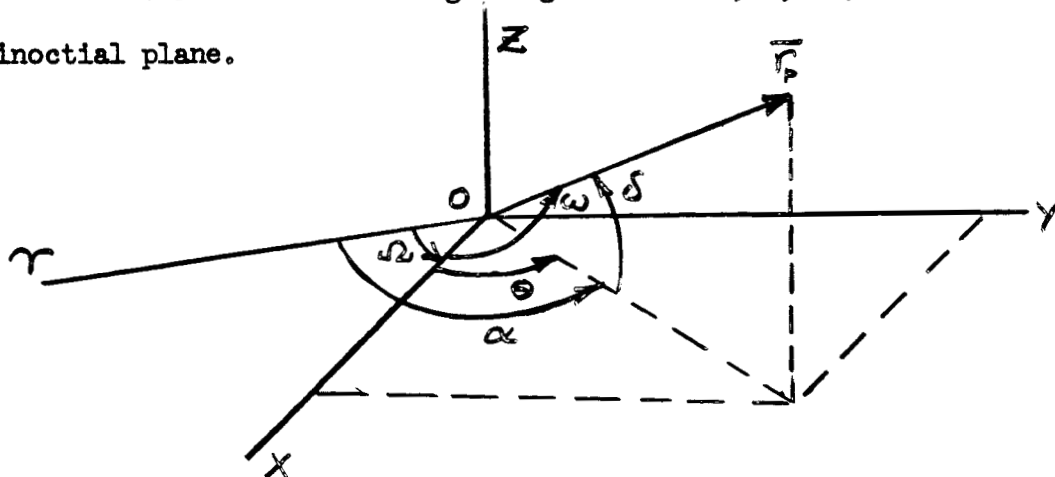
#### 2.2.4 Solar Position

The position of the sunline,  $\bar{s}$ , for 200 days from launch is plotted in celestial coordinates in the curves of figure 10. The solar position is obtained from The American Ephemeris and Nautical Almanac, 1964.

#### 2.2.5 Perigee Position

It is desired to determine the perigee position vector in celestial coordinates, i.e., right ascension and declination,  $\alpha$  and  $\delta$ .

Refer to the following diagram where X, Y, & Z lie in the equinoctial plane.



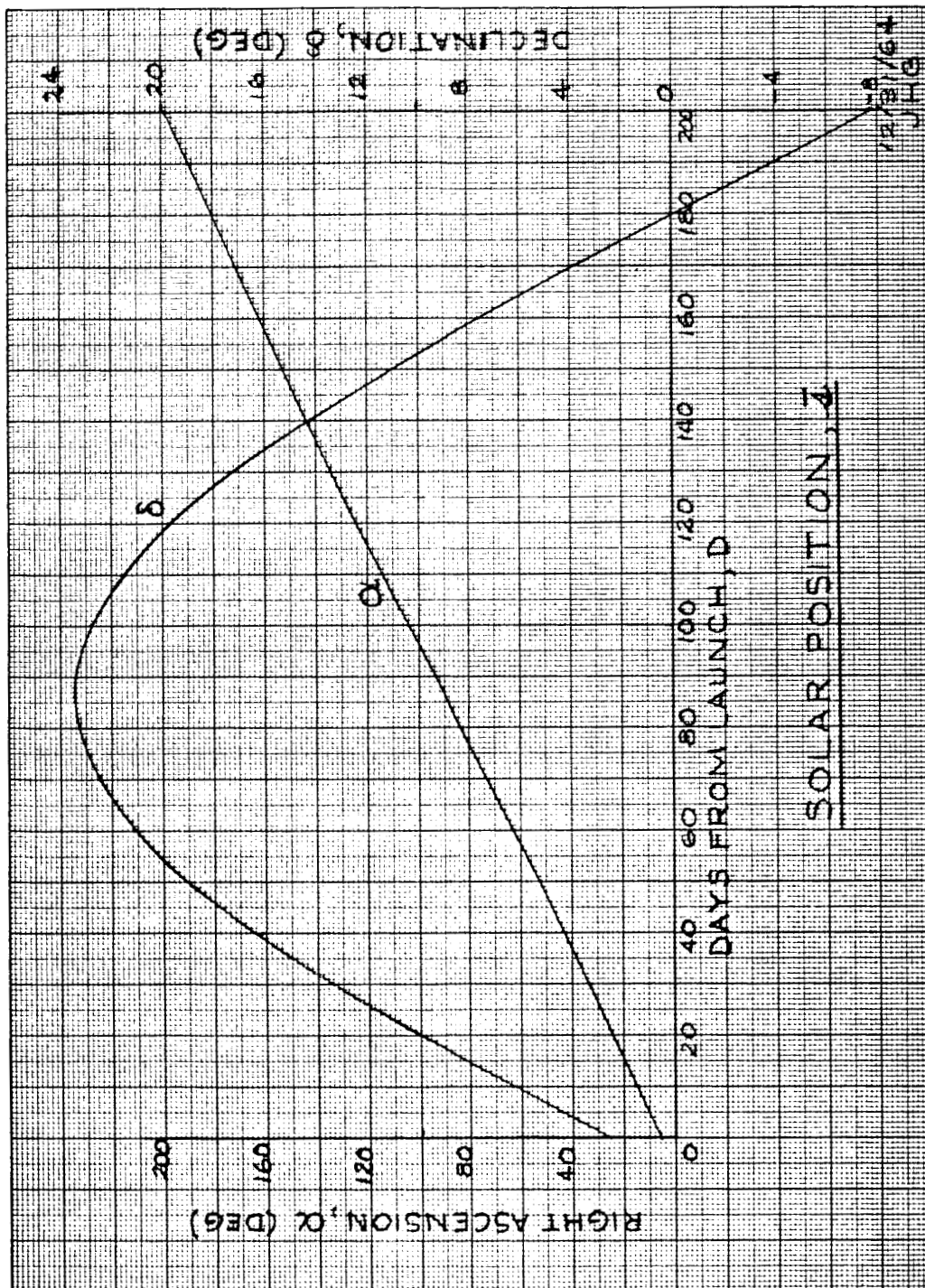


FIGURE 10 Solar Position,  $\delta$



The declination,  $\delta$ , of  $\vec{r}_p$  is the same angle as the latitude of perigee,  $\phi_p$ , as provided by the refined world map:

$$\delta = \phi_p \quad (1)$$

Using spherical trigonometry we obtain the relation:

$$\cos w = \cos \theta \cos \delta \quad (2)$$

Solving for  $\theta$  we have:

$$\theta = \cos^{-1} \left( \frac{\cos w}{\cos \delta} \right) \quad (3)$$

The right ascension of  $\vec{r}_p$  is then determined:

$$\alpha = \Omega + \theta \quad (4)$$

where  $\Omega$  = right ascension of the ascending node (provided by the refined world map).

Equation (4) is actually true only if we disregard orbital precession,  $\dot{\Omega}$ . The precession rate for this orbit is approximately -4.1 deg/day and does not introduce a significant error (always less than 0.29 deg). Using 3/27/64 elements as an example:

where:  $w = 138.7^\circ$

$$\Omega = 229.8^\circ$$

$$\delta = \underline{31.4^\circ}$$

$$\theta = \cos^{-1} \left( \frac{\cos w}{\cos \delta} \right)$$

$$= \cos^{-1} \left( \frac{\cos 138.7}{\cos 31.4^\circ} \right)$$

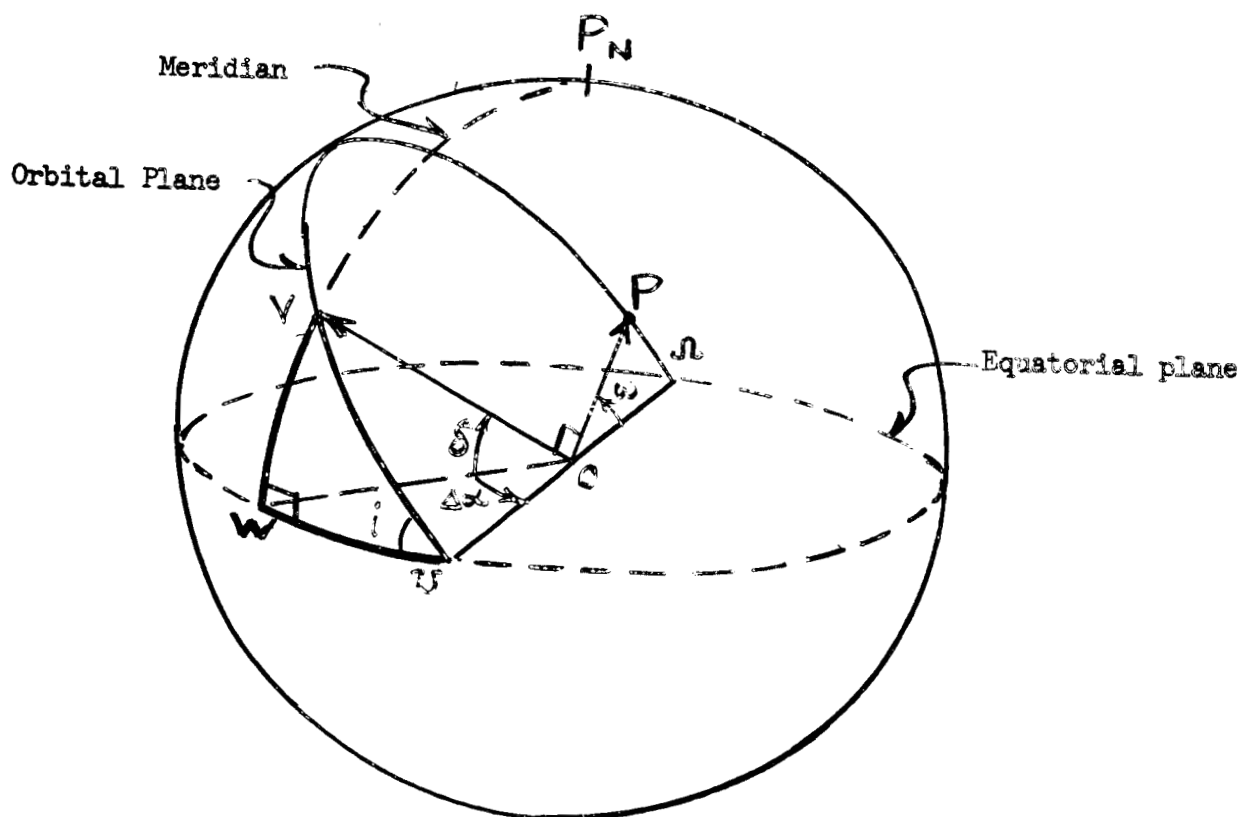
$$= \underline{151.7^\circ}$$

$$\begin{aligned}
 \alpha &= \Omega + \theta \\
 &= 229.8 + 151.7 \\
 &= \underline{21.5^\circ}
 \end{aligned}$$

The perigee position vector,  $\vec{r}_p$ , is plotted in celestial coordinates in figure 11.

#### 2.2.6 Perigee Velocity Vector

To establish the position vector of perigee velocity in celestial coordinates, consider the following diagram:



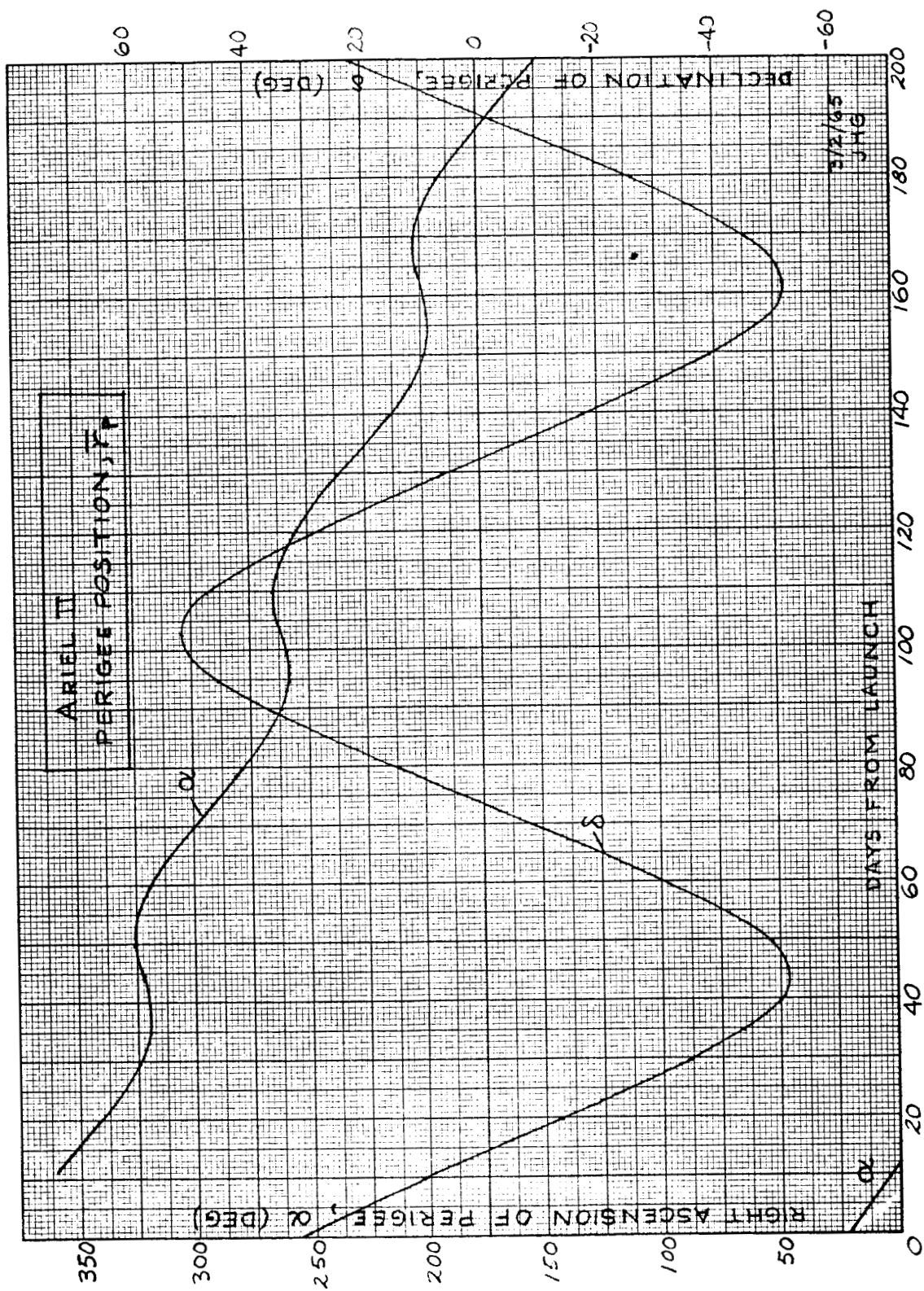
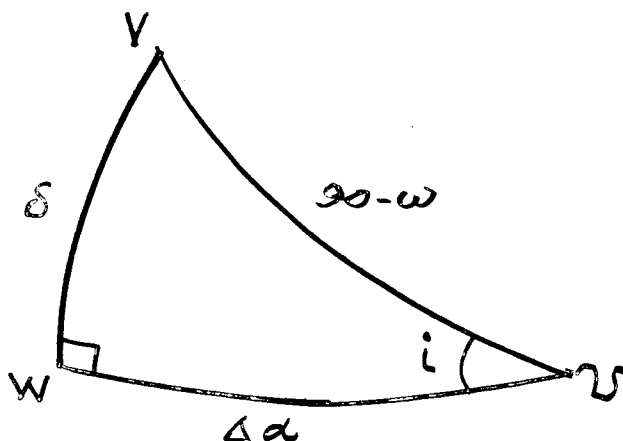


FIGURE 11 Ariel II Perigee Position

The velocity vector at perigee is in the plane of the orbit, and it always leads the perigee position by 90 deg. We can thus form the right spherical triangle V, W,  $\mathcal{V}$ .



The right ascension of the ascending node,  $\mathcal{Q}$ , the argument of the perigee,  $\omega$ , and the inclination,  $i$ , are known from the orbital elements listed in the Refined World Map.

The declination,  $\delta$ , of the perigee velocity vector is obtained from the relation:

$$\sin \delta = \sin (90^\circ - \omega) \sin i$$

$$\text{or} \quad \sin \delta = \cos \omega \sin i \quad (1)$$

The differential right ascension,  $\Delta\alpha$ , is determined from the relation:

$$\cos i = \tan \Delta\alpha \cot (90^\circ - \omega)$$

$$\text{or} \quad \tan \Delta\alpha = \tan \omega \cos i \quad (2)$$

To determine the right ascension,  $\alpha$ , of the perigee velocity vector, use the following table:

$\omega$	$\alpha$
$0 \leq \omega \leq 180^\circ$	$\mathcal{V} - \Delta\alpha$
$180 < \omega < 360$	$\mathcal{Q} - \Delta\alpha$

The celestial coordinates of the perigee velocity vector,  $\overline{\mathcal{V}}_p$ , are provided by the curves of figure 12.

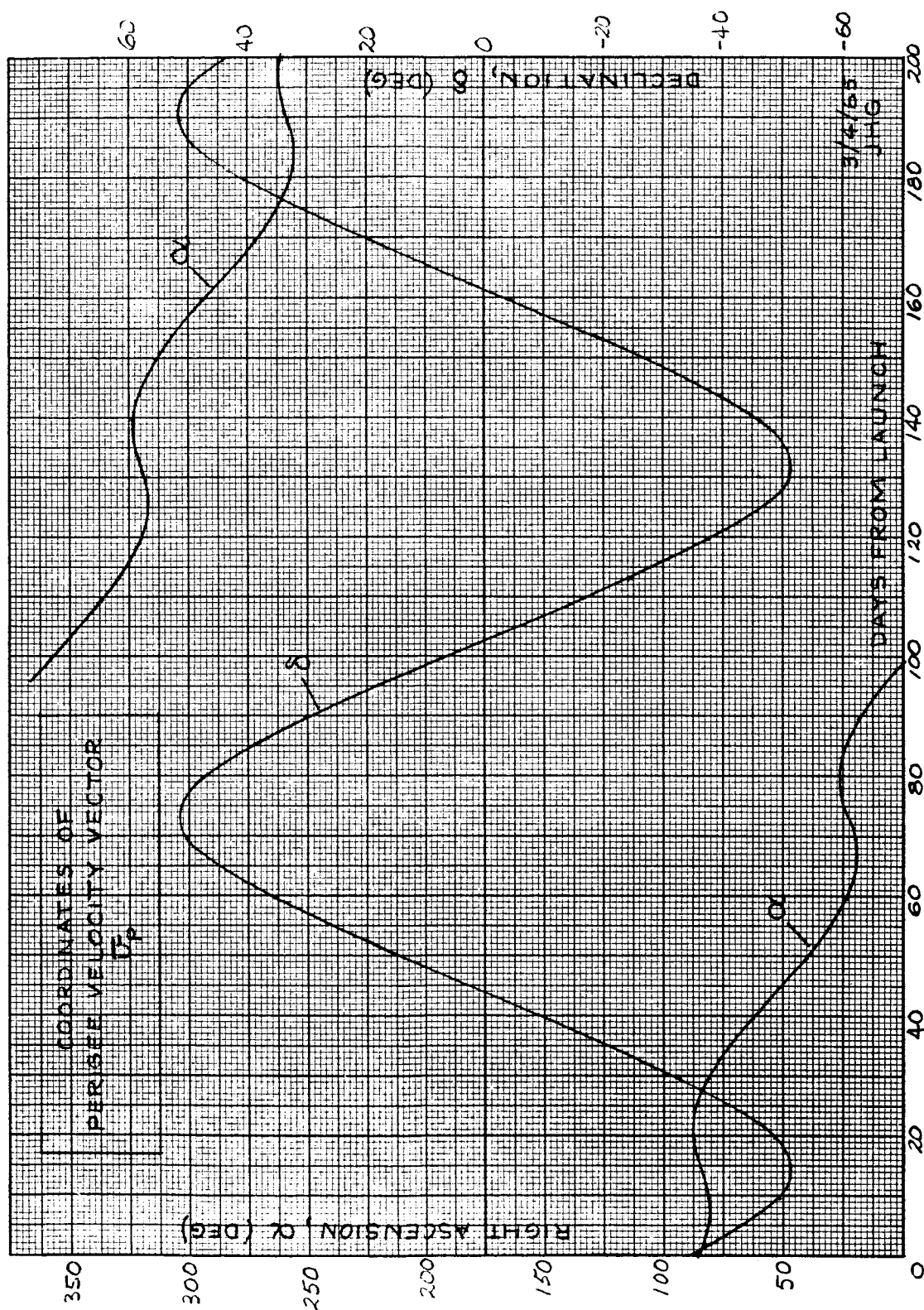


FIGURE 12 Coordinates Of Pergee Velocity Vector  $V_p$

### 2.2.7 Right Ascension of Ascending Node

Based on data supplied by the digital computer program of GSFC for the orbital performance of Ariel II, the arguments of the perigee and the right ascension of the ascending node are plotted in the curves of figure 13. This information is required in other areas.

### 2.2.8 Angle Between Initial Spin Axis and Perigee Velocity Vector

If we have two unit vectors,  $\bar{P}_i$ , described by celestial coordinates,  $\alpha_i$ , and  $\delta_i$ , the angle between these two vectors can be calculated using the relation:

$$\theta = \cos^{-1} (\sin \delta_1 \sin \delta_2 + \cos \delta_1 \cos \delta_2 \cos \Delta \alpha)$$

This relation is equivalent to:

$$\theta = \cos^{-1} (\bar{z}_0 \cdot \bar{U}_p)$$

where the initial orientation of the spin axis is:

$$\begin{aligned} \bar{z}_0 &= \begin{bmatrix} \alpha \\ \delta \end{bmatrix} \\ &= \begin{bmatrix} 90.8^\circ \\ -39.7^\circ \end{bmatrix} \end{aligned}$$

and  $\bar{U}_p$  is the unit vector of perigee velocity.

The angle between these two vectors is plotted in the curve of figure 14. This curve describes what the time variation of angle would be if the spacecraft maintained its original orientation in space.

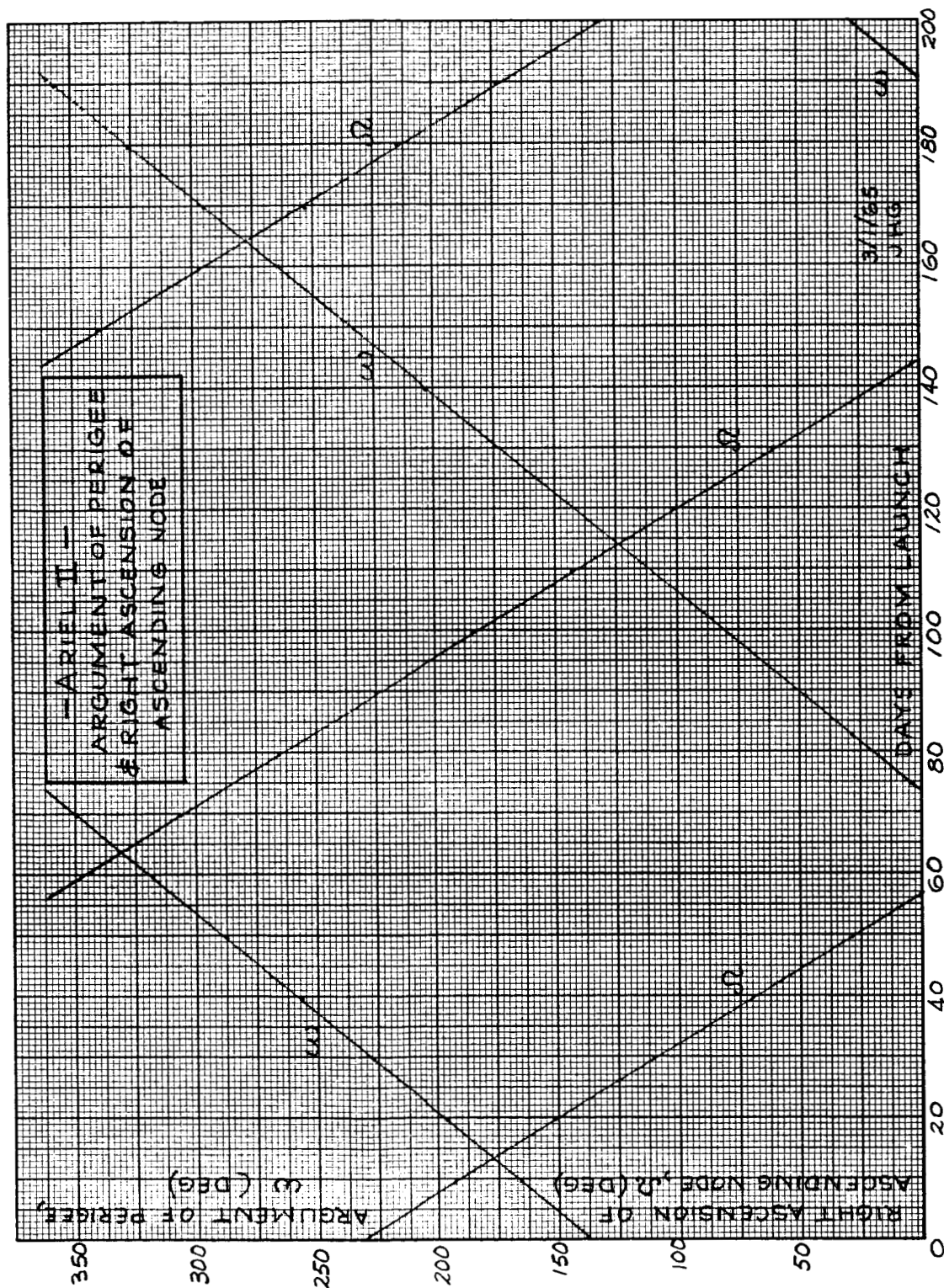


FIGURE 13 Ariel II Argument Of Perigee And Right Ascension Of Ascending Node



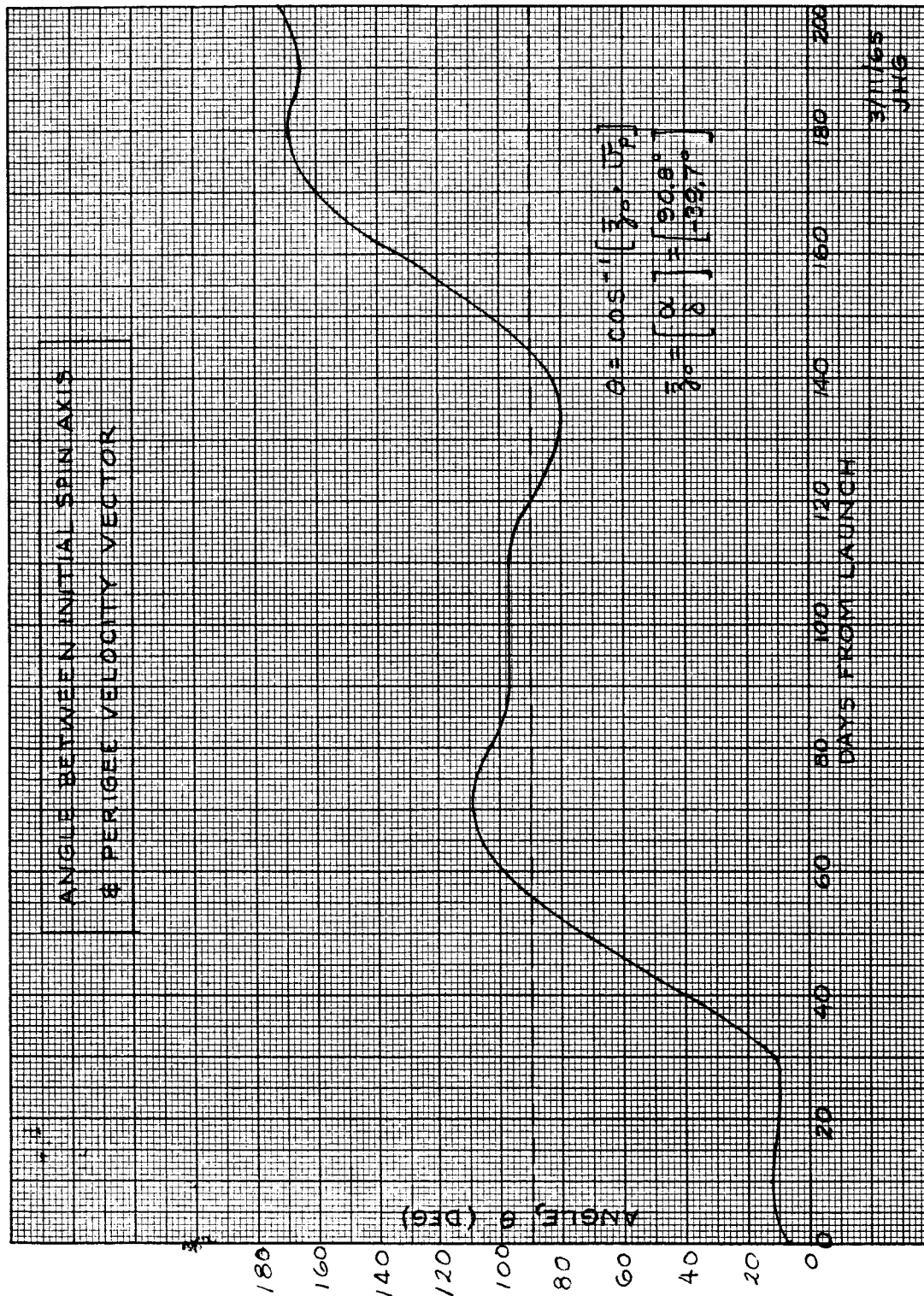


FIGURE 14 Angle Between Initial Spin Axis And Perigee Velocity Vector

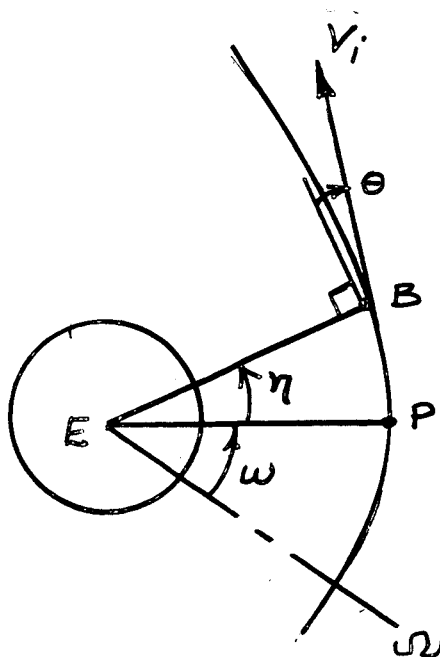


### 2.2.9 Initial Spacecraft Orientation

It is assumed that the initial direction of the spin axis of the spacecraft,  $\bar{z}_0$ , is aligned with the orbital velocity vector,  $\bar{v}_i$ , at the instant of insertion into orbit. The injection elements are:

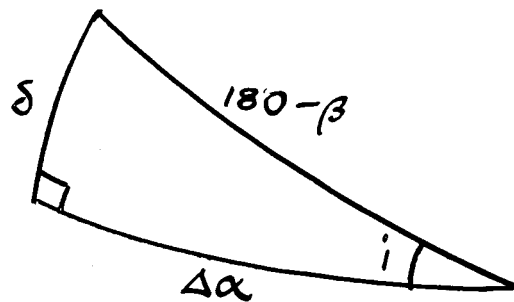
Element	Symbol	Angle (deg)
.Right ascension of ascending node	$\Omega$	229.8
.Argument of perigee	$\omega$	138.4
.True anomaly	$\eta$	6.5
.Flight path angle	$\theta$	0.4
.Inclination	$i$	51.66

These elements are indicated in the following diagram:



$$\begin{aligned}
 \text{Let } \beta &= \text{angle from } \Omega \text{ to } V_1 \\
 &= \omega + \eta + 90^\circ - \theta \\
 &= 138.4 + 6.5 + 90 - 0.4 \\
 &= 234.5 \text{ deg}
 \end{aligned}$$

Consider the spherical triangle:



$$\begin{aligned}
 \sin \delta &= \sin (180 - \beta) \sin i \\
 &= \sin \beta \sin i \\
 &= \sin 234.5^\circ \sin 51.66^\circ
 \end{aligned}$$

resulting in a declination of:

$$\delta = -39.7^\circ$$

$$\cos i = \tan \Delta\alpha \cot (180 - \beta)$$

$$\begin{aligned}
 \text{or } \tan \Delta\alpha &= -\cos i \tan \beta \\
 &= -\cos 51.66^\circ \tan 234.5^\circ \\
 &= -41.0 \text{ deg}
 \end{aligned}$$

The right ascension is then obtained:

$$\begin{aligned}
 \alpha &= \nu - \Delta\alpha \\
 &= 49.8 + 41.0 \\
 &= \underline{90.8 \text{ deg}}
 \end{aligned}$$

The initial orientation of the spacecraft spin axis in celestial coordinates is then:

$$\bar{\mathbf{z}}_0 = \begin{bmatrix} \alpha \\ \delta \end{bmatrix}$$

$$\bar{\mathbf{z}}_0 = \begin{bmatrix} 90.8^\circ \\ -39.7^\circ \end{bmatrix}$$

This initial orientation vector,  $\bar{\mathbf{z}}_0$ , coincides with other evidences of its initial celestial position.

### 2.3 Dynamical Conclusions and Recommendations

Two summary conclusions may be drawn about the dynamical performance of the Ariel II satellite on the basis of the information developed by phases 1 and 2 of the contract. The first of these was obvious before commencement of the study although as a result of the study more confidence may be placed in the magnitudes. The second conclusion was suspected prior to the study but study results have verified its existence and established magnitudes. These conclusions are:

- (1) Spin rate decayed from its initial value to zero with one large reversal over the 200 day interval. See figures 1 and 2.
- (2) Spin axis orientation is not fixed but experiences wide excursions. See figure 3.

Phase III of the program will seek to explain why the spacecraft performance in certain respects differed from anticipated performance.

The spacecraft spindown characteristic will be explained as largely an aerodynamic consideration.

The most probable trajectory of spin axis orientation will be determined by simultaneous solution of the solar aspect angle and the angle of attack deduced from the spin acceleration characteristics, since solar position and perigee velocity vector are known as functions of time.

Torques introduced by aerodynamic, gravity gradient, and solar pressure will be considered.

### 3.0 POWER SYSTEM PERFORMANCE

This section presents the results obtained from Phase II of the power system performance analysis for the UK-2/5-52 International Satellite. The purpose of Phase II is to define the actual performance of the power system and where possible, compare it to prelaunch predictions by use of graphical techniques. To accomplish this the following performance parameters are correlated using the data obtained from Phase I efforts (See Reference 1):

PP No.	Performance Parameter
04	+15 volts (regulated)
06	Dump Current
07	Unregulated Bus (Battery Voltage)
08	+12 Volts (regulated)
09	Solar Current
10	Battery Current
11	Battery Temperature
12	Paddle Temperature

In addition the following information is of interest:

Percentage of Sunlight/Days from Launch

Time of Sunlight Entrance and Exit

Aspect Angle/Days from Launch

Since the required data is only available periodically during the mission, the power system performance in the interim periods can not be defined with absolute certainty. As explained in the following sections, however,

sufficient data is available to generate a reasonably complete picture of actual system performance.

### 3.1 Regulated Voltages

The +12 and +15 volt regulated buses are examined to determine:

If a fault occurred

If an anomaly occurred

If one percent regulation requirements were met

If regulation varied with time, load or temperature

#### 3.1.1 Fault Determination

An ~~examination~~ of the +12 and +15 volt time profiles using the composite orbit graphs\* indicates that no permanent fault occurred. This is clearly shown by Figures 15 and 16 where the regulated voltages are plotted as a function of days from launch (DFL). A permanent fault would result in loss of data following its occurrence.

#### 3.1.2 Anomalous Occurrence

Through no permanent fault has been detected, an anomaly did occur in power system performance in orbit number 415. This is shown in Figures 17, 18, 19, 20, 21, 22, 23, 24, and 25. An appreciable drop in voltage occurs across the +12 and +15 volt buses so that regulation limits are exceeded for a period of 7 minutes.

---

\*"Composite Orbit" graphs referred to herein are documented in Reference 1.

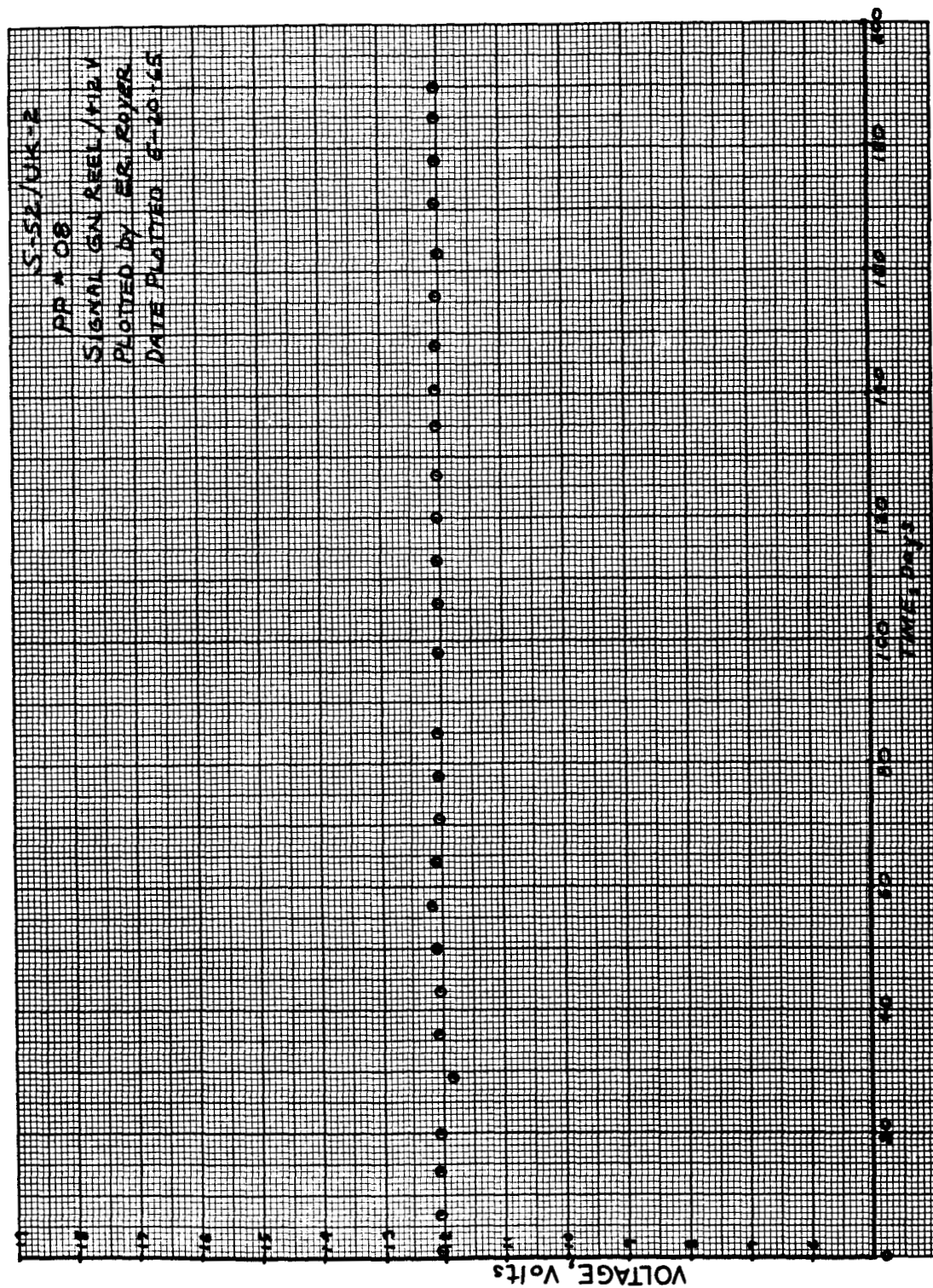


FIGURE 15

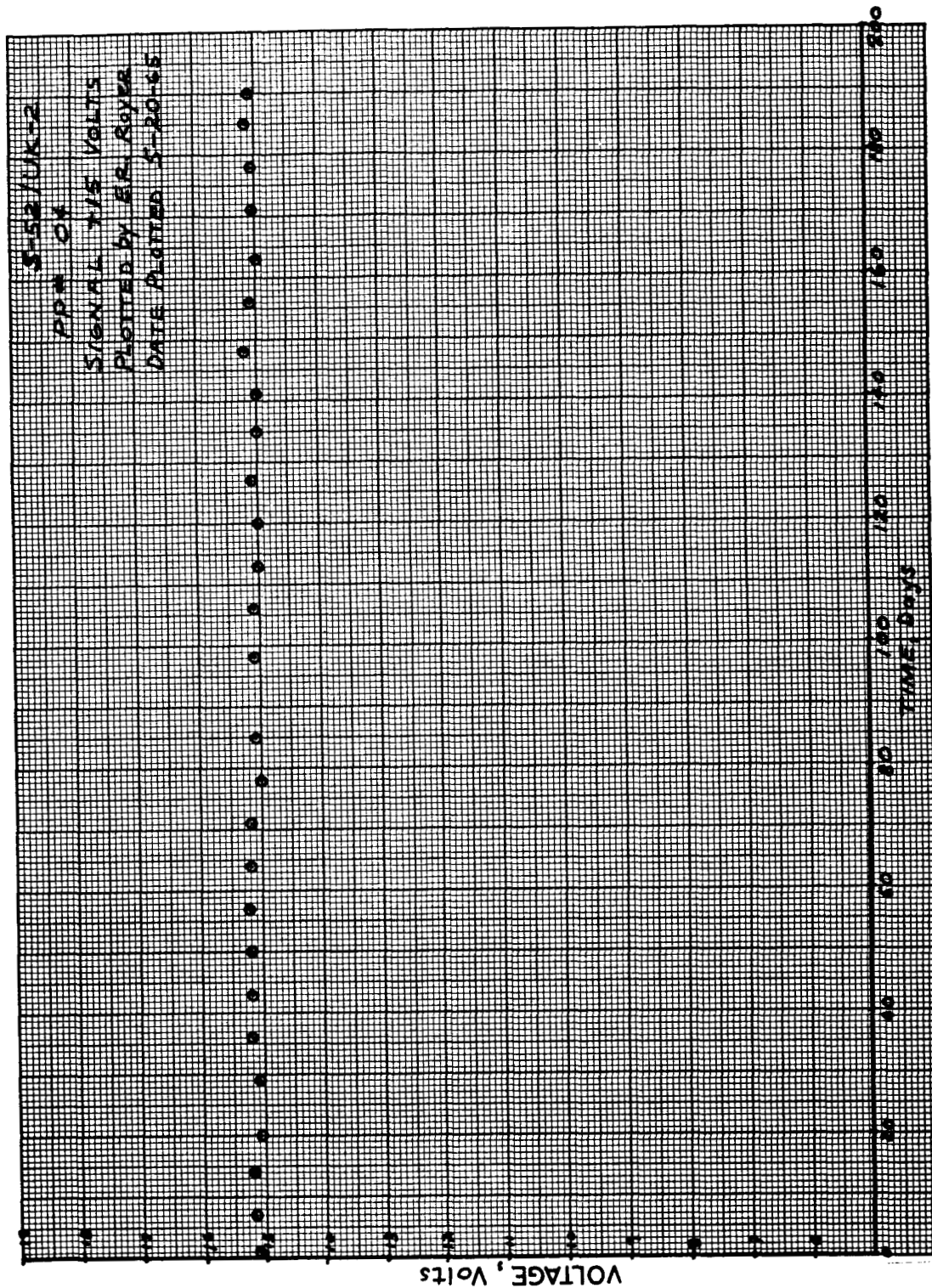


FIGURE 16



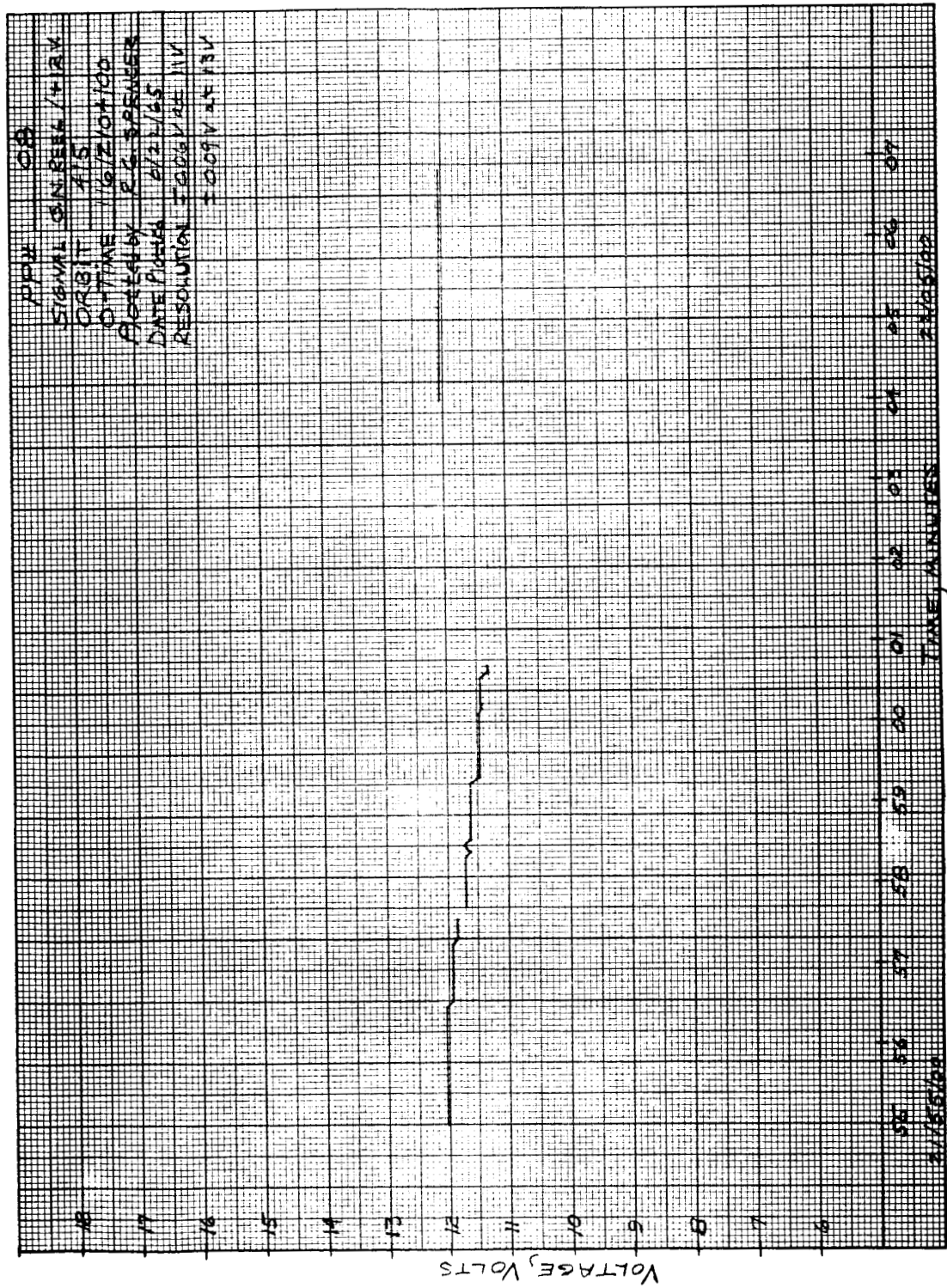


FIGURE 17

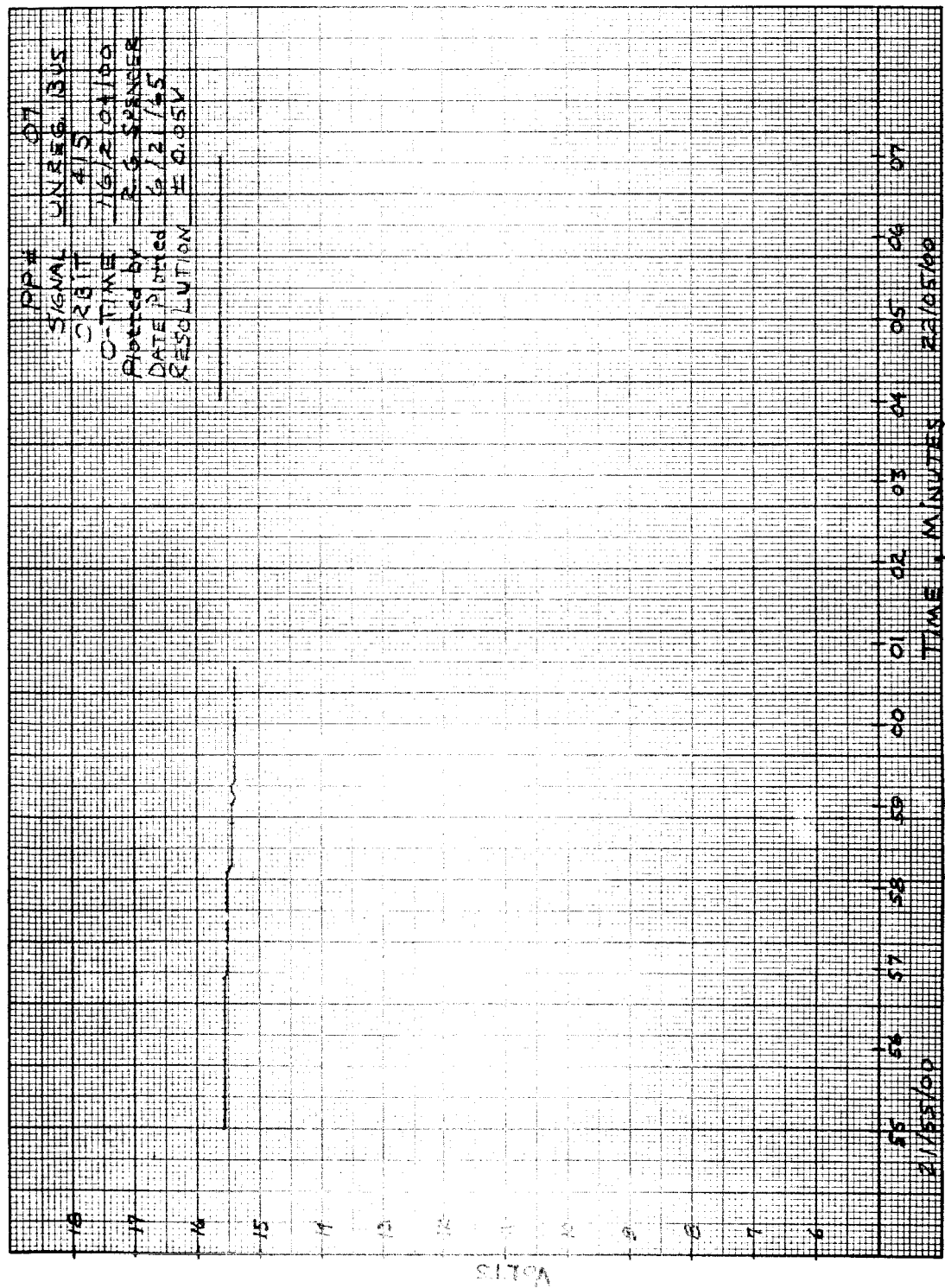


FIGURE 18

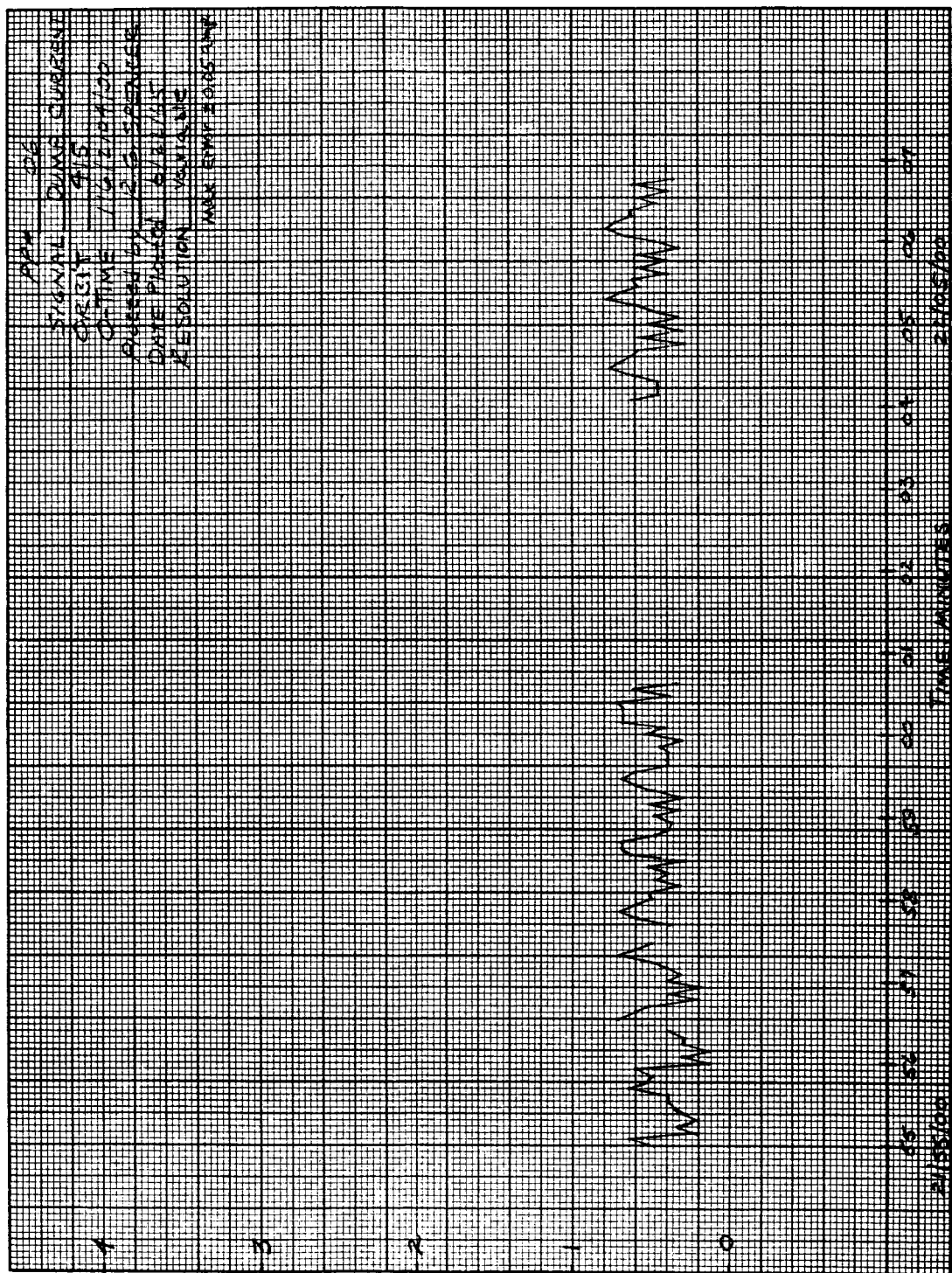


FIGURE 19

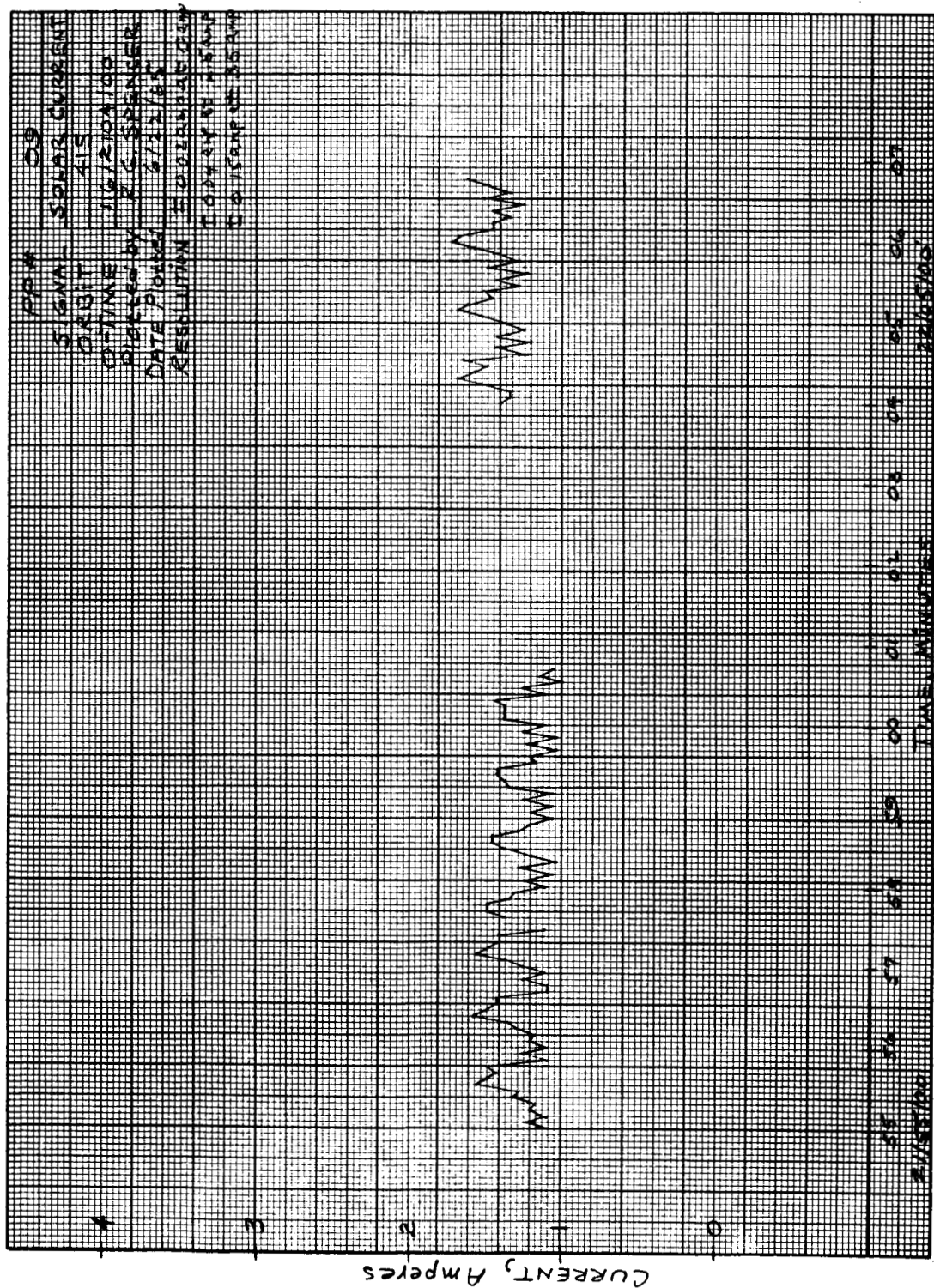


FIGURE 20



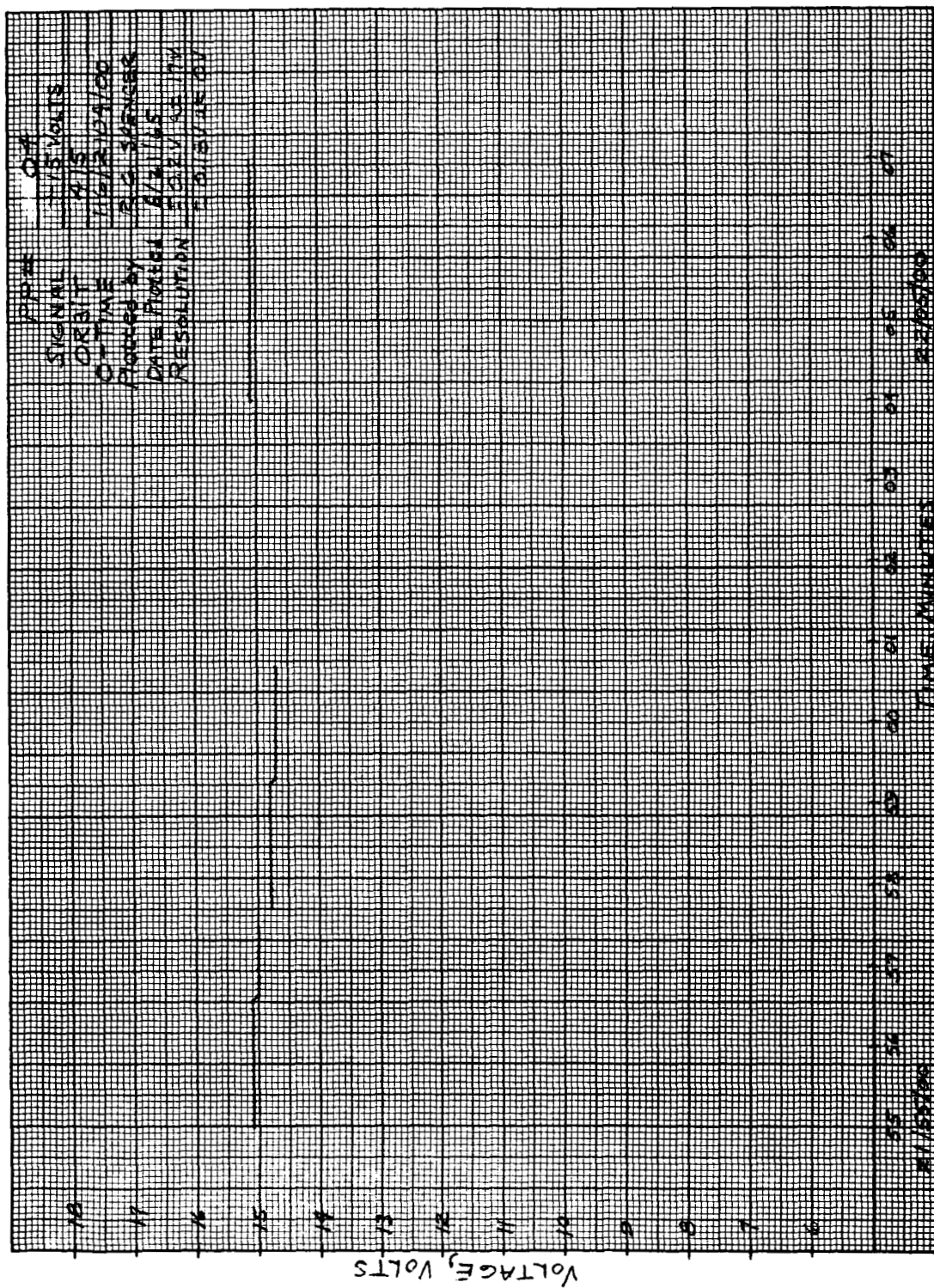


FIGURE 21

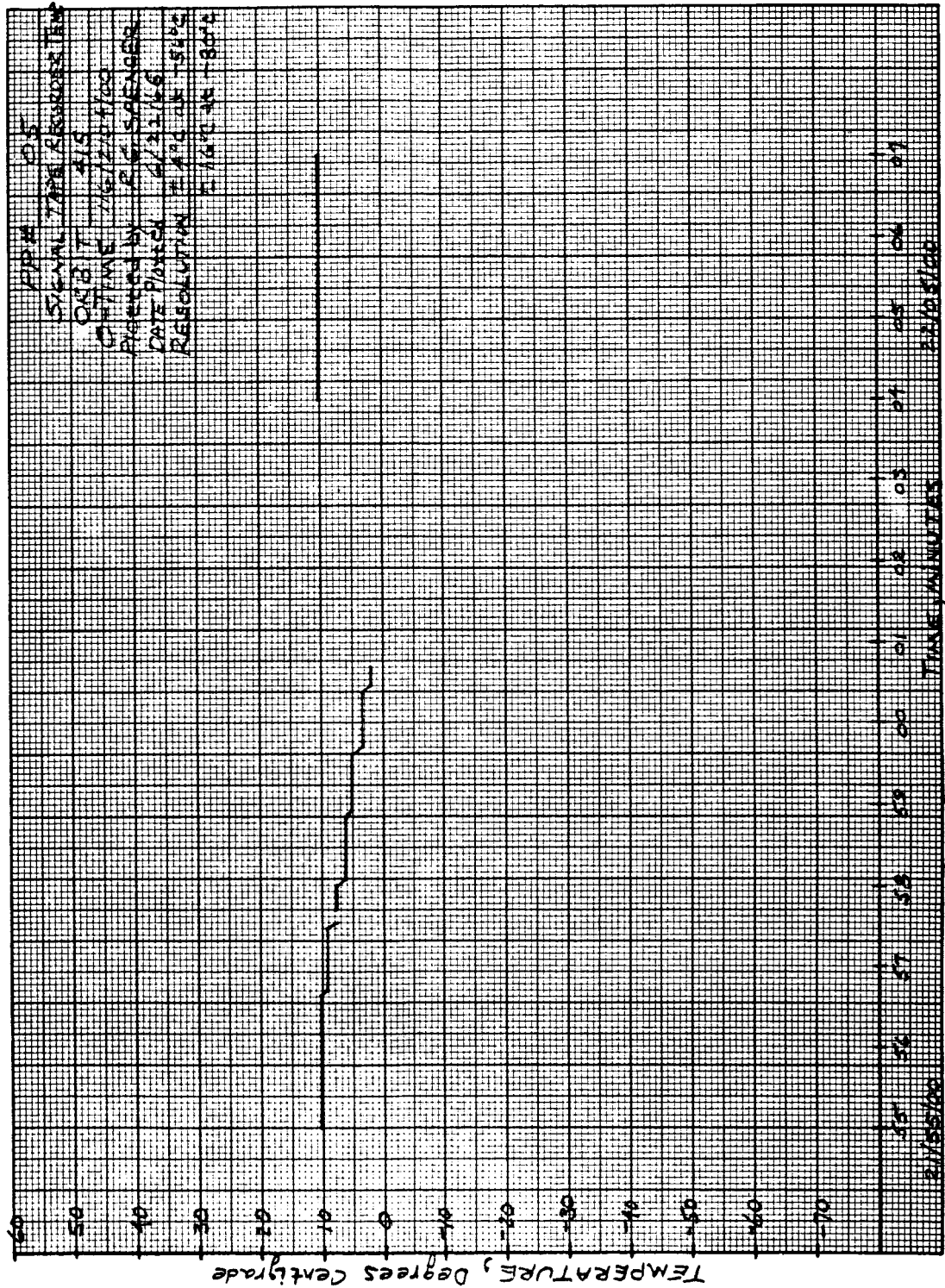


FIGURE 22

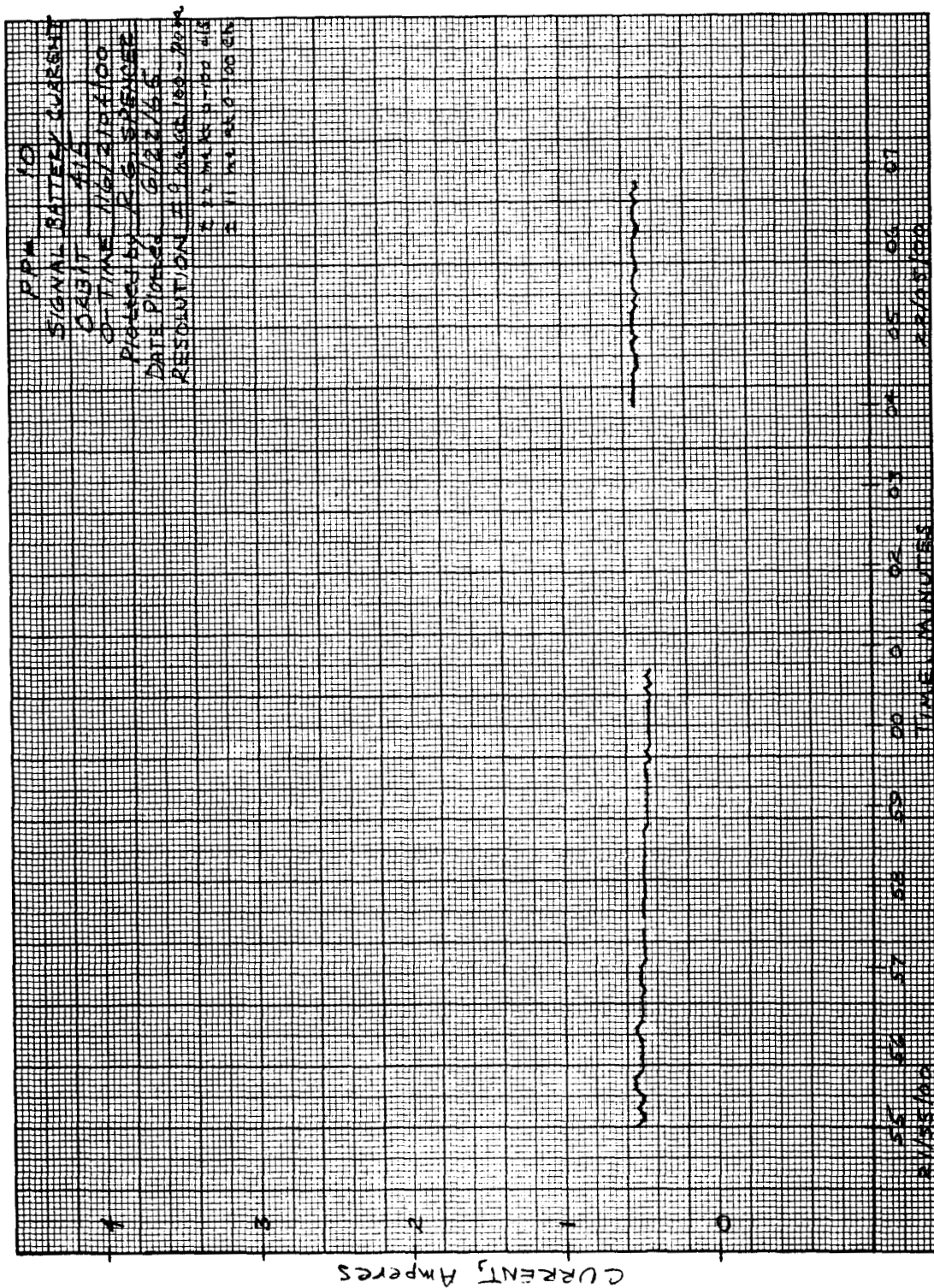


FIGURE 23

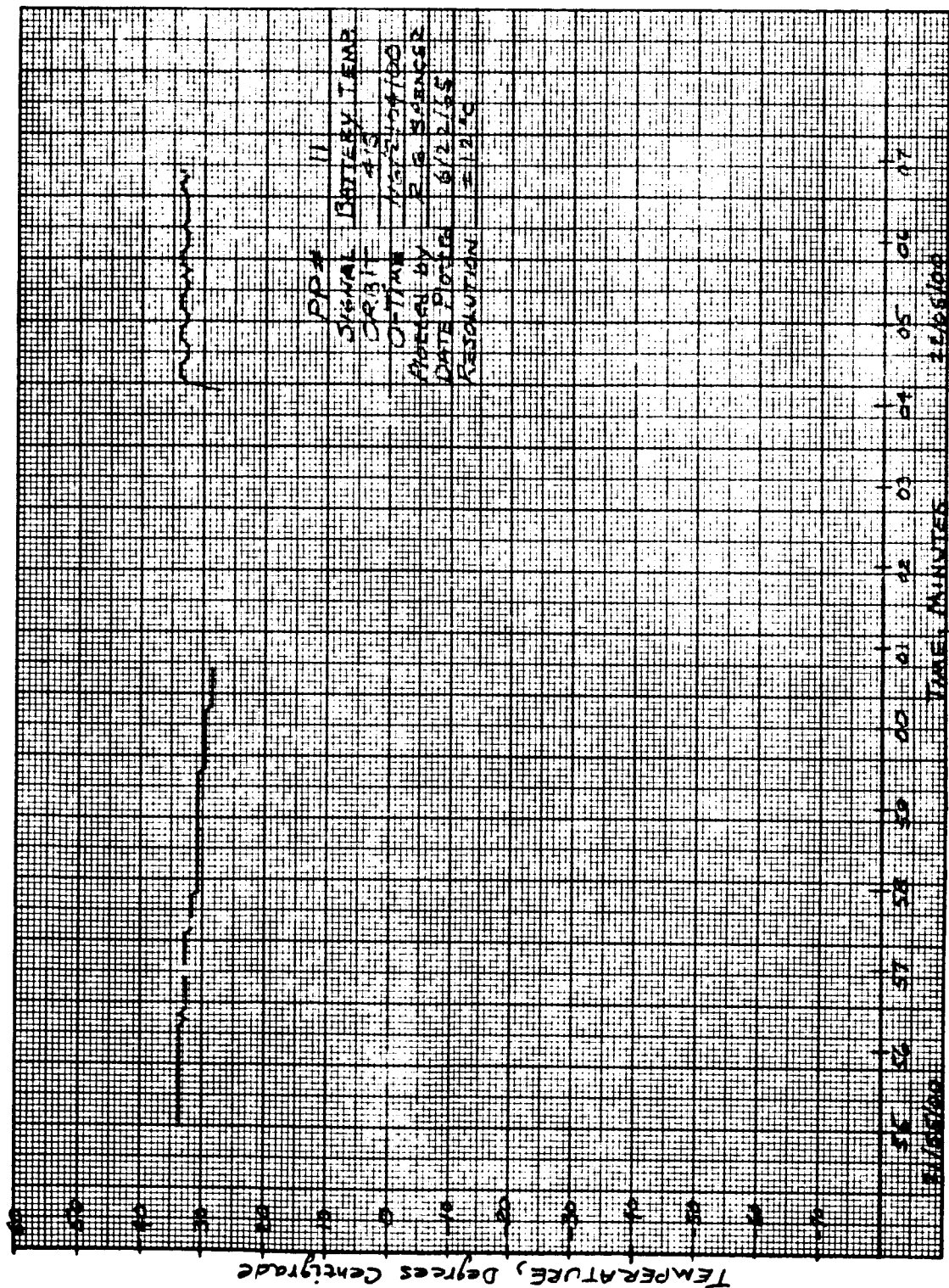


FIGURE 24



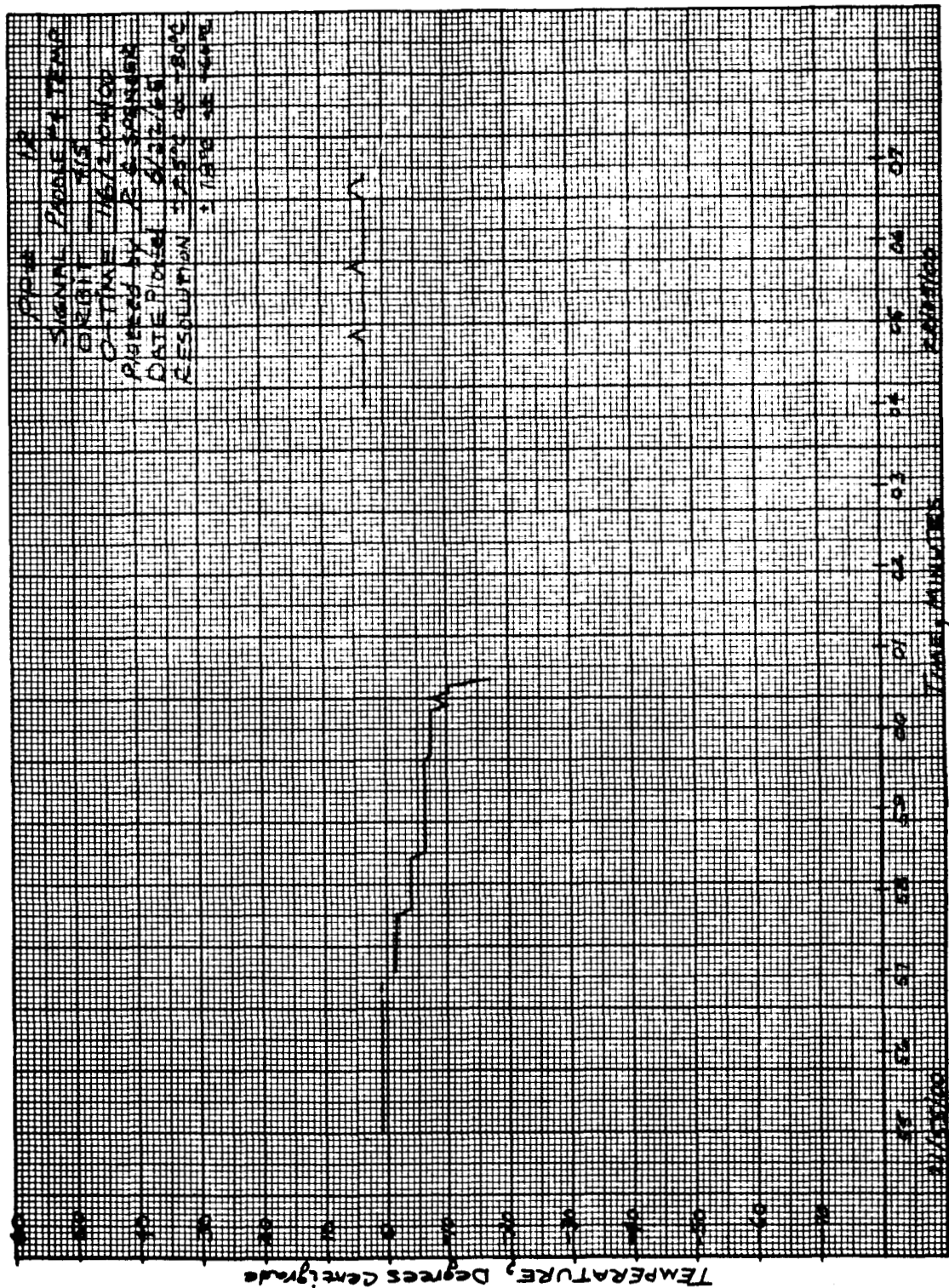


FIGURE 25

Since the temperature sensors are voltage sensitive, it is reasonable to assume that the temperatures recorded during this period decreased as a result of the temporary drop in voltages supplied by the power system. Furthermore, it does not appear from preliminary correlation of the current profiles that the power system was required to deliver an excessive load current which would have resulted in an inability to maintain the proper voltage levels. In Phase III this anomaly will be further examined in an attempt to determine its cause.

### 3.1.3 Regulation Requirements

An examination of the +12 and +15 volt time profiles in Figures 15 and 16 indicates maximum excursions of .15 and .2 volts respectively from the nominal regulation levels. Since the uncertainty in the telemetered data is  $\pm .1$  volt, however, this information can not be used to determine whether or not the one percent regulation limits were achieved. Further examination of Figures 15 and 16 clearly shows no degradation of regulation with time or temperatures encountered. Except for the anomaly in orbit number 415, regulation was not affected by any load variations encountered.

### 3.2 Battery Performance

The battery voltage, current and temperature time profiles are examined to:

- Determine if an undervoltage condition occurred
- Estimate the maximum discharge level
- Determine if charge current was regulated and if overvoltage limiting was accomplished
- Determine if any degradation in battery performance occurred

and if so, can it be related to time, load or temperature

- Did battery temperature exceed design limits?

### 3.2.1 Undervoltage Determination

An undervoltage condition occurs when the terminal voltage of the line battery drops below 12.5 volts. When this condition is reached the battery load is disconnected by an "undervoltage" relay and the terminal voltages of the line and redundant batteries are compared. If the voltage of the redundant battery exceeds that of the line battery by  $0.8 \pm 0.1$  volts, then the redundant battery is transferred to the load bus. On the other hand, should the terminal voltage of the redundant battery not exceed the line battery by the required (+) differential voltage, no transfer occurs. The appropriate battery is then charged for an 18 hour period during which time no telemetry data is transmitted. After this period the battery load is again connected via the undervoltage relay.

From the Phase I data available it can not be stated with absolute certainty that an undervoltage condition did not occur. Examination of the battery voltage as a function of DFL (See Figure 26), however, reveals no significant decrease in the output level.\* In fact the minimum value always exceeds 13.7 volts. It is reasonable to assume, therefore, that an undervoltage condition did not occur. Thus, it appears that the redundant battery was not employed.

### 3.2.2 Maximum Discharge Level

The depth of discharge during a single satellite night was not expected to exceed 12 percent of capacity. An examination of the battery current time profile using the composite orbit graphs verified this prediction.

\*That is, no large, steady decline is evident.

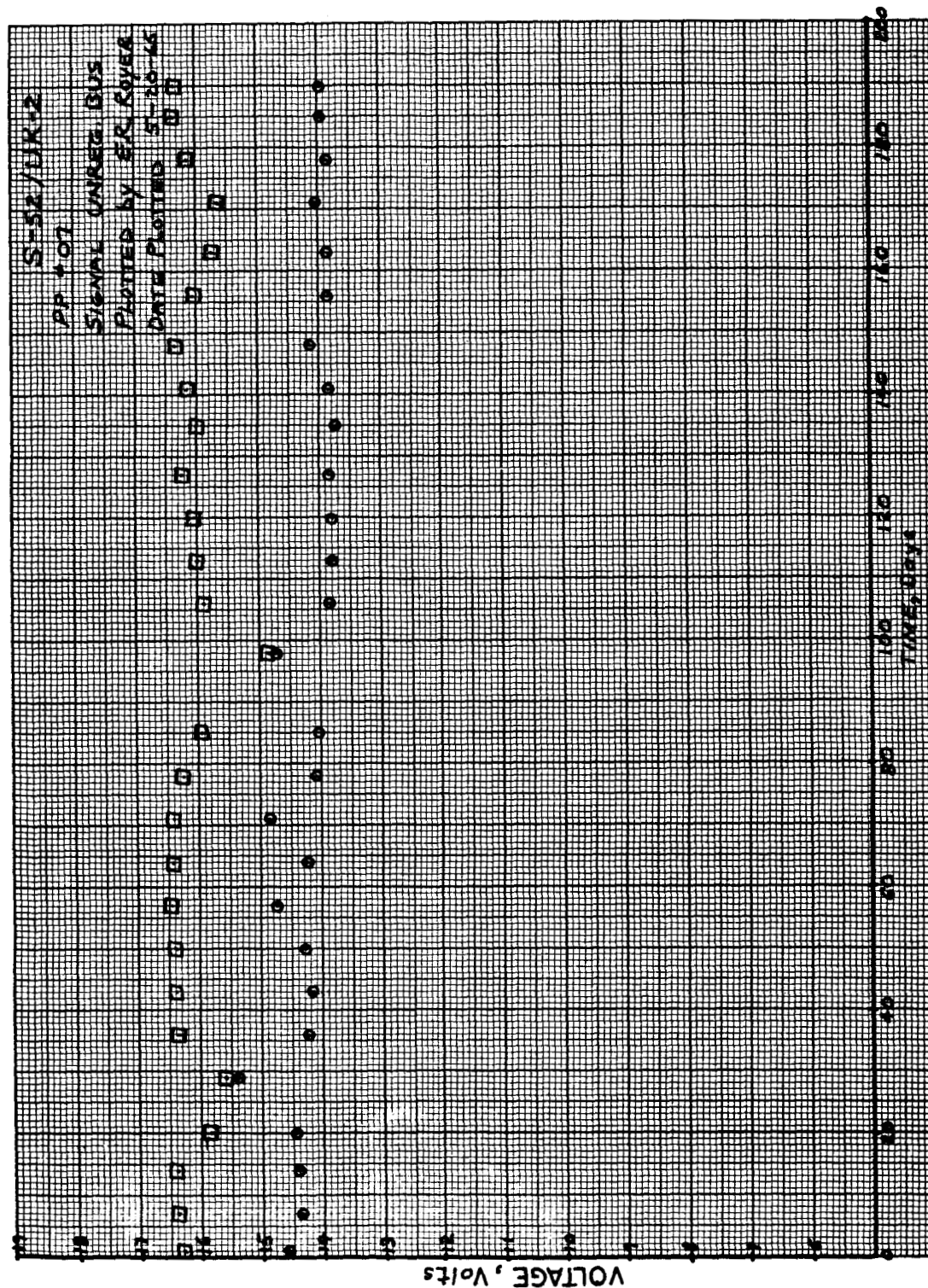


FIGURE 26

Assuming a battery capacity of 3.25 ampere-hours, the maximum level of discharge was approximately 9.24 percent. This condition occurred 79 or 80 days after launch.

### 3.2.3 Charging Current Regulation

The method of battery charging and protection employs a proportional shunt regulator. Normally, charging current was to be regulated within two percent of 500 milliamperes. An examination of the charging current time profile in Figure 27, indicates that the regulation limit was exceeded at various points.\* The largest excursions from nominal occurred in the interval from 35 to 65 days after launch. The maximum deviation from nominal was 100 milliamperes. Figure 28 indicates that the battery was subjected to very low temperatures during this period. Thus, the regulated level of charging current appears to decrease in a low temperature environment (ie. below zero degrees centigrade). This is not undesirable, however, since battery charging efficiency is significantly higher in a low temperature environment. The degree of regulation achieved is not affected by variations in time or load.

In addition to battery protection realized by regulating the charging current, further protection was provided by limiting the terminal voltage at 16.5 volts. This was to be accomplished by reducing the charging current. Two instances in which voltage limiting occurred are depicted in Figures 29, 30, 31, and 32, 33, and 34. From these cases it is evident that voltage limiting was activated at 16.4 volts. It should be noted that the terminal voltage is very responsive to a reduction in charging

---

\*Charging current is treated as positive in this analysis

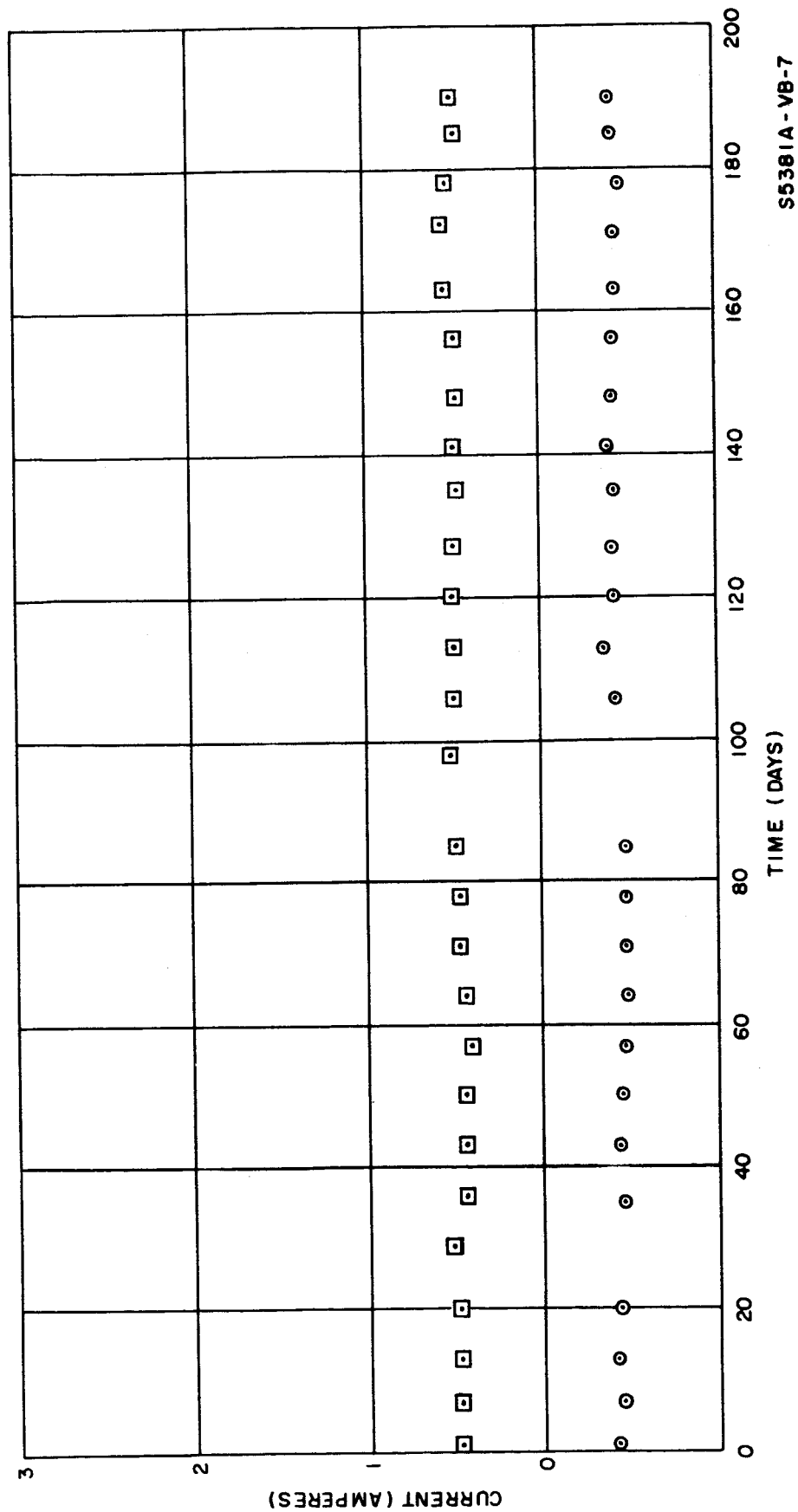


FIGURE 27 - PP #10 Battery Current



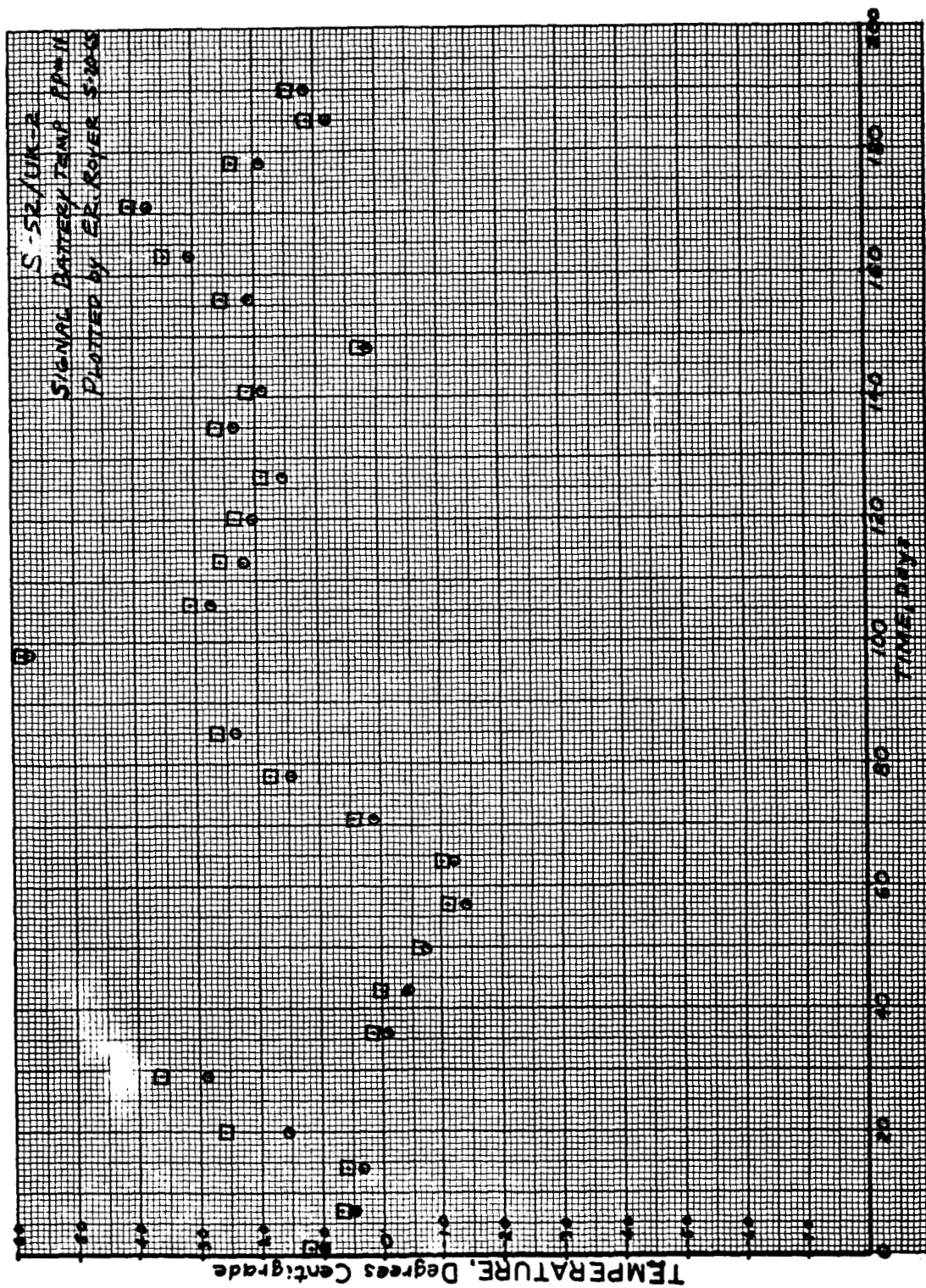


FIGURE 28

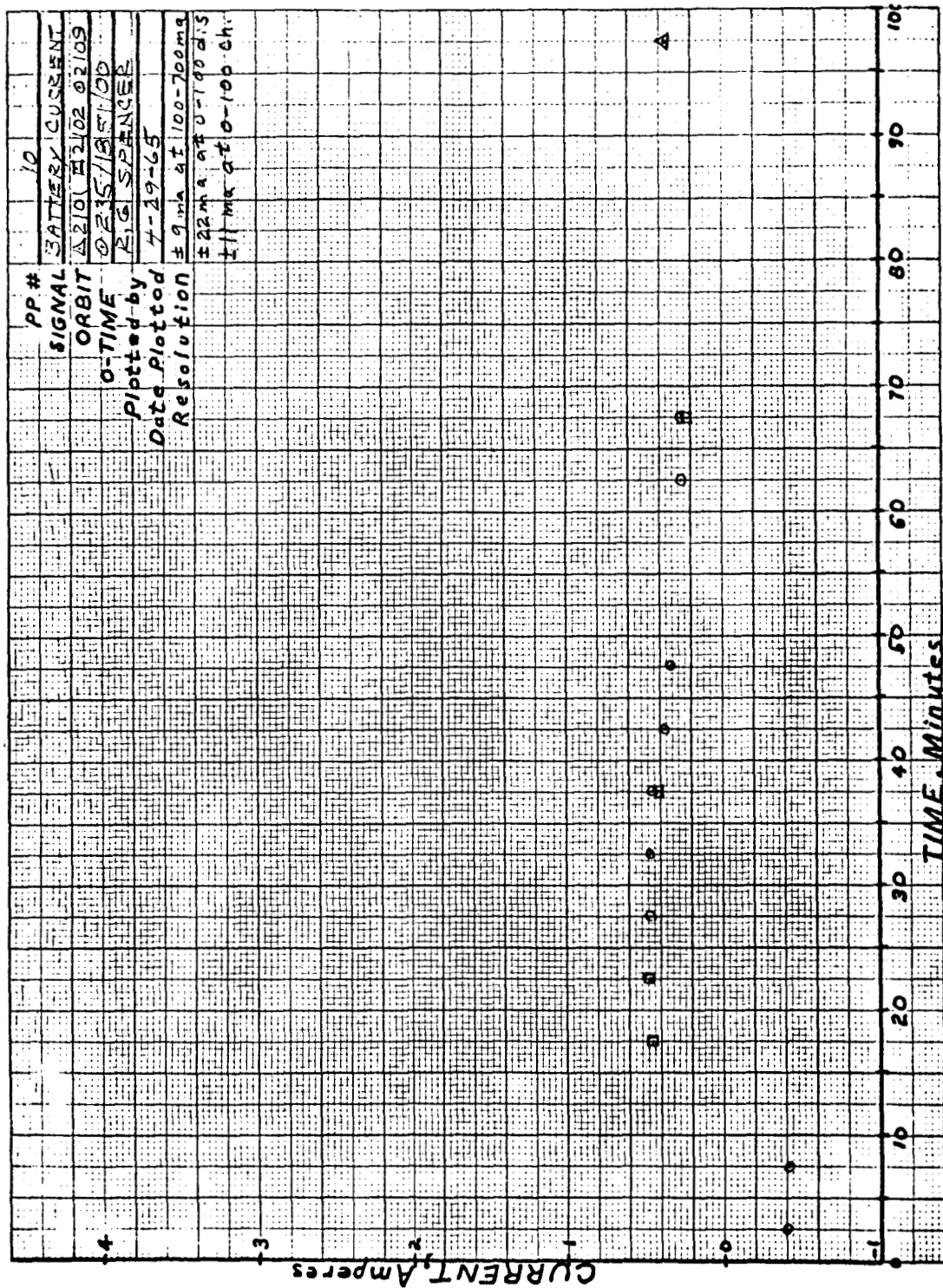


FIGURE 29



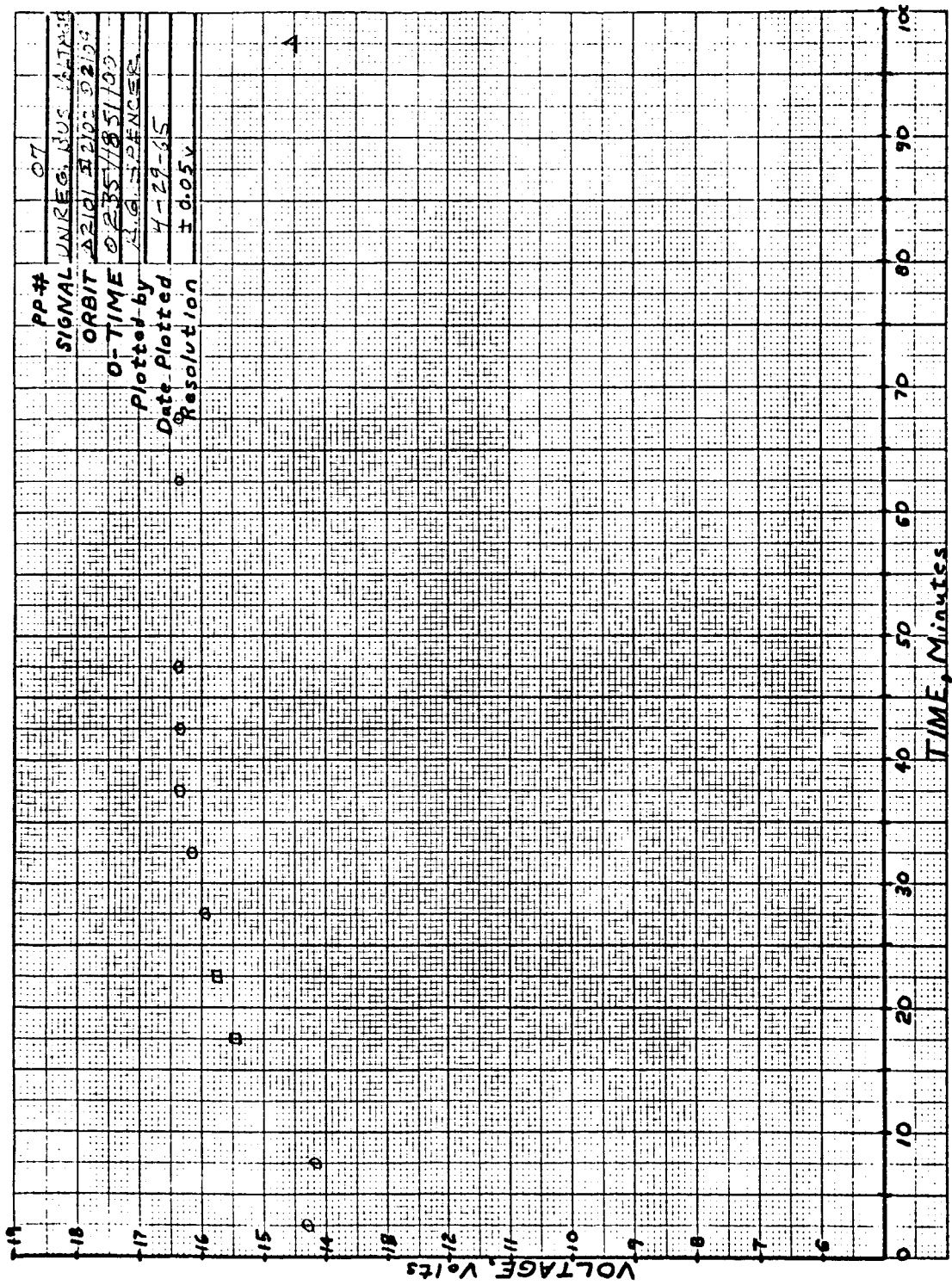


FIGURE 30

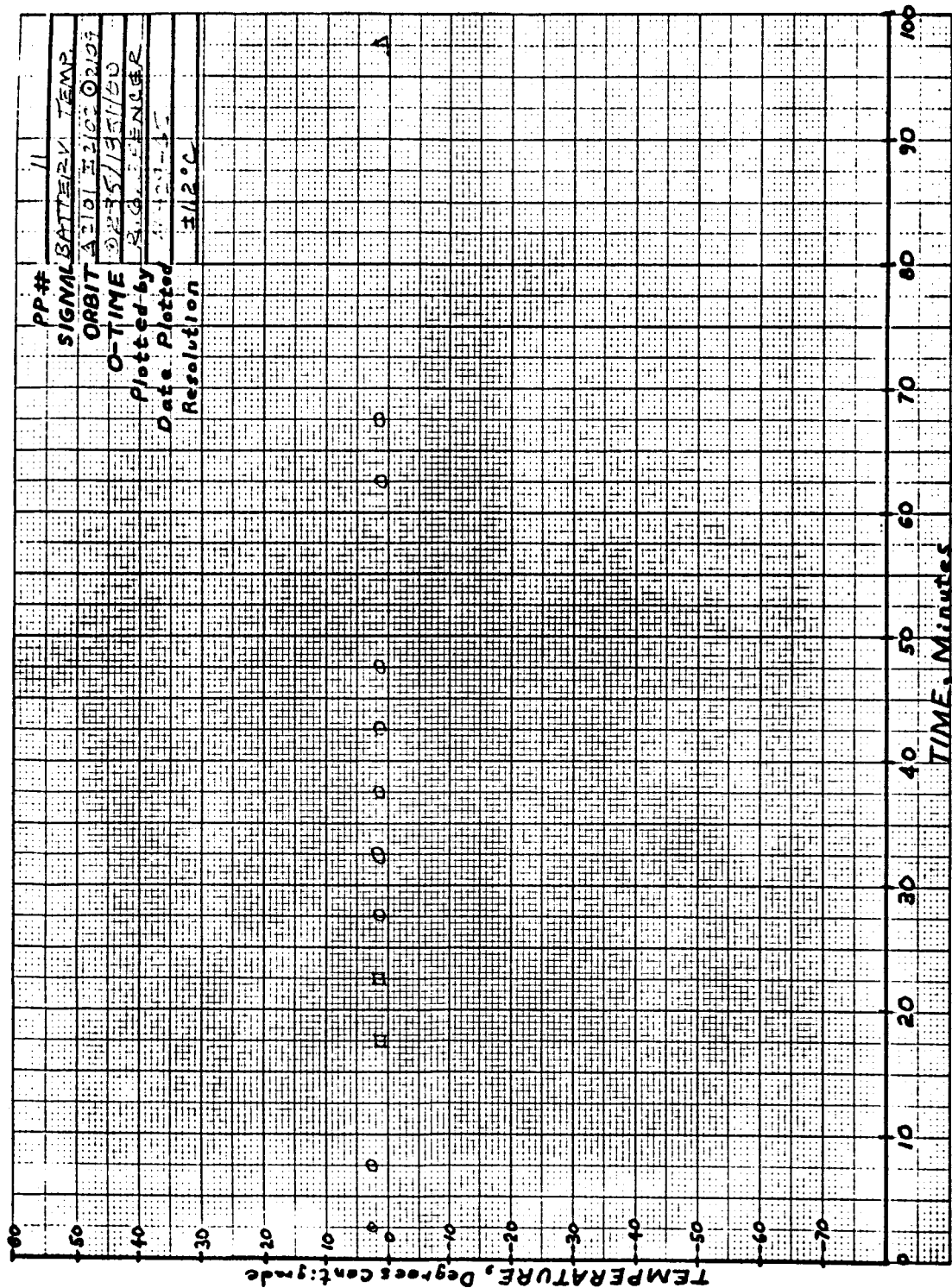


FIGURE 31

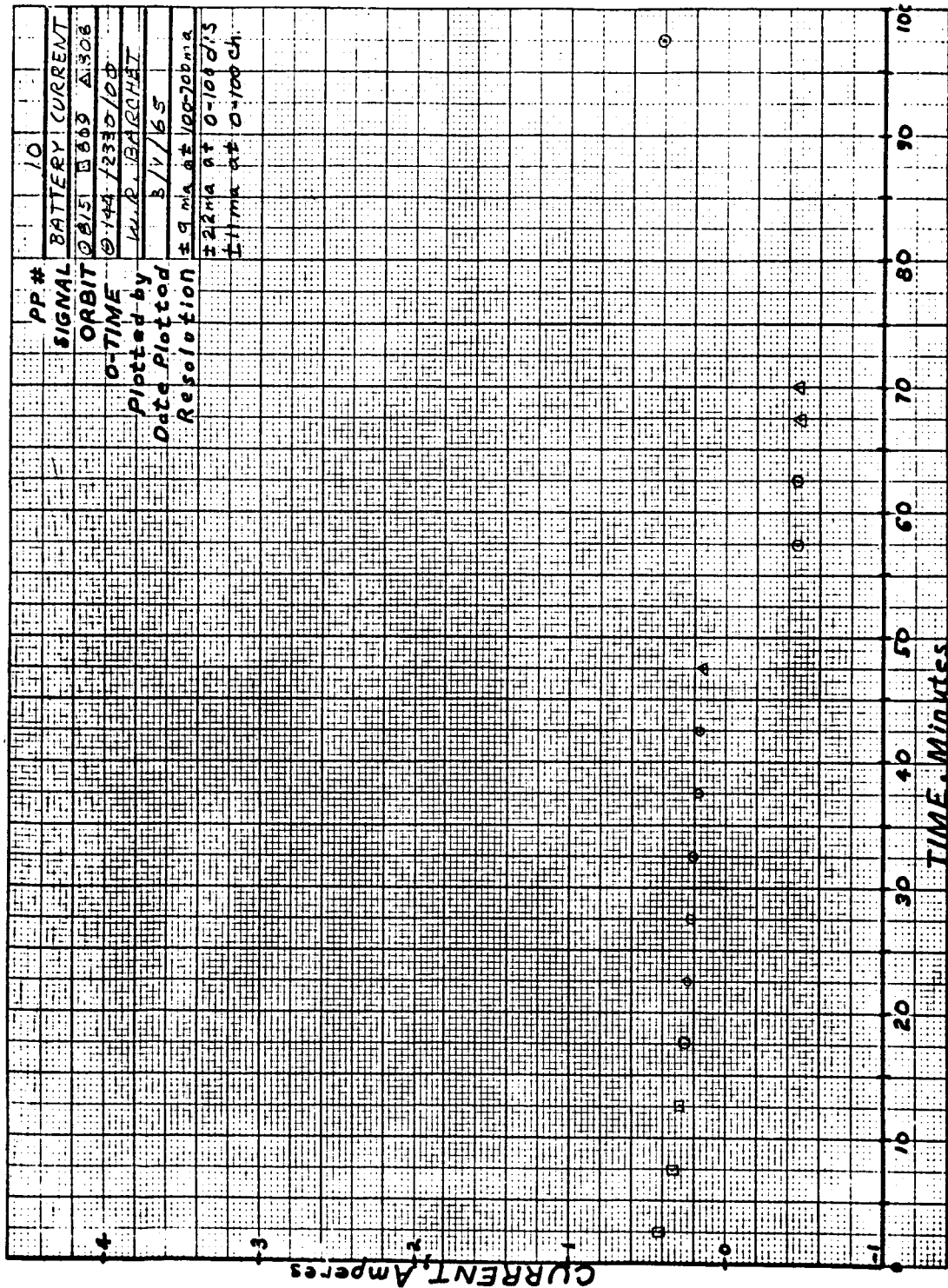


FIGURE 32

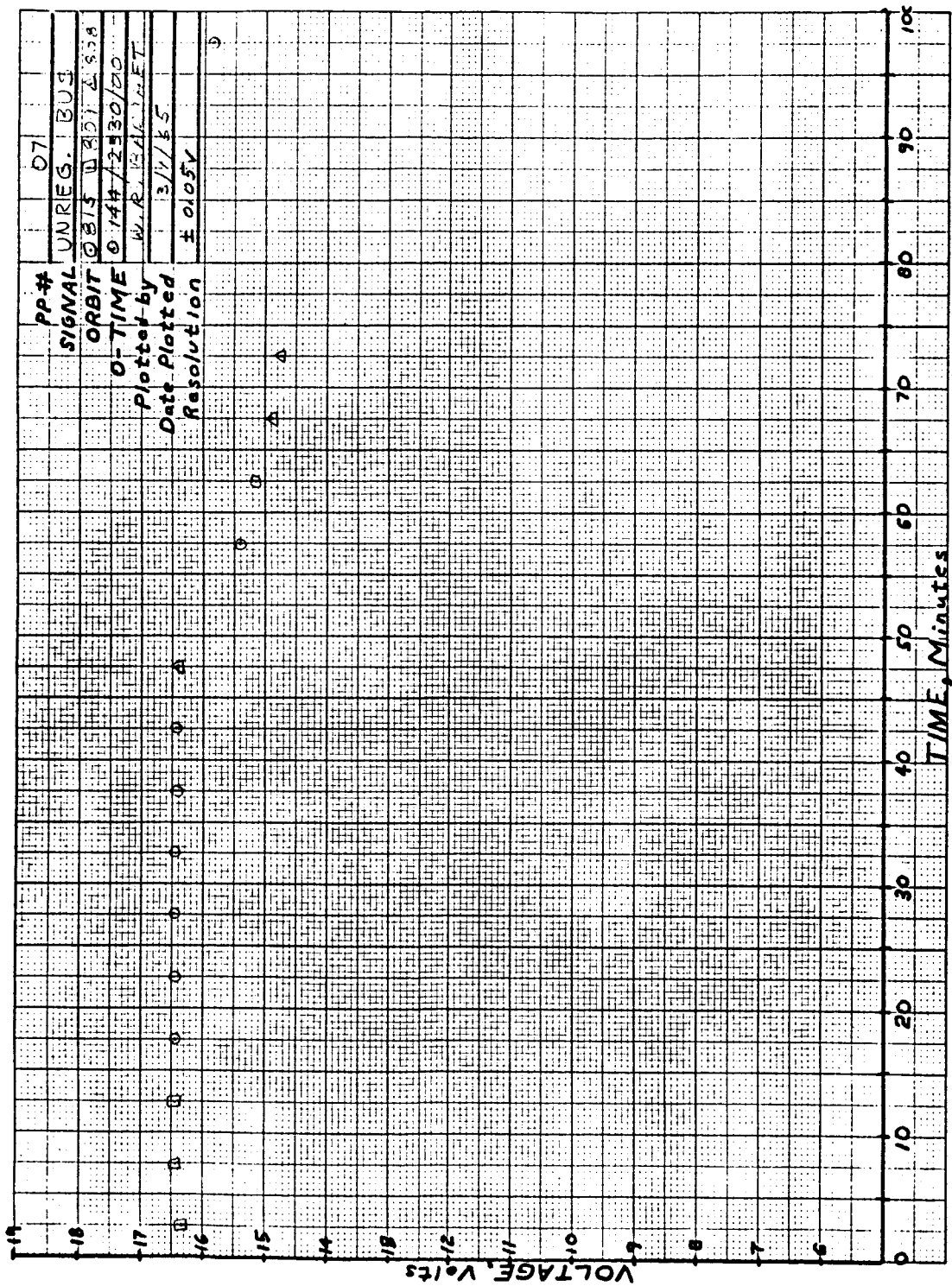


FIGURE 33

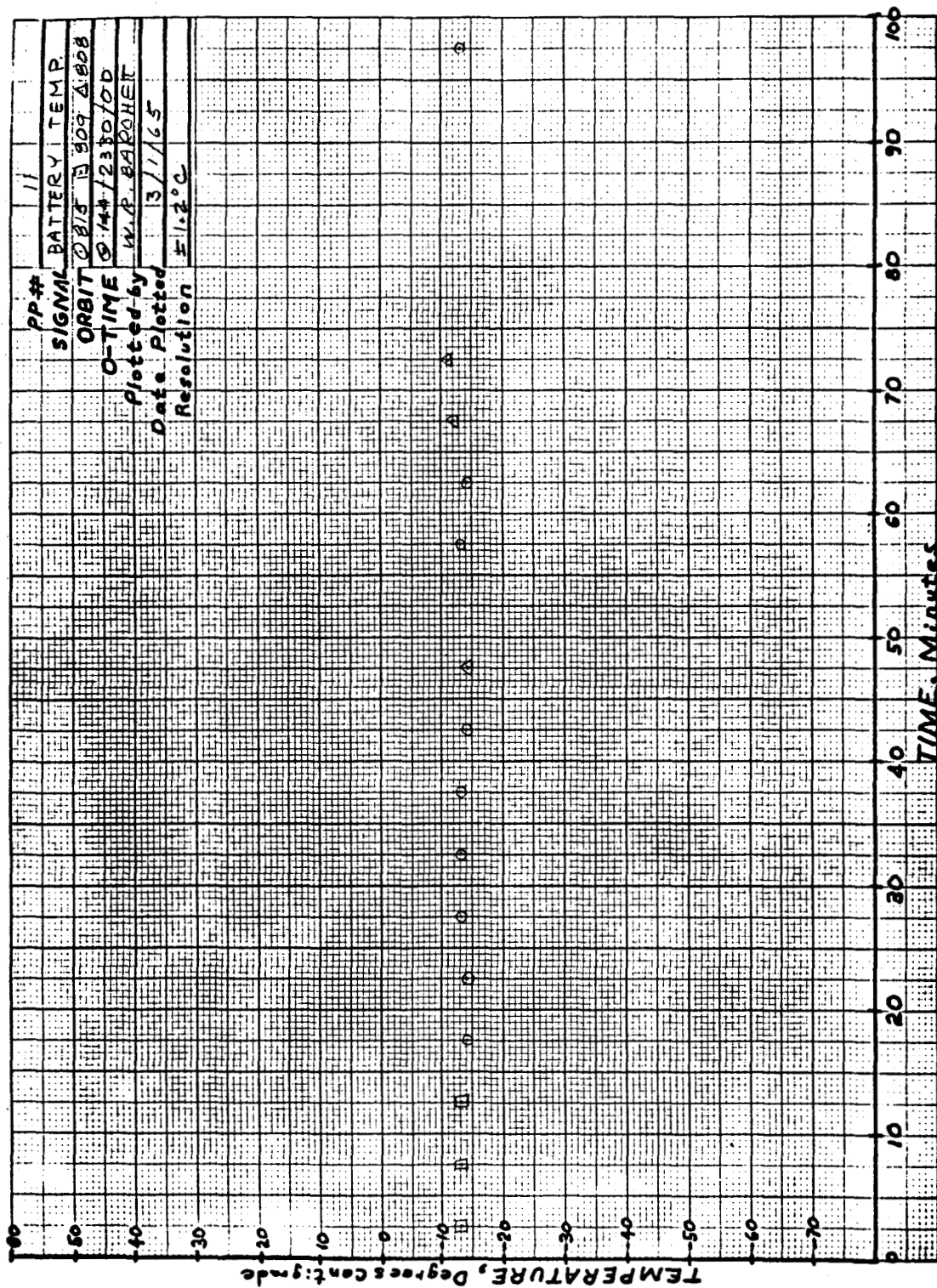


FIGURE 34

current. These cases also demonstrate the sensitivity of the charging current regulation level to low temperatures.

#### 3.2.4 Degradation Determination

In this analysis the battery discharge current time profile in Figure 27 is used as a measure of degradation in battery performance.\* Since no significant decline in output level is evident, it is reasonable to assume that no measurable degradation occurred.

#### 3.2.5 Battery Temperature

The range of ambient operating temperatures for the battery was specified prior to launch as  $-50^{\circ}$  to  $+400^{\circ}$ . Nominal ambient operating temperature is  $+250^{\circ}$ . It is evident from Figure 28 that the actual range of operating temperatures encountered was  $-150^{\circ}$  to  $+590^{\circ}$ . Since no permanent fault or degradation has been detected, however, it is reasonable to conclude that the battery can operate properly in the temperature environment encountered.

### 3.3 Solar Array Performance

In the following discussion of solar array performance unregulated bus voltage is treated as terminal voltage of the solar array. This constitutes a negligible error since the voltage difference is approximately constant at .2 volts.

#### 3.3.1 Minimum Power Requirement

The minimum power requirement of the S-52 satellite during daylight periods is approximately 14 watts. Power available from the solar array was expected to exceed this level, with aspect ratios greater than

---

\*Battery discharge current is negative in this analysis.

30 degrees, for a period of at least one year. An examination of the composite orbit graphs indicates that this requirement was met except during orbit number 704. During this period the available power profile is approximately that shown in Figure 35. It is evident from this data that the available power is less than 14.0 watts prior to the nighttime portion of the orbit.\* For the purposes of Phase III efforts in explaining this anomaly the solar current, solar voltage, dump current, battery current, paddle temperature and aspect ratio profiles are presented in Figures 36, 37, 38, 39, 40, and 3 respectively.

#### 3.3.2 Maximum Power Output

The maximum power output of the solar array was expected to approach 30 watts at the most favorable aspect ratio. An examination of the composite orbit graphs indicates that maximum power delivery occurred in orbit number 1,799 at an aspect ratio of 93 degrees. The output exceeded the expected level by 13.5 watts.

#### 3.4 Recommended Efforts For Phase III

Phase III will consist of an effort to develop theoretical bases for defining the departure of actual power system performance from prelaunch predictions. More specifically, the following areas should be investigated:

- (1) Anomalous behavior of all telemetered performance parameters in orbit number 415.
- (2) Anomalous behavior of available power output during orbital daylight in orbit number 704

---

\*A favorable aspect ratio of 147 degrees existed during the orbit.

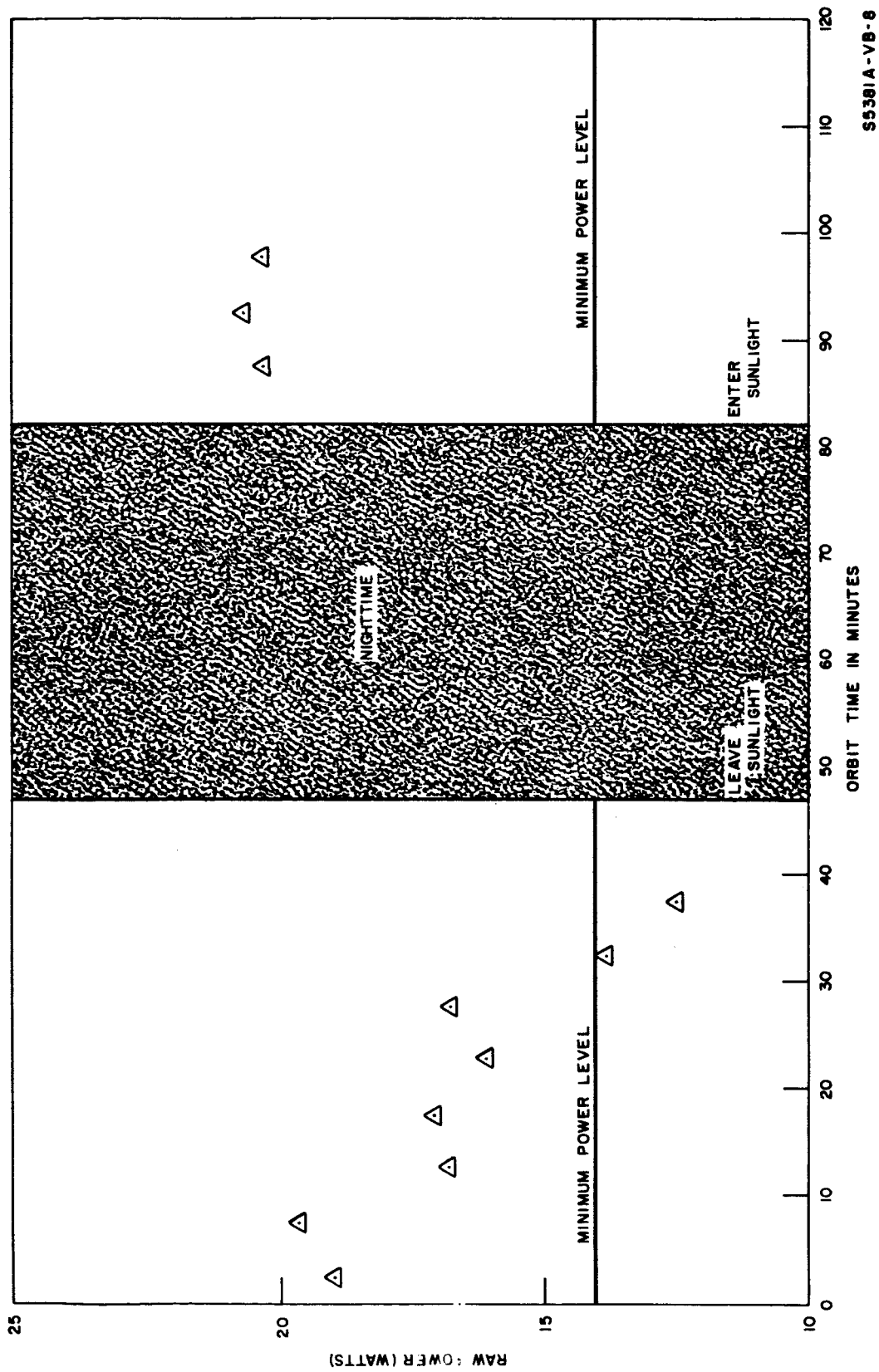


FIGURE 35 Available Power Profile, Orbit 704



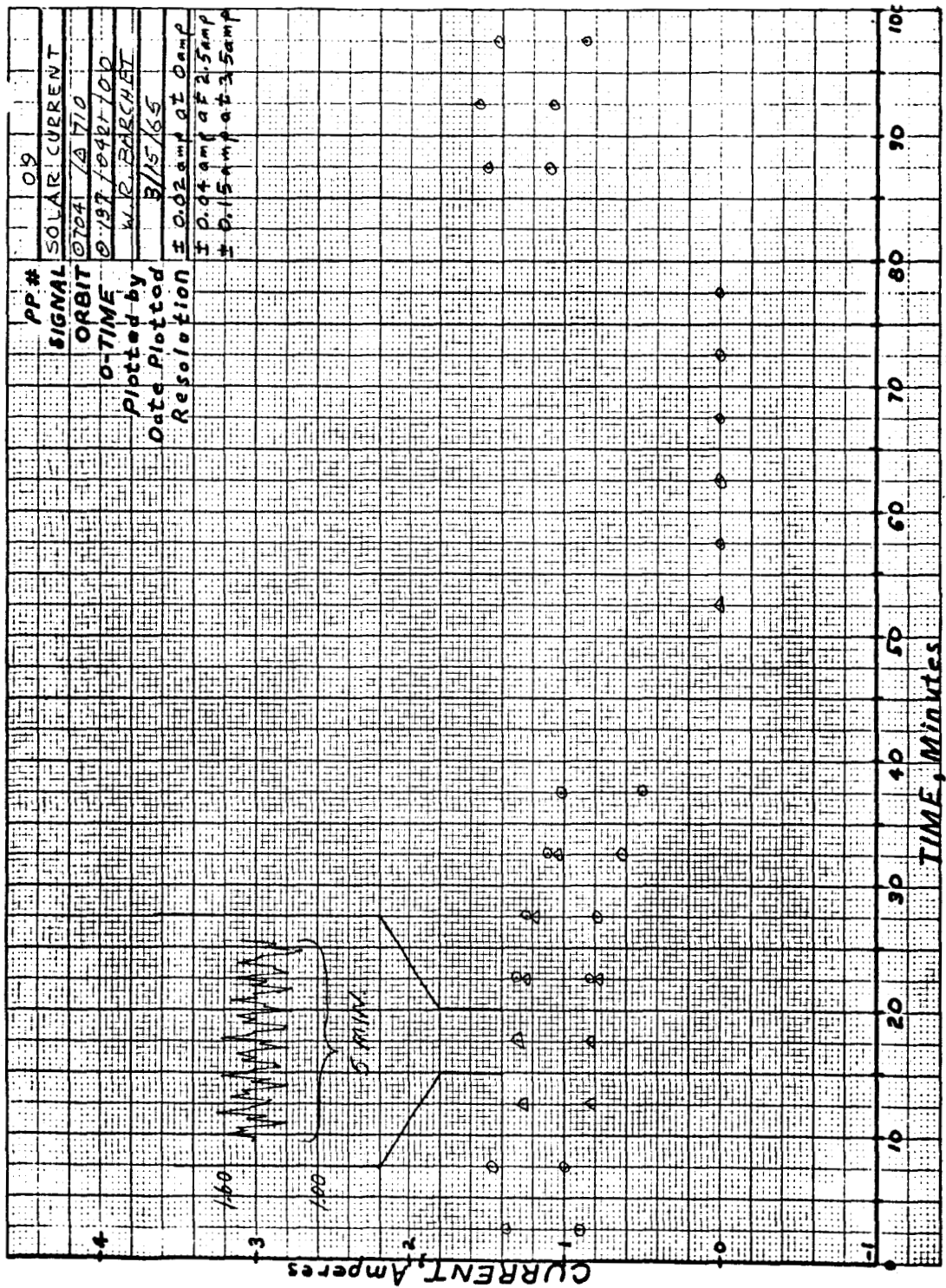


FIGURE 36

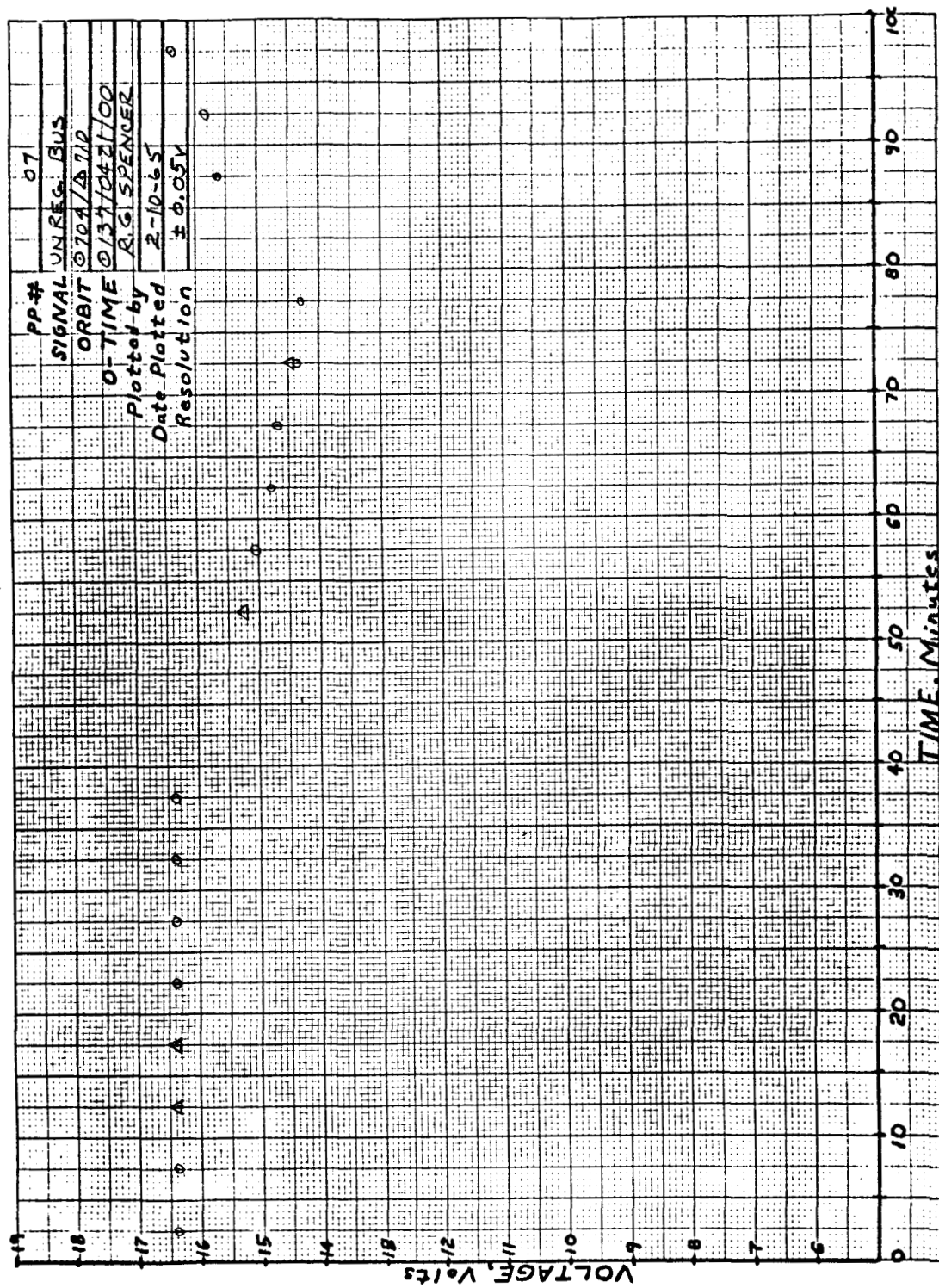


FIGURE 37

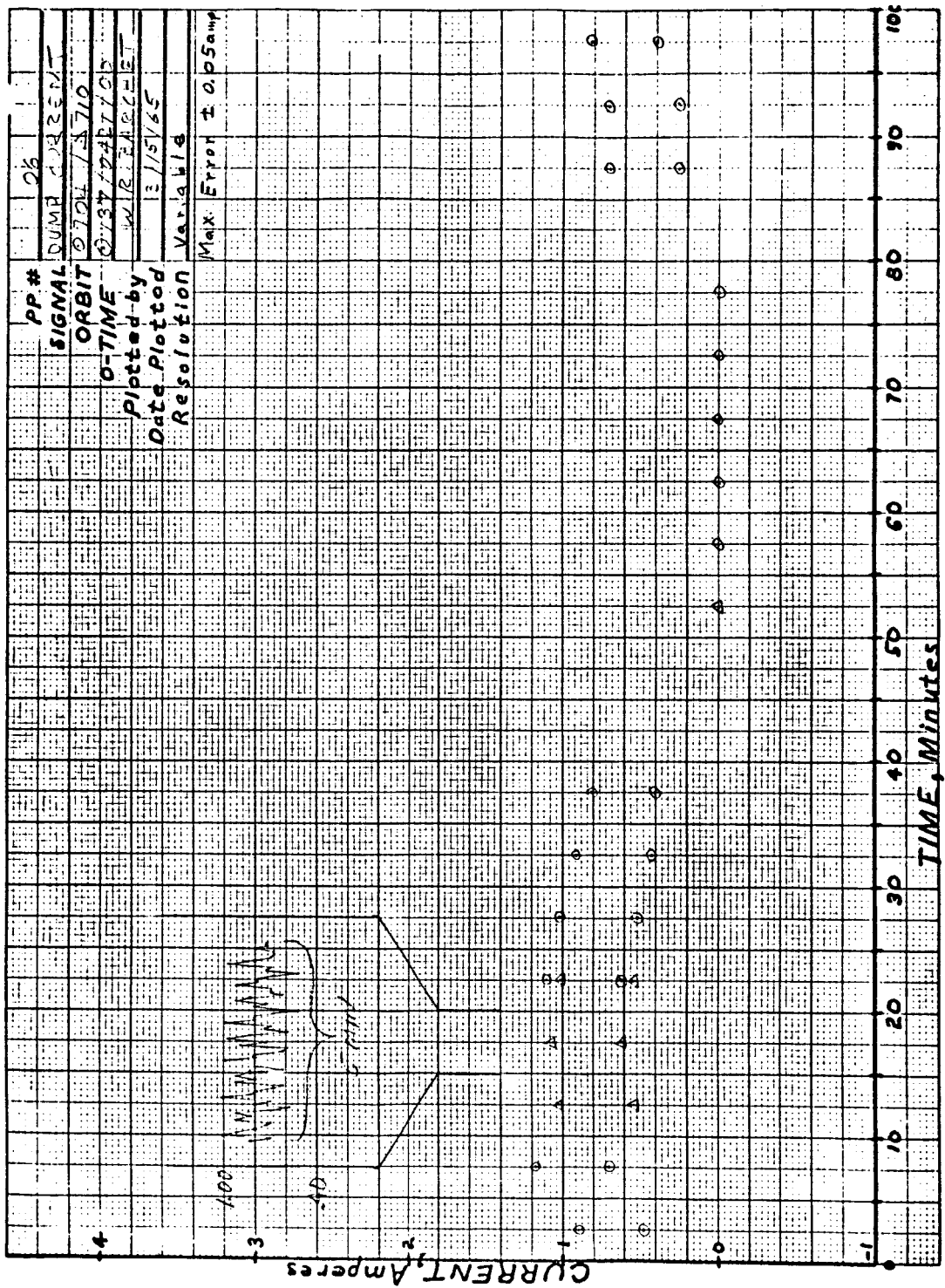


FIGURE 38

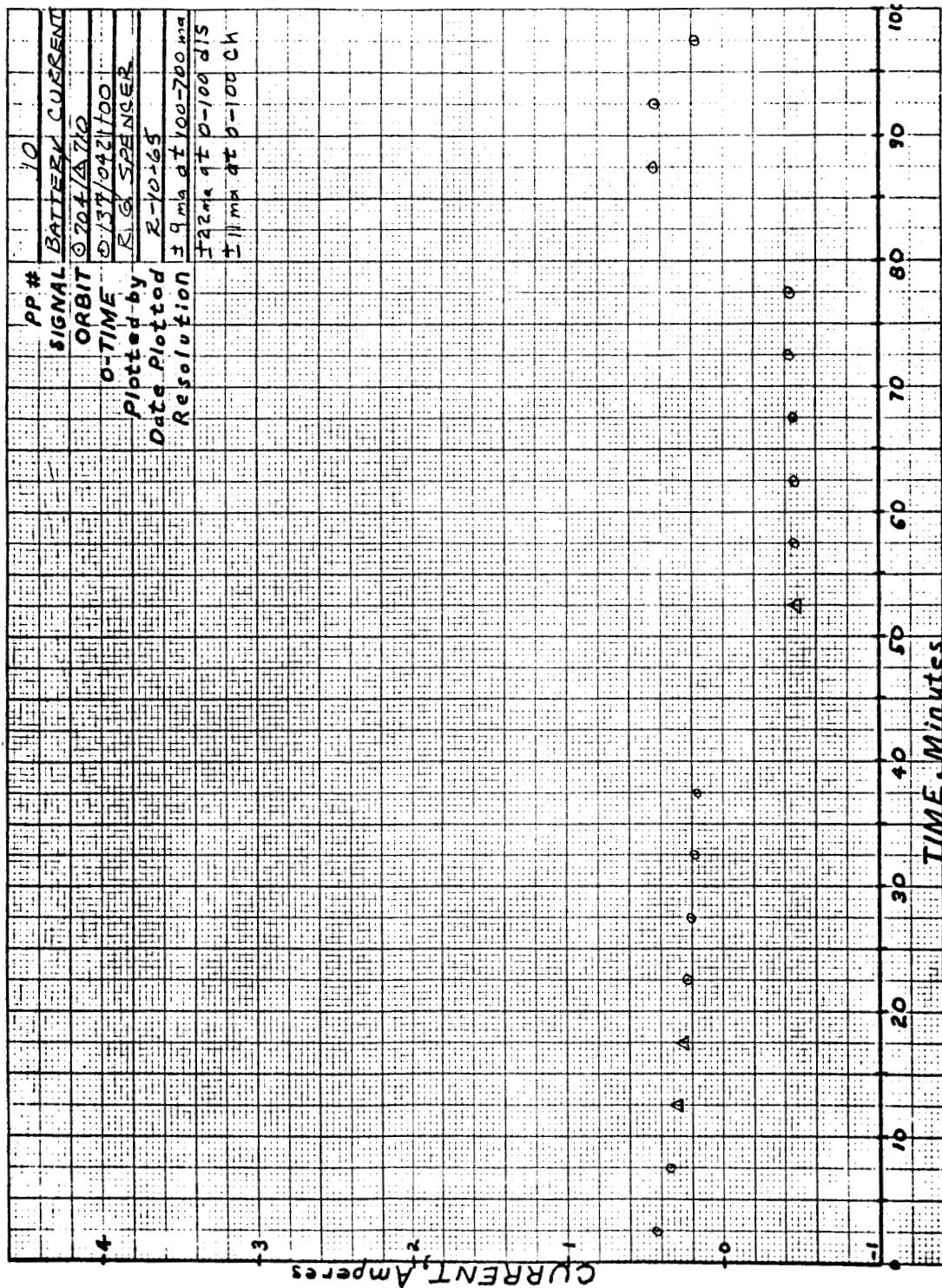


FIGURE 39

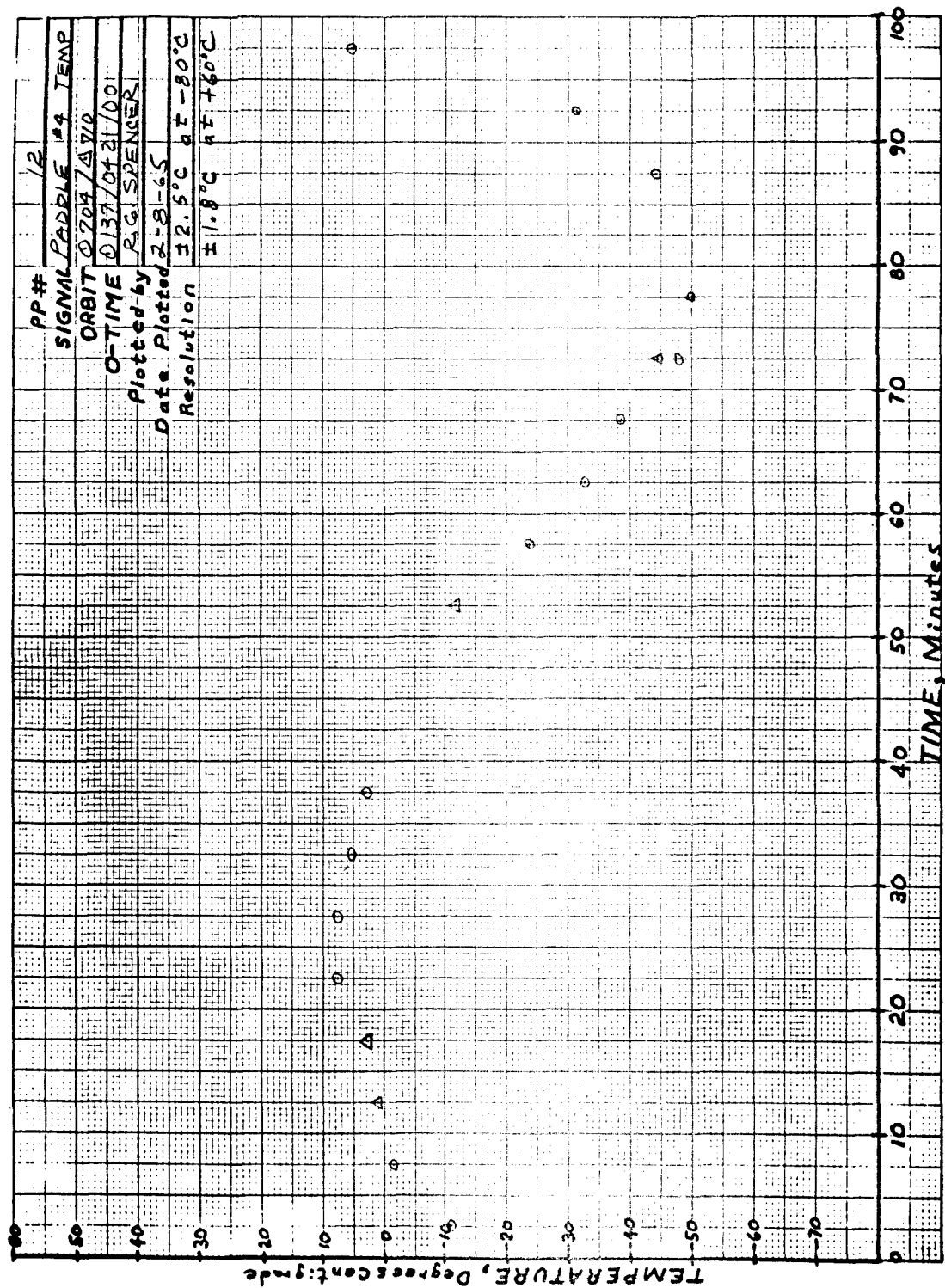


FIGURE 40

(3) Degradation of solar array performance with time.

The purpose of investigating the temporary fault in power system performance during orbit number 415 is to determine its most probable cause. As explained in section 3.1.2, it is reasonable to assume that the temperatures recorded during this period decreased as a result of the temporary drop in regulated voltages supplied by the power system. Furthermore, correlation of the solar current, battery current and dump current profiles indicates that an excessive load current was not required during this period. Thus, the general approach will be to correlate the telemetered data with known characteristics of the power system circuitry.

The anomaly in the available power output of the solar array should be investigated to determine whether or not a temporary fault occurred, and if so, the most probable cause. Since a favorable aspect ratio existed (See Figure 3), the dump current and solar voltage profiles should be correlated to determine whether or not load requirements were met.

Essentially four conditions affect the telemetered performance parameters of the solar array during orbital daylight. These are:

(1) Battery charge state (2) Array temperature (3) Aspect ratio, and (4) Damage (either cell cover discoloration, micrometeorite erosion, open or shorted panel). Changes in telemetered performance parameters can be uniquely identified with the first three conditions. Thus, any permanent change not attributable to the first three conditions must be caused by some type of damage.

#### 4.0 THERMAL PERFORMANCE

Reduced data from phase I, as presented in reference 1, has been organized to facilitate direct comparison with thermal performance predictions as developed prior to launch by GSFC. It should be noted that thermal analyses performed at GSFC on preliminary coating configurations led to the adoption of the flight coating pattern. Final analyses resulted in validation of the suitability of the configuration and in predictions of the performance. Actual results have been superimposed upon the predictions in the curves of this section for the purpose of showing the degree of precision achieved in prediction and also to show the thermal behavior of the spacecraft in the event that it has significance to the other areas of investigation, namely, dynamical performance and power supply performance.

##### 4.1 Predicted Thermal Performance

Predictions of Ariel II thermal performance were developed in terms of solar aspect angle, which is defined as the angle between the spacecraft spin axis and the sun line, and in terms of percent sunlight in the orbit. The choice had been made to plot predicted temperature versus aspect angle for maximum sunlight and minimum sunlight orbits and, thus, develop a band in which all operating points, or at least most operating points, would occur. Percentages of 100 and 65 were used to represent maximum and minimum percent sunlight respectively. To make comparisons of predicted performance and actual performance feasible, the thermal analysis was coordinated with the selection of locations for temperature sensors.



Final prelaunch predictions appear on figures 41 through 47 where they are compared to actual performance; however, review of actual performance results led to a reexamination of the prelaunch computation and a programming error was discovered in that computer input data for the 120° aspect angle was erroneous. Corrected prelaunch predictions based entirely on the original analysis, but with the effects of the noted error removed, are displayed in figures 48 through 52. Performance parameters 00 and 01 are not affected. Again comparisons are made.

#### 4.2 Actual Thermal Performance

To portray the spacecraft temperatures versus aspect angle, it was necessary to construct graphs for maximum and minimum sunlight orbits from the composite orbit graphs and from the variation of solar aspect angle graph using the days from launch parameter as the common denominator. It may be observed that the drawing of the curves through the points displaying actual results has been influenced by anticipated results. This is true because insufficient data points exist to establish a very tightly defined trace. It must also be borne in mind that aspect angle is subject to some uncertainty.

Limiting actual percent sunlight conditions encountered in orbit, 100% and 63%, matched predictions closely and permitted direct comparison.

#### 4.3 Conclusions and Recommendations

In general, the actual temperatures are slightly lower than predicted for aspect angles below 110° and higher than predicted for aspect angles above 110°; however, as a review of the curves presented in this section reveals, the predictions foretold quite well the range of temperatures experienced by the various spacecraft elements. This is true even when the



erroneous programming influenced results somewhat.

During the process of reviewing the composite orbit graphs of reference I, several singular situations were noted. Pages 174, 230, 300 and 314 are cited in particular. They all show a rapid temperature change of the ozone cell within a solar aspect range of  $135^{\circ}$  to  $150^{\circ}$ . Pages 174 and 300 show the most rapid temperature change of approximately  $6^{\circ}\text{C}$  per orbit. This occurs within the solar aspect range of  $136^{\circ}$  to  $142^{\circ}$ . Page 342 shows a  $50^{\circ}\text{C}$  temperature jump also for the ozone cell temperature sensor.

The ten-orbit stabilization graphs indicate that generally there was not more than 10 C degrees difference between the temperatures of the first and the 10th orbits. The most extreme of these variations was  $12^{\circ}\text{C}$  for the battery. The indication is that stabilization was attained early, perhaps after 5 to 7 orbits, although variations from other causes than stabilization mask the actual transient phenomena.

It is felt that some value might be derived from a careful investigation and refinement of the original prediction analysis to learn why the temperatures were lower than predicted at lower aspect angles and higher at higher angles. Nevertheless, it is also realized that to be meaningful such an investigation would be necessarily intensive, requiring more than the original analytical level of detail. Such work falls outside of the scope of the present contract and will not be undertaken for phase III. It would be done most expeditiously by the original thermal analysts at GSFC.

For purposes of the present study, thermal investigation is complete with the submission of this phase II report.

FIGURE 41

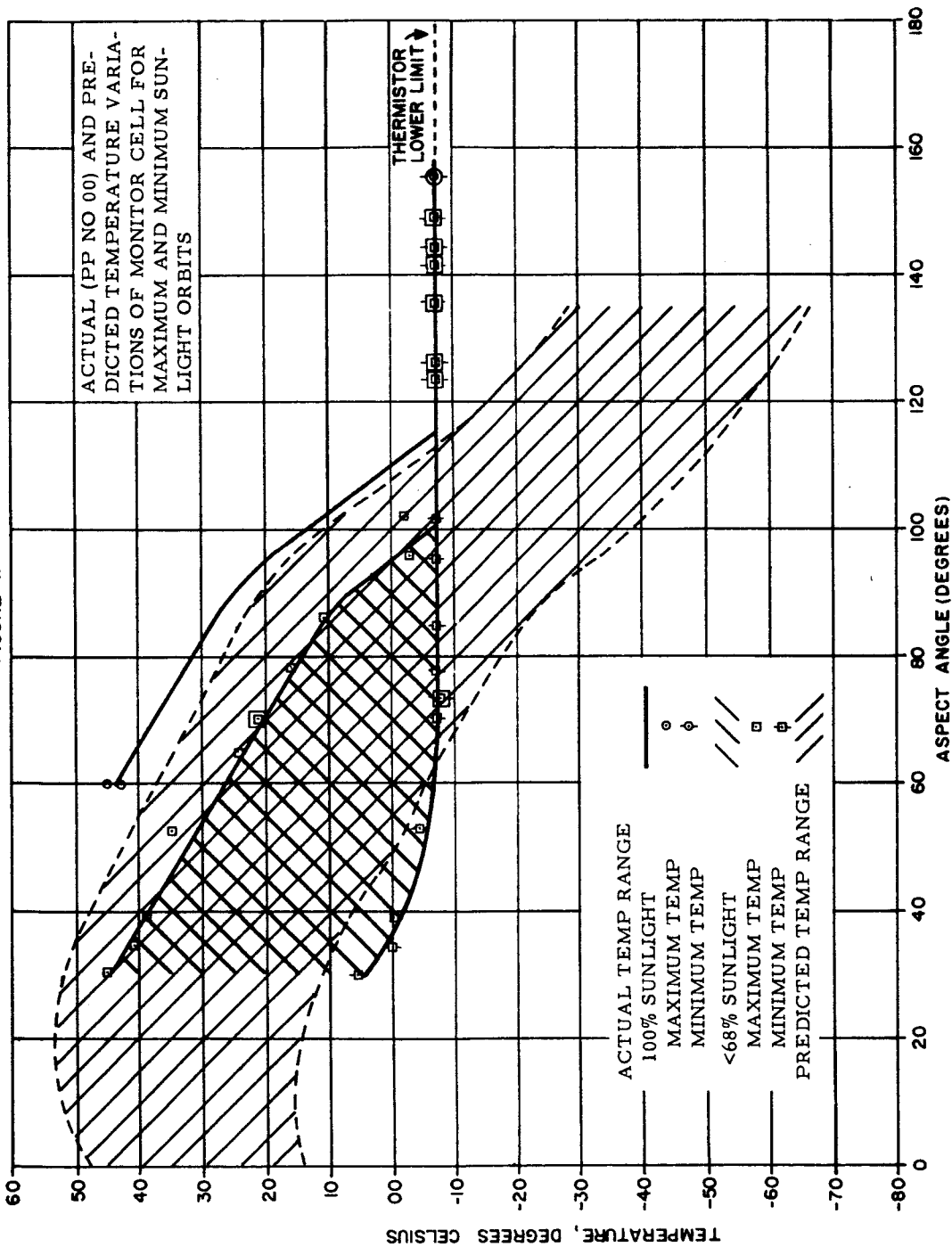


FIGURE 42

5463A-VB-1

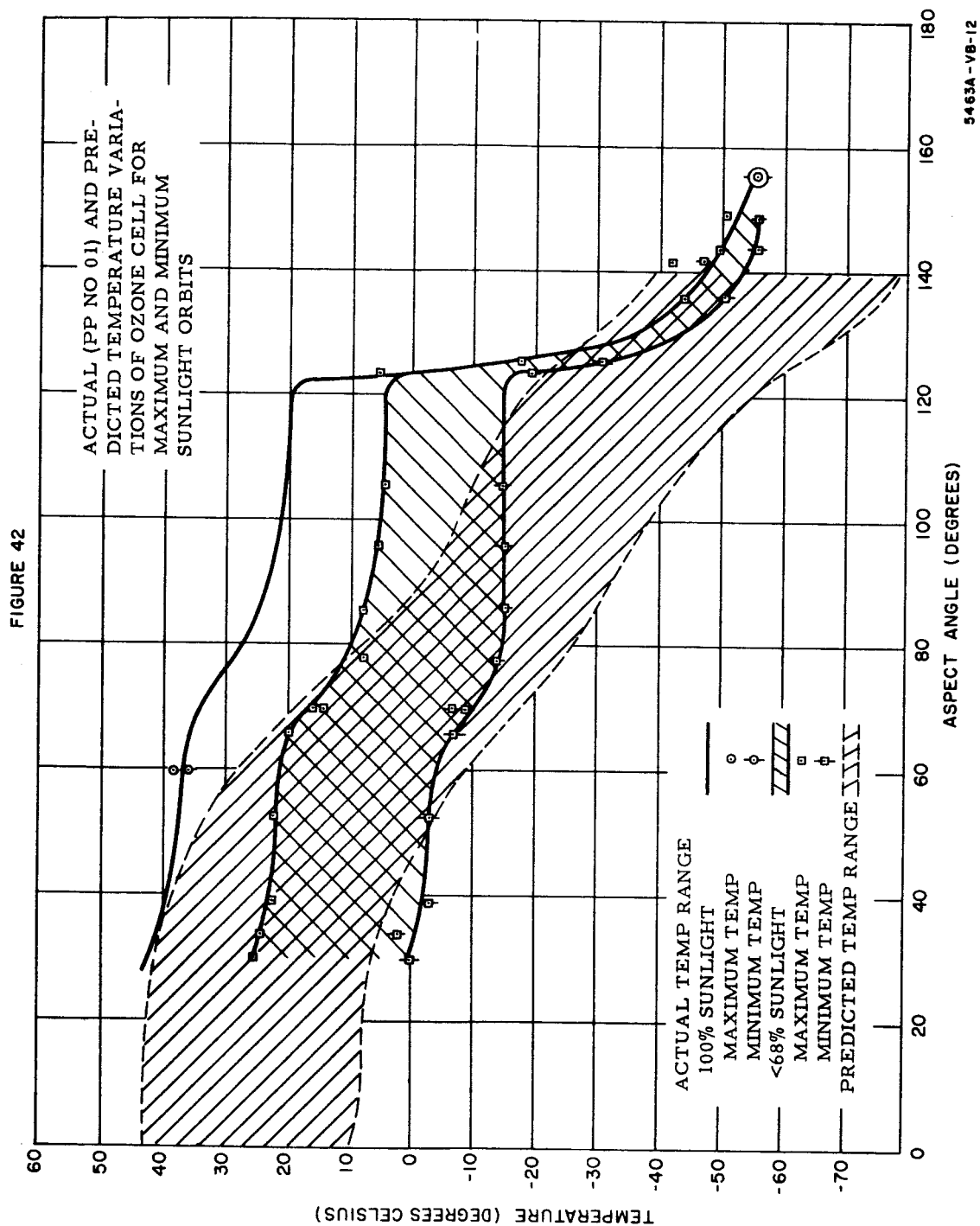


FIGURE 42

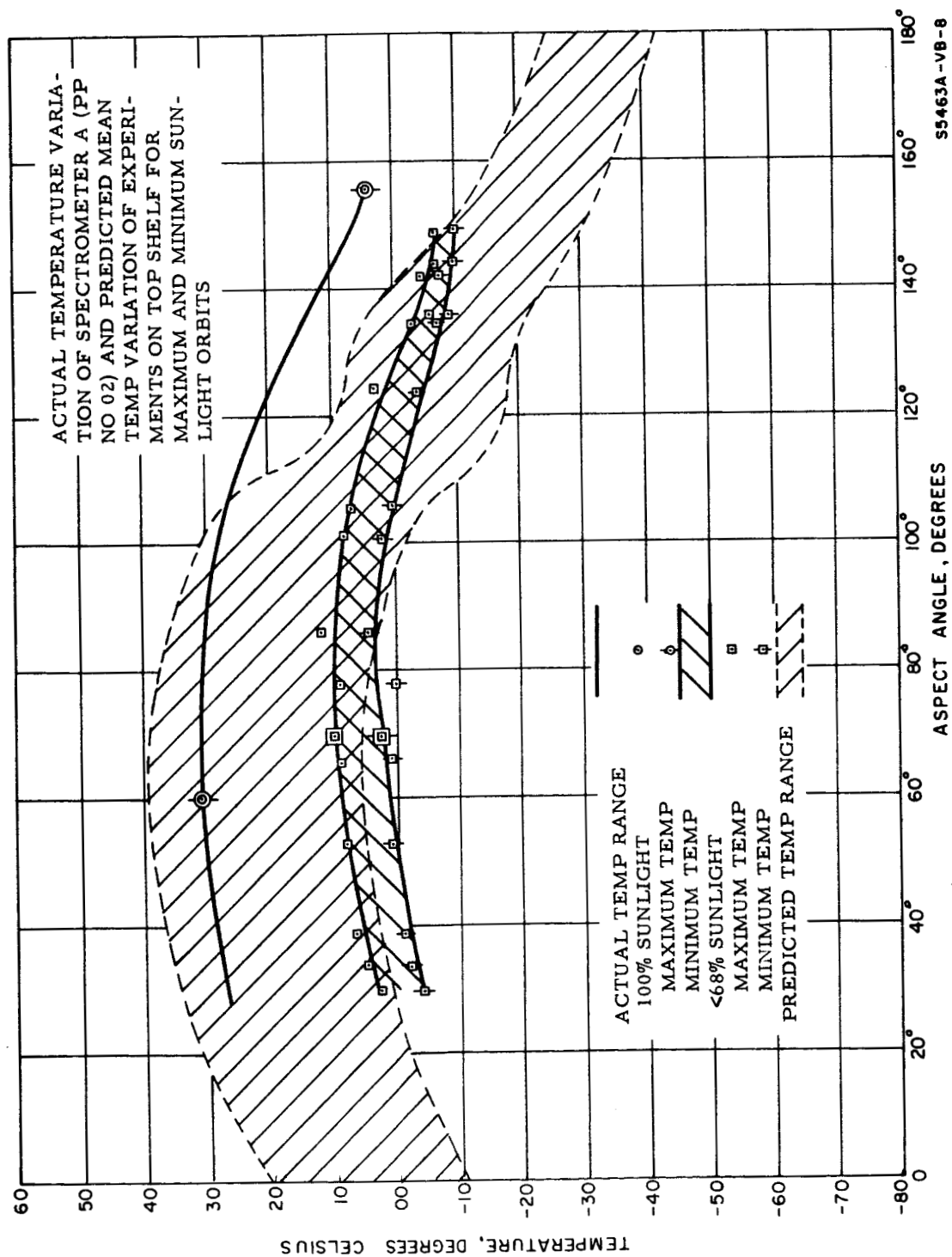


FIGURE 43

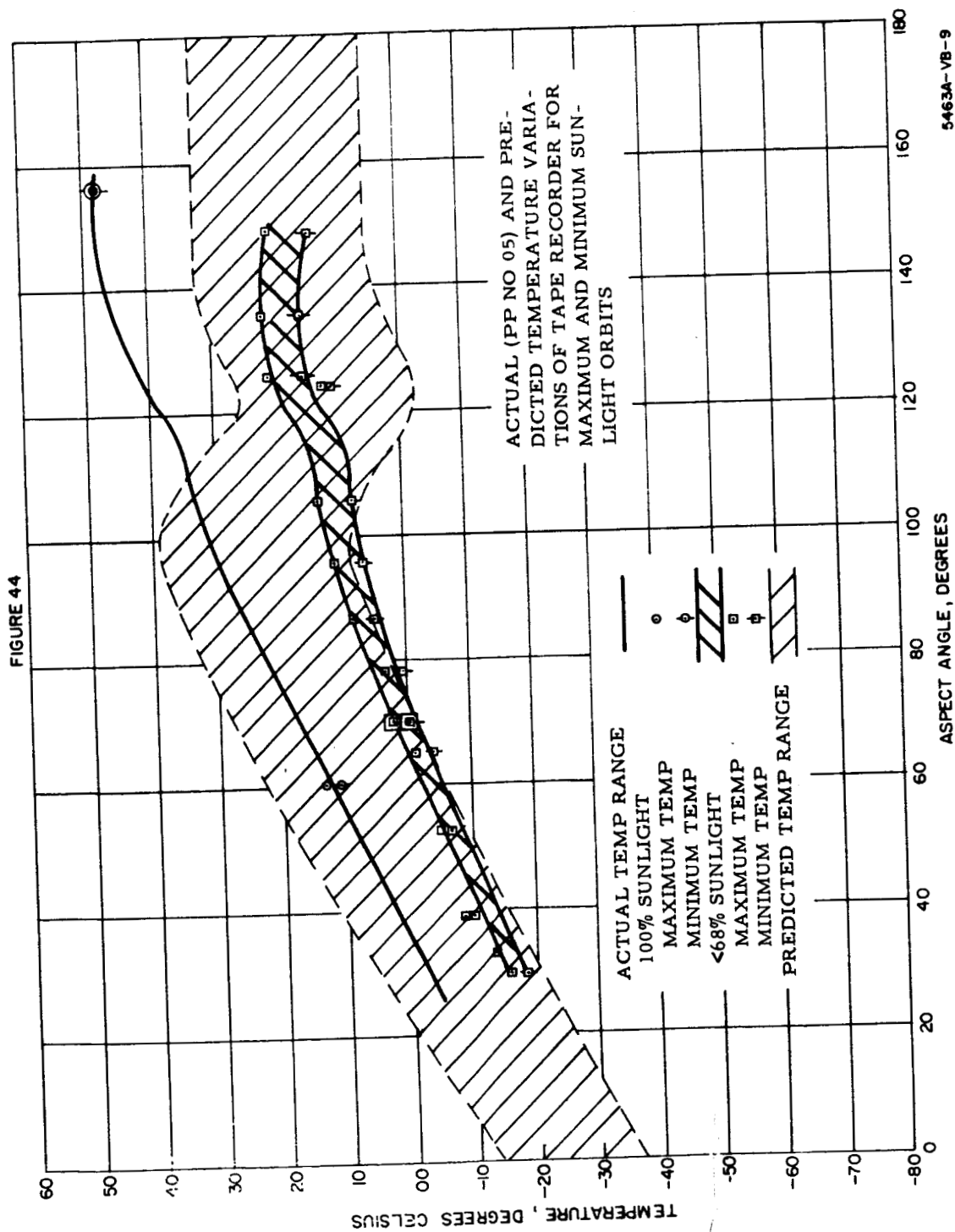


FIGURE 44

FIGURE 45

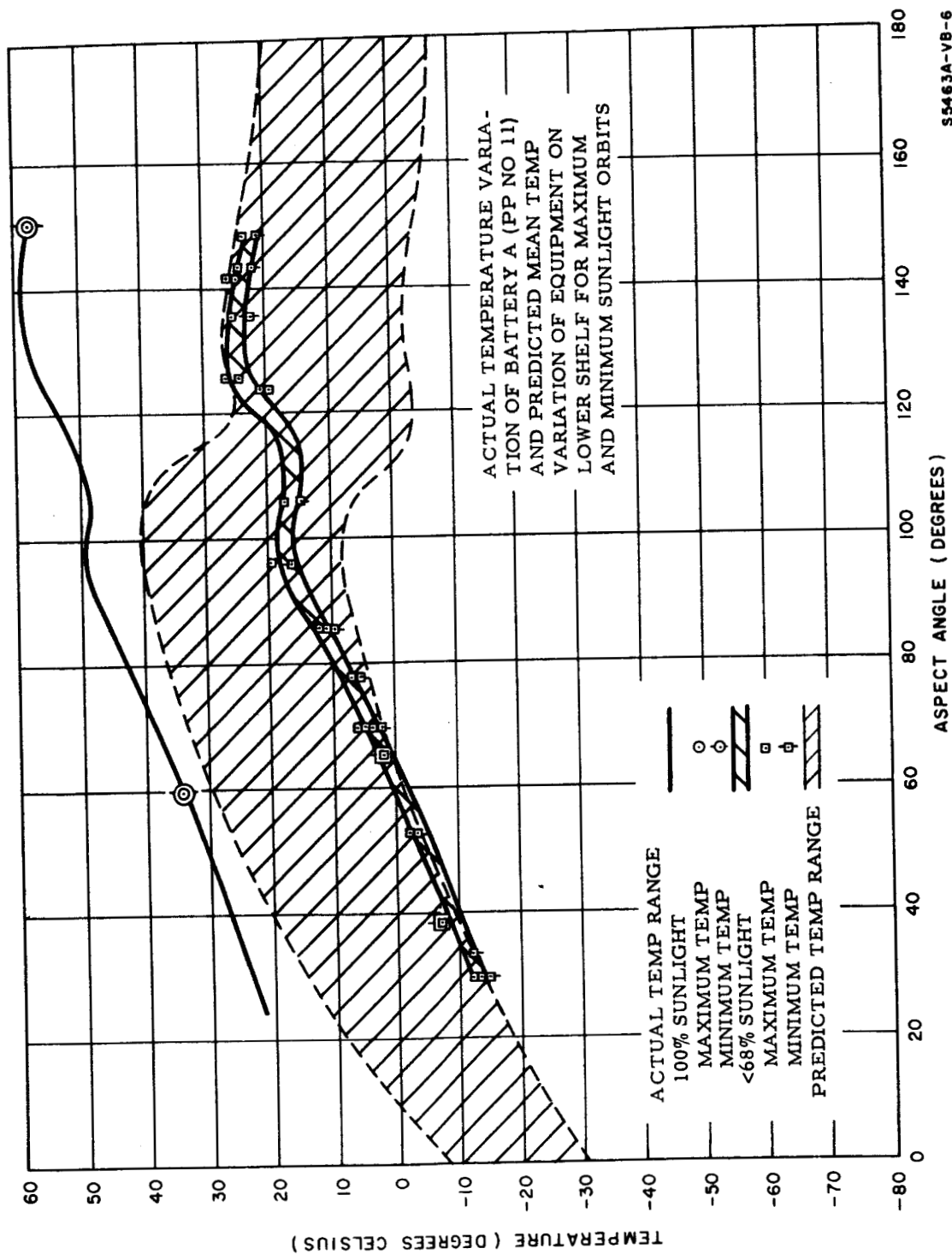


FIGURE 45

FIGURE 46

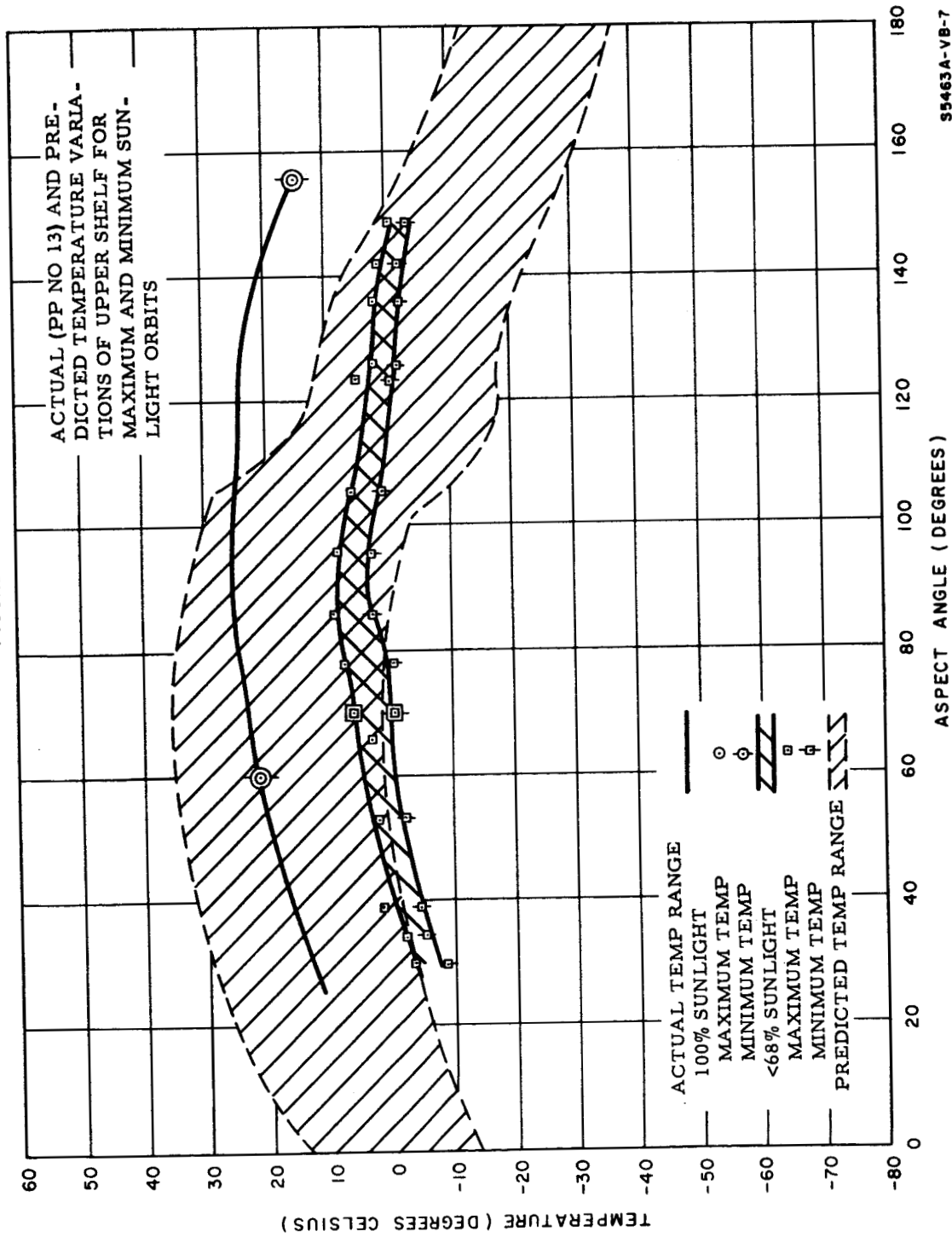


FIGURE 46

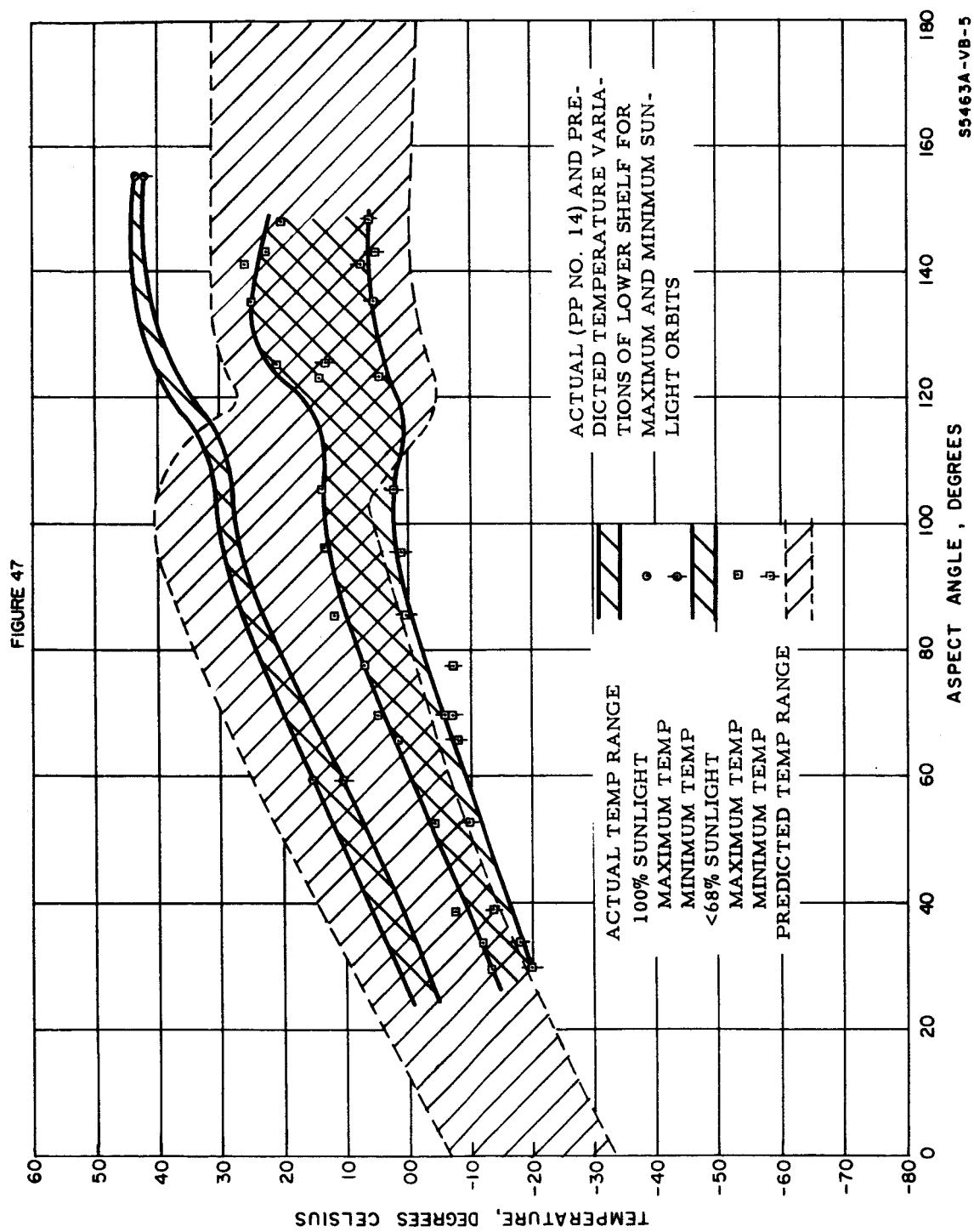


FIGURE 47



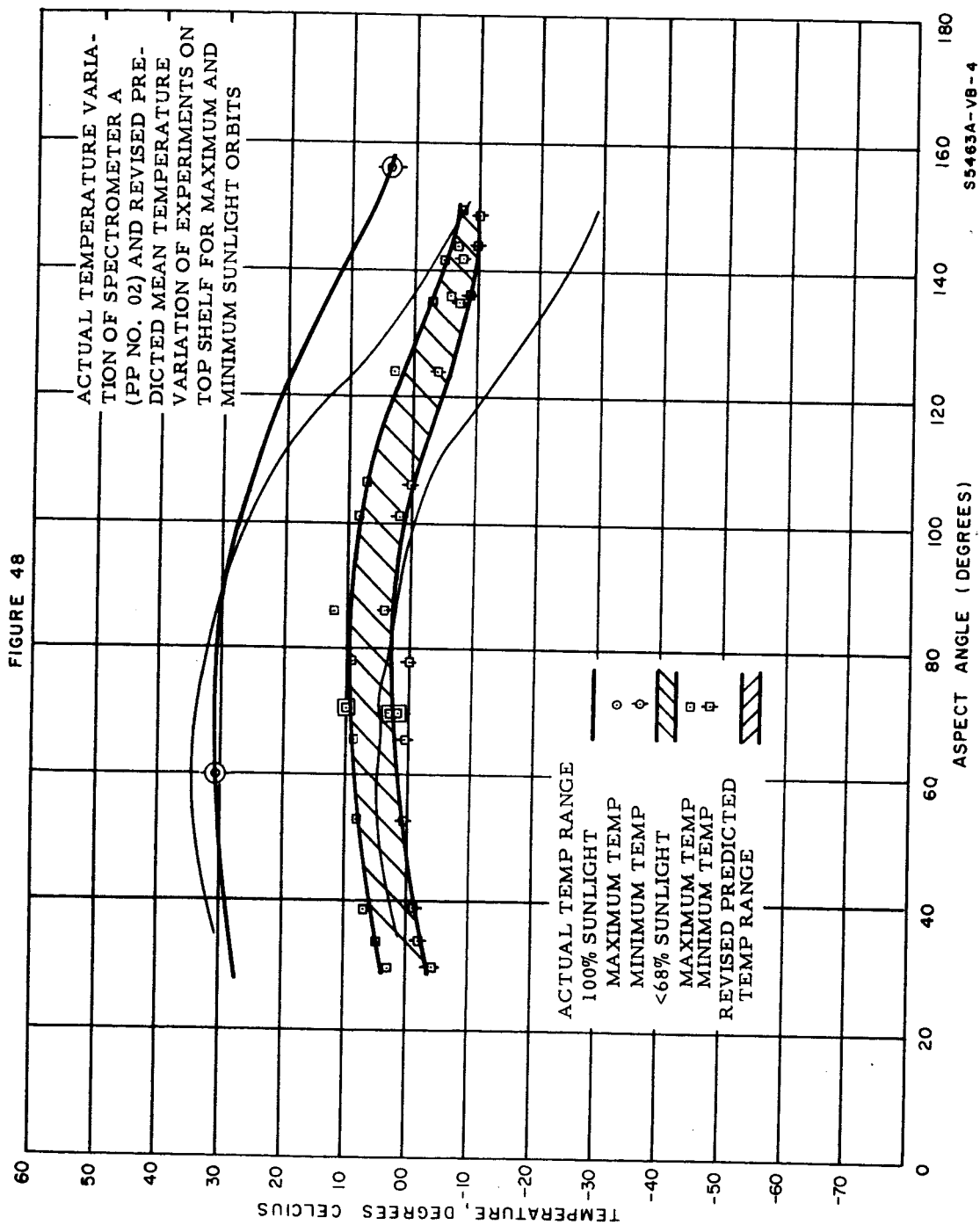


FIGURE 48

FIGURE 49

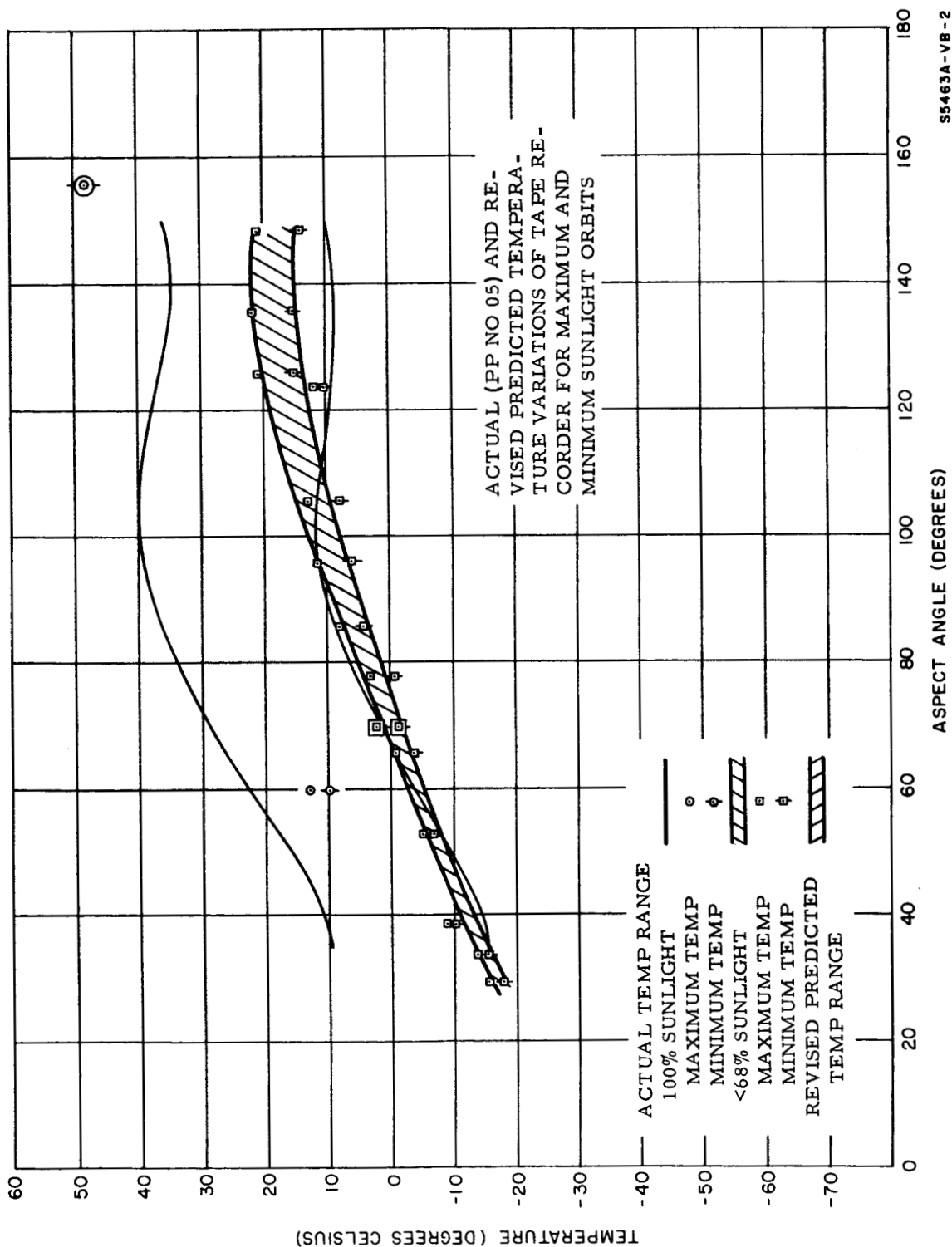


FIGURE 49

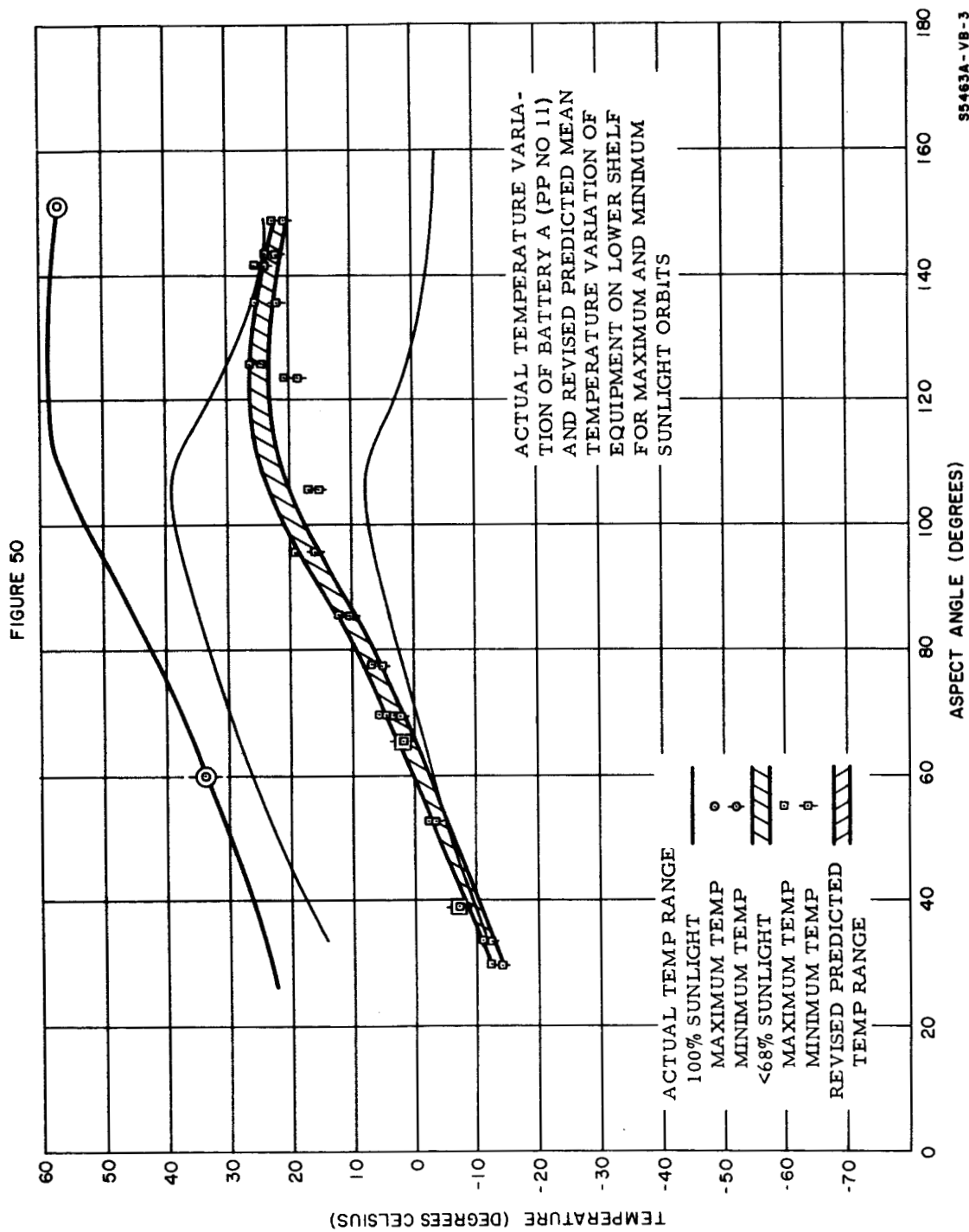


FIGURE 50

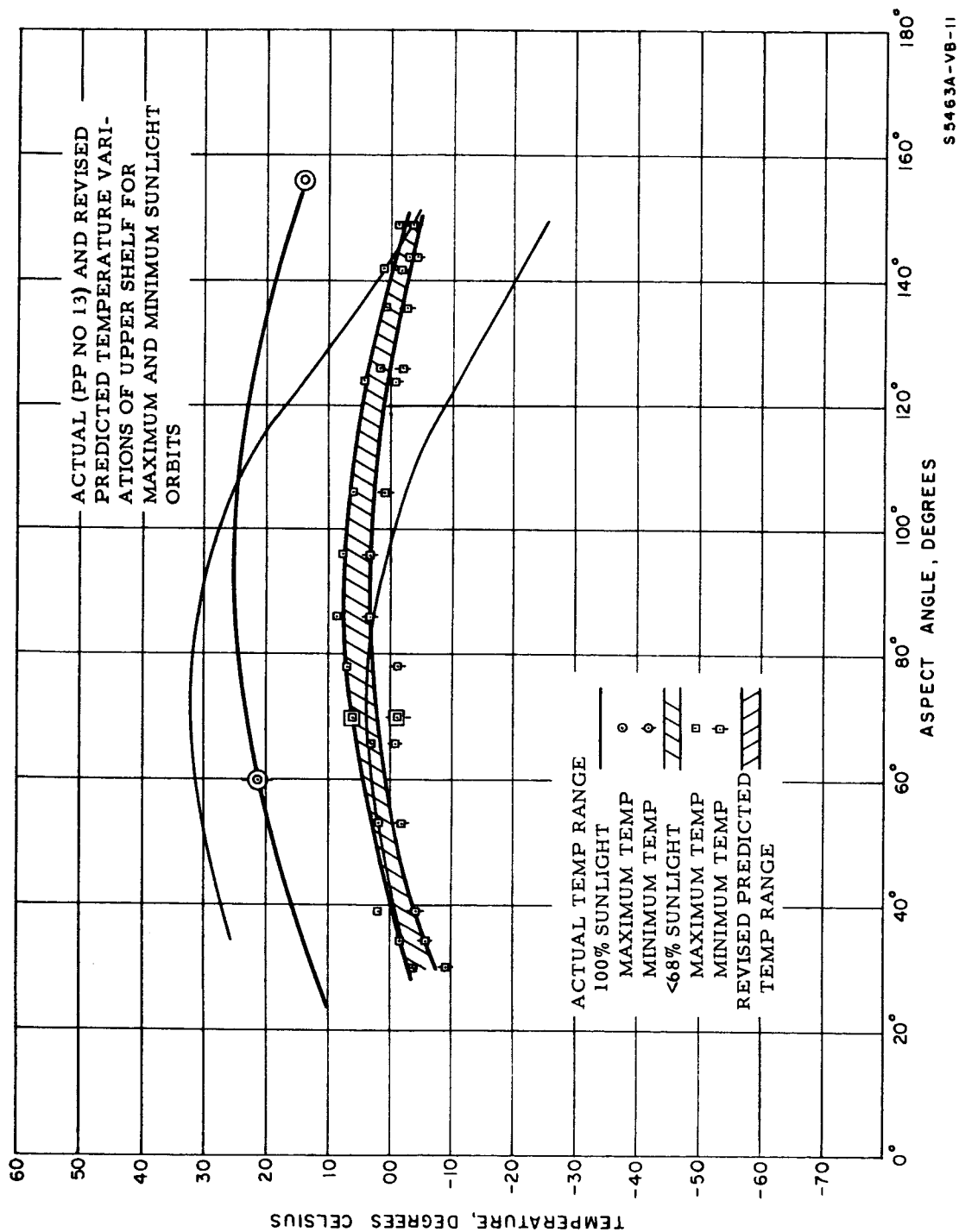


FIGURE 51

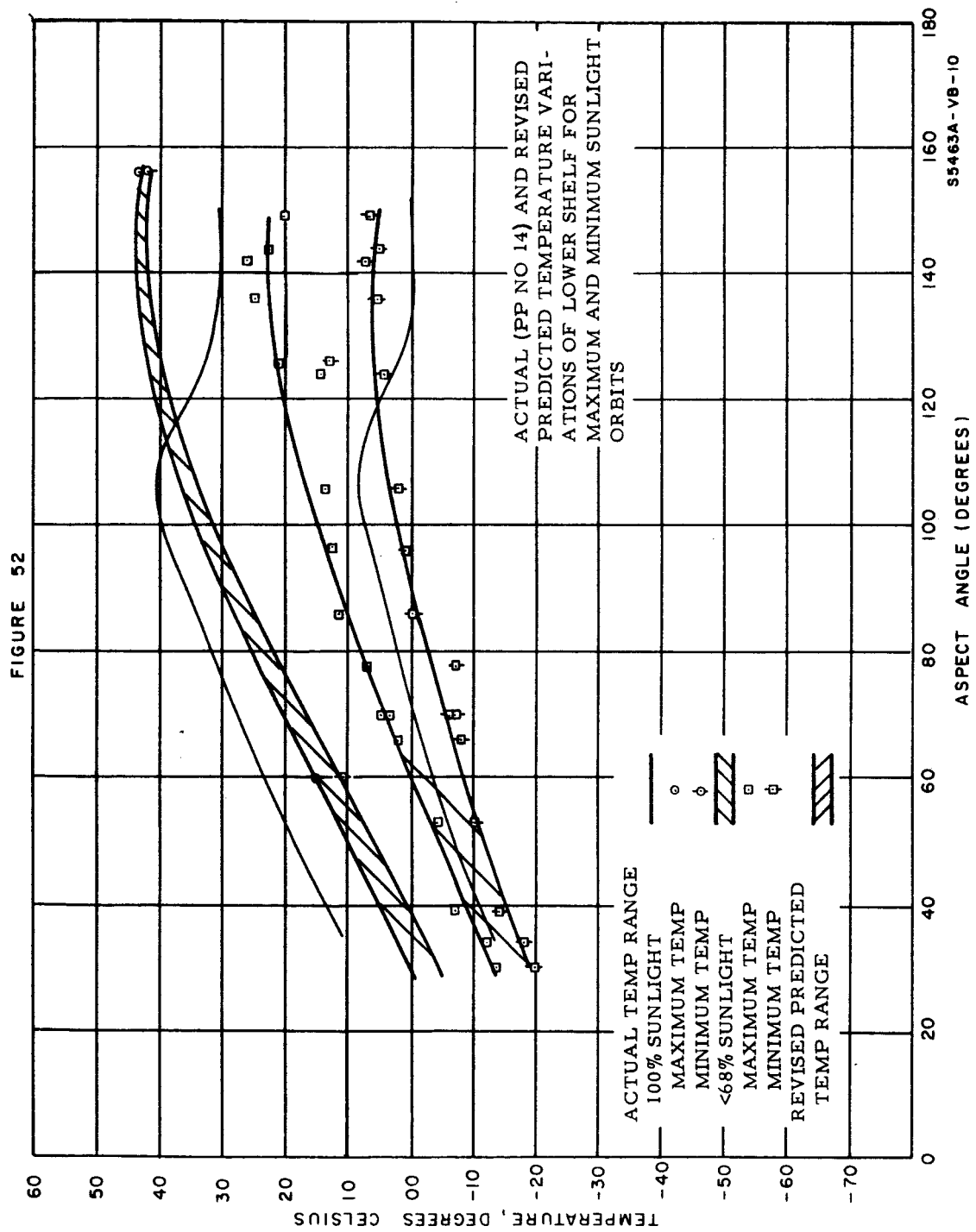


FIGURE 52

## 5.0 GENERAL CONCLUSIONS AND RECOMMENDATIONS

A review of conclusions for the three areas considered indicates that an adequate level of performance was maintained for the collection of data by the Ariel II spacecraft. This condition obtained for the initial period after injection into orbit. Because the experiments depend upon spin in their operation, however, loss of spin by the spacecraft resulted in cessation of useful data collection except for occasional information from the ferrite rod galactic noise antennas. Spin axis orientation experienced a wide excursion over the 200-day interval studied.

Power supply performance was adequate with the exception of possibly two anomalous periods. All telemetered performance parameters displayed anomalous behavior in orbit 415 and this may be related to a power supply problem. Also, it appears that available power may have dropped below requirements in orbit 704.

The spacecraft thermal design proved to be well executed. In general actual temperatures followed predicted values very well although actuals ran somewhat lower than predicted for aspect angles below  $110^\circ$  and somewhat higher for higher aspect angles. Thermal stabilization to quasi-equilibrium was attained in 5 to 7 orbits.

Recommended effort for Phase III consists of the following:

- (1) a definition of spin axis orientation trajectory
- (2) an evaluation of spin torques
- (3) an explanation of cited power system performance anomalies

No attempt to explain temperature departures from predicted values will be made because the level of refinement in thermal design required to do so would be inordinate and unjustified.